3D Printed Cortical Tissue and Implantation

Yongcheng Jin

Wolfson College

University of Oxford

A thesis submitted for the degree of

Doctor of Philosophy

Hilary 2023

Declaration

The work described in this thesis was performed between October 2019 and February 2023 in the Chemistry Research Laboratory, University of Oxford, United Kingdom, under the supervision of Professor Hagan Bayley. All the work described is my work, unless otherwise acknowledged. No work in this thesis has been submitted formerly for any other degree at the University of Oxford, or any other universities.

Yongcheng Jin

February 2023

For my family and friends

3D Printed Cortical Tissue and Implantation

Yongcheng Jin
Wolfson College, University of Oxford
A thesis submitted for the degree of Doctor of Philosophy
Hilary 2023

Abstract

It is a considerable challenge to engineer human tissue with multiple cell types and a defined cellular structure and function. The outer layer of the brain, the cerebral cortex, is composed of a layered architecture, which consists of multiple types of layer-specific neurons arranged into vertical columns. The layered structures enable higher cognition via intricately wired neuronal circuits; however, the present tissue engineering technique cannot generate these structures. In the current DPhil project, we used a droplet-based bioprinting technique to assemble living tissues mimicking simplified cerebral cortical columns. Upper- and deep-layer cortical neural progenitors were differentiated from human-induced pluripotent stem cells (hiPSCs) and were then droplet printed into two-layered cerebral cortical tissues. In the subsequent characterization, we found that the tissues demonstrated layer-specific biomarker expression and produced an integrated axon network. The printed cerebral cortical tissues were implanted into mouse brain explants, which revealed a considerable host–implant connection across the boundaries via axon projection, neuron migration, and the establishment of correlated calcium ion signals. Implanted brain explants can be applied in the evaluation of compounds and nutrients that facilitate tissue integration. Moreover, our technique might be used in personalized implantation therapy by 3D-printed tissues generated from patients' own iPSCs.

Acknowledgments

I would like to thank the following people for their contributions to this work. My family, who are responsible for improving my quality of life, and my close friends for their encouragement throughout my DPhil.

Professor Hagan Bayley, for his creative scientific vision, and for enabling my development as a scientist. This work was made possible by his long-term vision and consistent rigor in all things, from experimental designs to the use of words in writing.

The Bayley Group, for their support. In particular, Dr. Linna Zhou provided patient training and day-to-day guidance in many aspects; Ellina Mikhailova helped with the cell culture and enabled the project to progress rapidly; and Xingyun Yang and Dr. Yujia Zhang provided various 3D culture, engineering, coding, and statistics support. Collaborators from the Department of Physiology, Anatomy & Genetics and the Department of Pharmacology, Oxford, for their help and guidance. Prof. Ming Lei and Dr. Tianyi Sun helped with the animal work, while Dr. Sally Cowley provided the human cells. Kaili Liu, Daniel Catarino, Luana Campos Soares, and Sara Bandiera helped with various experiments across the project. Prof. Francis G. Szele and Prof. Zoltan Molnar provided design, assistance, and guidance throughout the project.

I also acknowledge that English spelling and grammar in this Thesis were proofread by Scribendi, a professional editing and proofreading service provider.

The work is funded by the Oxford Martin School.

Abbreviations

Abbreviations	Definition
2D	two-dimensional
3D	three-dimensional
BDNF	brain-derived neurotrophic factor
BRN1	POU homeodomain protein 1
BRN2	POU homeodomain protein 2
CNS	central nervous system
CTIP2	COUP-TF-interacting protein 2
CUX1	drosophila homeobox cut gene 1
CUX2	drosophila homeobox cut gene 2
DAPI	4′,6-diamidino-2-phenylindole
DAPT	N-[N-(3,5-Difluorophenacetyl)-L-alanyl]-S-phenylglycine t-butyl ester
DIB	droplet-interface bilayer
DN	deep-layer neuron
DNP	deep-layer neural progenitor
DPBS	Dulbecco's phosphate-buffered saline
DPBST	DPBS with 0.1% Triton X-100
DPhPC	1,2-diphytanoyl-sn-glycero-3-phosphocholine
DPI	day post implantation
EBSS	Earle's Balanced Salt Solution
ECM	extracellular matrix
EDTA	ethylenediaminetetraacetic acid
EGF	epidermal growth factor
EHS	Engelbreth-Holm-Swarm
FBS	fetal bovine serum
FGF-2	fibroblast growth factor 2
GABA	gamma-aminobutyric acid
GF	growth factor
GFP	green fluorescent protein
hiPSC	human induced pluripotent stem cell
HNCAM	human neural cell adhesion molecule

iPSC	induced pluripotent stem cell
KO	knockout
MAP2	microtubule-associated protein 2
NCAM	neural cell adhesion molecule
NESTIN	neuroepithelial stem cell protein
NIM	neural induction medium
NMM	neural maintenance medium
NP	neural progenitor
NTM	neural terminal medium
PFA	paraformaldehyde
PI	propidium iodide
PNS	peripheral nervous system
qPCR	quantitative polymerase chain reaction
RFP	red florescence protein
RGC	radial glial cells
ROI	region of interest
RT	room temperature
RT-qPCR	real-time quantitative polymerase chain reaction
SATB2	special AT-rich sequence-binding protein 2
TBI	traumatic brain injury
TBR1	T-box brain transcription factor 1
TUJ1	class III β-tubulin
UN	upper-layer neuron
UNP	upper-layer neural progenitor
WPP	week post-printing

Table of Contents

Table of Figures

Table of Tables

Chapter 1. Introduction

Three-dimensional (3D) printing, known as additive manufacturing, is a computer-aided manufacturing process that assembles 3D structures additively based on pre-designed digital models. This process has enabled the rapid prototyping of complex 3D geometries from various materials, such as metals, ceramics, and plastics[1]. Now, bioprinting is an emerging field that enables the additive manufacture of biological materials. Recent bioprinting advances have demonstrated the precise patterning of cells and biomaterials to attain 3D functional living tissues. Examples of printed tissues include inkjet-printed skin[2], layered cartilage[3] and bone constructs[4], an extrusion printed aortic valve[5], and an acellularized skin construct produced by laser-assisted printing[6]. In 2020, the Bayley Group reported on a droplet-in-oil printing technique to fabricate cell-laden droplets, forming tissue-like constructs[7]. In the current study, we advance the droplet-based printing technique and form two-layered cerebral cortical tissue, resembling a simplified model of the human cerebral cortex. Our approach gains tremendous interest in the future application of personalized implantation treatments for brain disease using 3D tissues derived from a patient's own induced pluripotent stem cells (iPSCs).

As one of the most important brain structures, the cerebral cortex has a layered cellular architecture constituting layer-specific neurons organized into vertical columns, delivering higher cognition via intricately wired neural circuits[8,9]. Existing tissue engineering methods cannot generate such structures. However, by using our droplet-based printing technique, we produced tissues comprising simplified cerebral cortical columns. Human iPSCs (hiPSCs) were

differentiated into upper- and deep-layer neural progenitors and then bioprinted to produce cerebral cortical tissues with a two-lamina organization. We implanted cortical tissues into mouse organotypic brain slice cultures and revealed substantial implant–host integration.

The following introductory chapter summarizes the biological background of the central nervous system (CNS) and traumatic brain damage, followed by techniques for producing living neural tissues. We also describe implantation-based therapies, from dissociated cells and organoids to the implantation of our printed cortical tissues.

1.1. Biology of the Neural System

1.1.1. From the Neural System to the Cerebral Cortex

In mammals, including humans, the nervous system consists of two main parts: the CNS and the peripheral nervous system (PNS). The CNS is composed of the brain and spinal cord, while the PNS contains mainly nerves, which are enclosed bundles of the long fibers or axons that deliver and receive information for the CNS to every other part of the body. The PNS can be further separated into three subsystems: somatic, autonomic, and enteric nervous systems[10]. Somatic nerves regulate voluntary movement[11,12], and the autonomic nervous system contains the sympathetic and parasympathetic nervous systems[13]. The sympathetic nervous system, in response to stressful situations, mediates the "fight-or-flight" response[14], while the parasympathetic nervous system regulates relaxation and mediates the "rest and digest" or "feed and breed" reaction[15]. The enteric nervous system regulates the gastrointestinal system[16].

The CNS consists primarily of the spinal cord and brain[17]. The spinal cord contains nerves that carry messages between the brain and the rest of the body [18]. The brain is composed of the

cerebrum, cerebellum, and brainstem[19]. As the largest part of the brain, the cerebrum can be further distinguished into the cerebral cortex (often referred to as gray matter)[20], and subcortical structures (often referred to as white matter) containing a set of small deep nuclei, such as the basal ganglia, hippocampus, and thalamus[21,22].

In humans and most other mammals, the cerebral cortex, the outer layer of neural tissue of the cerebrum, is the most important part of the brain and is responsible for higher cognitions. It plays a key role in attention, perception, awareness, thought, memory, language, and consciousness[23,24]. Each cortical region has specific functions, such as movement in the motor cortex, and sight in the visual cortex[25]. In the human cerebral cortex, 14 to 16 billion neurons are organized into horizontal cortical layers[26,27], and radially into cortical columns[28]. The cerebral cortex typically has a six-layer architecture composed of layer-specific neurons. Layers I–IV are designated as the upper layer[29], while Layers V–VI are the deep layers[30]. Intracortical wiring of neural circuits between different layers[8,9] is believed to play an important role in higher cognition in mammals[31,32]. Cerebral cortical neurons consist of different variations with two major morphological shapes: pyramidal and stellate cells[33]. Pyramidal cells, mostly glutamatergic excitatory neurons, comprise approximately 80% of the cellular component of the cortex, generating output to other regions of the cortex or the rest of the CNS[34]. Stellate cells are usually small and distributed through the cortex, with the function of modulating the activity of other cortical neurons[35]. Stellate cells are composed of excitatory interneuron releasing glutamate and inhibitory interneurons releasing gamma-aminobutyric acid (GABA) as neurotransmitters[36,37]. Each cortical layer is differentiated by the size, shape, and subtype of the neurons. Practically, biomarkers expressed differently in the neurons of each cortical layer provide a useful tool for distinguishing and studying the neuroanatomical structure[38,39].

1.1.2. Global Challenges of Traumatic Brain Injury

Brain damage from disease and injury has devastating social and economic consequences. Brain injuries, such as traumatic brain injury (TBI), lead to damage to the cerebral cortex and create a catastrophic burden on patients and the public. According to a 2018 report, 69 million people worldwide suffered from TBI, of which 4.8 million were severe[40,41], leading to disabilities and 30% mortality[42,43]. Nevertheless, effective medication is still not developed for the treatment of severe brain injuries[44]. Attempts have been made to implant dissociated neural progenitor cells and brain organoids into mouse brains for the study of brain repair[45,46]. However, the structure of the injured brain tissues was not completely repaired in these reports, as the implanted cells or organoids cannot generate a cellular architecture that mimics the brain's natural anatomy.

1.2. Artificial Generation of 3D Neural Tissues

1.2.1. Generation of Neural Cells

The generation of neural cells *in vitro* serves as an essential first step in fabricating 3D neural tissues. Early studies of human cerebral cortex relied on extrapolating the understanding of rodent cortical development and functions. In 2006, Shinya Yamanaka reported that mouse iPSCs, a type of pluripotent stem cell, can be generated directly from somatic cells[47]. This iPSCs technique was later extended to human cells in 2007, enabling an unlimited human-originated cell source[47,48]. Scientists around the world quickly adapted protocols and methods originally developed for embryonic stem cells to differentiate hiPSCs into specific somatic cells for research and medical purposes[49-51]. In 2012, Shi et al. reported a robust and multistep process protocol mimicking human cortical development to direct differentiation of hiPSCs to cortical stem and progenitor cells, followed by an extended period of cortical neurogenesis. The terminally differentiated

neuron from the protocol demonstrated mature electrophysiological properties, as well as a functional synaptic network[52,53].

In humans and most mammals, cortical neurons are formed in temporal order. Deep-layer neurons (DNs), as the early product of cortical neurogenesis, divide asymmetrically from radial glial cells (RGCs) and migrate toward the cortical plate by radial migration from the ventricular zone[54]. Later, in cortical neurogenesis, RGCs generate neurons that migrate radially into the cortical plate, passing through the DNs to become upper-layer neurons (UNs). Shi's protocol undergoes the same temporal process of neurogenesis and generated neurons of all layers, evidenced by the sequential generation of layer-specific biomarkers expressing neurons over 100 days incubation[52,53].

However, Shi's differentiation protocol results in the asynchronous production of layer-specific neurons in a single culture. It is practically challenging to select a specific neuronal population from a mixture of neurons representing different cortical layers. To address this issue, in 2013, Boissart et al. reported an iPSC differentiation protocol generating a stable and self-renewing neural progenitor population that synchronously differentiates into glutamatergic cortical neurons of the upper cortical layer. This is achieved by the prolonged pro-proliferative culture of neural progenitors, resembling the *in vivo* neurogenesis of the late production of UNs from proliferating RGCs[55].

The adaptation of a modified Shi's protocol in this project enabled us to generate DNs at the early differentiation stage. Modified Bossart's protocol allowed us to produce homologous UN cultures through prolonged proliferation. In the current study, we made bioinks with these hiPSCs

differentiated deep-layer neural progenitors (DNPs) and upper-layer neural progenitors (UNPs) and performed droplet-in-oil bioprinting to fabricate layered cerebral cortical tissues.

Conventional 2D cell cultures cannot fully represent normal tissues. Although monolayer cell culture has been widely used in cellular biology research, it does not mimic complex 3D physiological architectures[56,57]. Therefore, the 3D artificial generation of tissue was established to compromise this issue. Two main strategies, autonomous self-assembly of cells and biomimicry of tissues, were developed. Autonomous cellular self-assembly relies on the natural development process of cells, and produces, for example, organoids and assembloids[58,59]. The biomimicry approach involves patterning cells in tissue-like microarchitecture, with or without a scaffold, such as the microfluidic and 3D bioprinting method[2].

1.2.2. Organoid

During the late twentieth and early twenty-first centuries, cell lines and animal models have shown success in many fields, such as extending our understanding of cellular signaling, identifying potential pharmacological targets, and helping in the design of potential drugs[58,60,61]. However, extrapolating the results from cell lines or animal models to humans is considered a major bottleneck in biomedical research[62]. The advent of human organoids, stem cell-derived miniature 3D tissue, enabled us to recreate the architecture and physiology of human organs *in vitro* in detail. Human organoids have been widely applied to study infectious diseases[63], genetic disorders[64] and cancers[65]. Generally, organoids are produced from pluripotent stem cells or adult stem cells by mimicking the human developmental process or the organ regeneration process *in vitro*[58].

Organoid formation relies on two important processes. Initially, key signaling pathways associated with developmental patterning were activated or inhibited in 2D-cultured or 3D-

aggregated stem cells by small molecules or morphogens, leading to the establishment of a correct regional identity for later differentiation. Second, these inducted cells were aggregated into 3D structures or embedded into the 3D extracellular matrix (ECM). These early 3D structures were then cultured and grown in a way that allowed for their expansion and maturation into organoids in three dimensions[58]. Brain organoids were reported in 2013 by Lancaster and his colleagues [66]. Human pluripotent stem cells are initially guided to differentiate into embryoid bodies before further differentiation toward the neuroectodermal lineage. Once the cell aggregates contain developmental precursors for brain tissue patterning, the rest of the developmental steps occur spontaneously in a spinning bioreactor. The brain organoids were shown to develop into various discrete brain regions, and generate complex progenitor populations, organizing and producing mature neuron subtypes[66]. Thus far, organoids have been developed as remarkable tools in biomedical research. However, it has also been widely reported that the internal structures of organoids become spontaneously organized over time in an unpredictable and spatially disordered manner[66-68].

1.2.3. Assembloids

The human body relies on the physiological connections around organs. However, each type of organoid conventionally resembles only one simplified organ[58]. To study the interconnection of multiple organs *in vitro*, assembloids were developed and reported in 2020 by Pașca et al.[59,69,70]. Organoids were initially produced using established methods and then assembled with heterogeneous organoids or spheroids. In recent advancements, organoids resembling the cerebral cortex and the hindbrain/spinal cord were produced and assembled with human skeletal muscle spheroids through closely contacted co-culture to produce 3D corticomotor assembloids. It has been reported that cortical neurons project and connect with the spinal spheroid, while spinal-derived motor neurons connect with muscle. The stimulation of cortical spheroids triggers the

contraction of 3D muscle. The capacity to form functional circuits in assembloids makes it a remarkable tool for studying development and disease in the future[59,70].

1.2.4. Bioprinting

The bioprinting strategy has been applied to fabricate 3D tissues, as it can accurately place cells at high resolution, forming size- and structure-defined constructs. This strategy also offers users great control over the shape, cellular components, and texture of fabricated tissues through computer-assisted design. Unlike the unpredictable self-developed pattern in organoids, the printing procedure can be engineered and scaled up, allowing the high throughput generation of patterned tissues with great reproducibility[2,71].

Current bioprinting strategies can be cataloged by the technologies employed to distribute cells, including extrusion-based, laser-based, stereolithography-based, and droplet-based 3D bioprinting. Extrusion-based bioprinting fabricates tissues through the deposition of continuous filaments of cell-laden hydrogels. The hydrogel is usually extruded by pneumatic pressure or plunger- or screw-based pressure through a nozzle or needle onto a stationary substrate. Full 3D constructs are formed after layer-by-layer operation[71,72]. The advantages of extrusion-based bioprinting include room-temperature printing, low cost, and good cell survival. However, it is only compatible with high-stiffness materials and has limited resolution. A recent extrusion-based printing study applied self-healing ECM as a printing bath, allowing direct cell printing in the ECM and enabling the fabrication of low stiffness materials[73]. Laser-based bioprinting contains three parts: a pulsed laser source, a ribbon, and a receiving substrate. The laser irradiates the ribbon, leading the liquid biological materials to evaporate and reach the receiving substrate in droplet form. Laser-based bioprinting allows a reasonable high-resolution (~20 μm) patterning and high viability of cells. Nevertheless, it is also a high-cost, cumbersome, and time-consuming

technology[74]. Stereolithography-based bioprinting applies laser in solution containing cells and light-sensitive polymer materials to cause solidification. Theoretically, stereolithography-based bioprinting has the highest fabrication accuracy (~2 μm)[71]. However, residual photocuring reagents and UV lasers have been reported to be cytotoxic and harmful to cellular DNA stability[71,75]. Droplet-based 3D bioprinting was reported by the Bayley group[7,76]. A piezoelectric transducer generates a mechanical pulse and ejects droplets containing cell-laden hydrogel out of the printing nozzle into a lipid-containing oil bath. A single droplet was covered by a lipid monolayer, and multiple contacted droplets formed a droplet–interface bilayer, stabilizing the droplet network. The droplet-printing technique allows the fabrication of soft and biocompatible materials, such as Matrigel, with a high resolution (~50 μm) and viability (>90%)[76]. A prospective advancement in achieving a resolution of 20 μm, enabling the encapsulation of approximately a dozen cells per droplet, can potentially enhance fine structure of printed tissues while maintaining cell viability.

1.3. Implantation for Brain Damage Repairment

1.3.1. Implantation of Dissociated Neural Progenitors

Jong-Hoon Kim and his colleagues conducted an early brain implantation study in 2002 in which mouse embryonic stem cells were differentiated into dopamine neurons these were in turn implanted into the striatum of hemiparkinsonian rats. Extracellular stimulation in the center of the graft resulted in an excitatory postsynaptic potential in both implanted neurons and host striatal neurons, indicating the presence of graft-to-host and graft-to-graft synapses. In addition, a mild improvement in motor asymmetry was observed after treatment[77]. The complexity and neuronal diversity impede the research progress of cerebral cortex repairment. In 2018, a study demonstrated that human embryonic stem cells differentiated from visual cortical cells can be implanted and integrated in the lesioned mouse adult visual cortex. Notably, implanted visional

cortical neurons in the visual cortex demonstrated long-range axonal projections in the adult brain, but much less efficient projection if implanted in the motor cortex. Sparse connections between the graft and host were detected by electrophysiological measurement through a patch clamp[45]. Later research reported that the implantation of human cortical pyramidal neurons into the mouse brain at the neonatal stage demonstrated an integration at adult age. Implanted human neurons displayed long-term synaptic potentiation and sparsely turned neural activity to the visual stimuli given to the mouse. Human neurons demonstrated a juvenile-like dendritic spine structure in the adult mouse cortex, indicating a species-specific neuron-intrinsic developmental feature[78]. Although breakthroughs have been achieved in the last two decades to repair brain damage through implanting human-originated neural cells into mouse brains, the dissociated cell implantation strategy has not fully restored the lesioned structure and the function of the cerebral cortex.

1.3.2. Implantation of Organoids

Miniature brain-like constructs generated from human pluripotent stem cells are known as brain organoids. Former research on organoids provided an unprecedented opportunity to model human brain development and disease *ex vivo*. The first attempt at implanting human brain organoids into adult mouse brains was made in 2018. Organoids with 40–50 days old were intracerebrally implanted into a cavity premade in the retrosplenial cortex of immunodeficient mice. The majority of the mice and grafts survived three months post-implantation. Continuous differentiation, extensive axonal growth, vascularization, and positive neuronal activity were observed in grafted brain organoids in the mouse cortex[79]. Another study conducted in 2022 implanted human cerebral cortical organoids into the somatosensory cortex of neonatal immunodeficient rats, showing that neurons integrate into sensory and forming circuits. Single-cell transcriptomics demonstrated that implanted organoids continued with corticogenesis. Axon tracing and

functional measures indicated that the implanted organoids receive thalamocortical and corticocortical neuronal inputs and cause sensory responses in implanted human-originated neurons. Rats with grafts encoded by a channelrhodopsin-2 optogenetic switch were trained for 15 days to lick water during blue- but not red-laser stimuli in the cortex. Later behavioral assessment of the mice demonstrated a lifted lick frequency during blue-laser activation, indicating that grafts can participate in the host circuit's controlling behavior[80]. Overall, implanted organoids in mouse brains revealed great potential to mature, connect with host brains, and even cause behavioral changes. Nevertheless, grafted organoids fail to produce a natural cerebral cortical structure in the lesion, such as cortical layers and columns, which are critical for higher function and cognition. The uncontrollable differentiation process of organoids might also challenge their therapeutic application in future developments.

1.4. Summary of Works: Implantation of Printed Cortical Tissues

Attempts to implant dissociated neural cells and brain organoids have been made by multiple research groups. Although an integration between the implant and the host was observed in these studies, none produced therapeutic effects and the proper restoration of lost brain tissue structure, such as the cortical layers. To tackle this challenge, structural, and cellular components defined as miniature tissue, resembling the anatomy of lost brain tissue, are likely required for advanced repairment of brain injury, particularly in the case of large tissue damage. Implantation using brain tissues produced from the bioprinting strategy has not yet been reported. In the current project, we applied and advanced a droplet-based bioprinting technique to pattern hiPSC-derived UNP and DNP to form cerebral cortical tissues with the architecture of a simplified two-layer cerebral cortical column. We determined the maintenance of the identity and structure of the deep and upper layers during *in vitro* culture after printing. During this period, we also investigated process

outgrowth, neuron migration, and maturation. Further, this thesis describes the implantation of printed cortical tissues into brain explants, with a thorough measurement of the structural and functional connections between the implant and the host.

The research is presented in three chapters. Chapter 2 focuses on the establishment of protocols to differentiate hiPSCs into two distinct subtypes of neurons—DNs and UNs—as well as their progenitors that resemble the critical cell components in the human cerebral cortex. Chapter 3 narrates the advance of a droplet-in-oil 3D bioprinting strategy that could assemble heterogeneous picoliter volume neural cell-laden droplets into self-standing two-layer networks that can be further transferred and incubated to form living cortical tissues. Chapter 4 describes the implantation of printed cortical tissue into mouse brain explants, with a focus on the structural and functional connections between the implant and the explant. Chapter 6 presents the potential future applications of this droplet-based bioprinting technique, and Chapter 7 reports the details of the materials and methods employed throughout the research. Figure 1.1 shows a schematic to summarize the work.

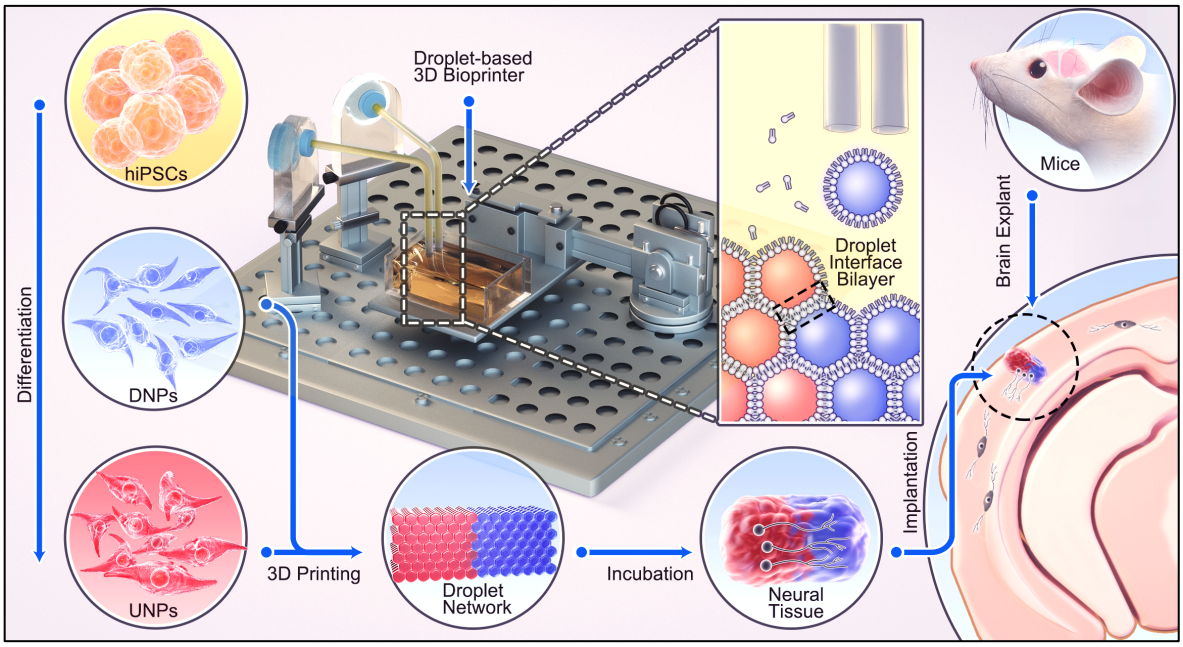

Figure 1.1 Overview of the current thesis.

Patterned 3D printing of droplets containing the hiPSC-derived neural progenitors, DNPs and UNPs, and ECM. The formation of adhesive droplet–interface bilayers (DIBs) secured the patterned network. The printed cerebral cortical tissues were cultured *in vitro* for functional studies and implanted into mouse brain explants. I acknowledge that the drawing refinement of this schematics was provided by Fantastic Colour, a professional scientific drawing service company.

Chapter 2. Cells for Printing

2.1. Chapter Introduction

To fabricate the two-layer cortical tissue, it was first necessary to differentiate the layer-specific cortical neurons. In humans and most other mammals, the cortex has a six-layer architecture that is formed in an inside-first-outside-last order. The early product of cortical neurogenesis is DNs. DNs divide asymmetrically from RGCs and migrate toward the cortical plate from the ventricular zone[54]. A recent study reported a differentiation protocol in which, in the early culture, neural progenitors primarily differentiate into DNs, which can be phenotyped by the expression of deep-layer biomarkers[53,81]. Later, in cortical neurogenesis, RGCs generate neurons that migrate radially into the cortical plate, passing through the DNs to become UNs[54,82]. Boissart and his colleagues addressed the generation of homogeneous UNs *in vitro* through prolonged pro-proliferative culture of neural progenitors, which mimic the *in vivo* late production of UNs from proliferating RGCs[55]. This section focuses on establishing the hiPSC differentiation protocols that generate both UNPs and DNPs for later study.

2.2. Acknowledgments

All work included in this chapter was performed by the author, unless specifically stated in the text. I acknowledge that Dr. Sally Cowley (Department of Pathology, University of Oxford) provided the hiPSC lines used in this study and kindly provided DN differentiation training. Ellina Mikhailova and Linna Zhou (Department of Chemistry, University of Oxford) helped with the cell culture, and A/Prof. Francis Szele (Department of Physiology, Anatomy & Genetics, University of Oxford) and A/Prof. Ming Lei (Department of Pharmacology, University of Oxford)

provided the tissue culture facilities for the hiPSC culture and differentiation. Daniel Catarino and Kaili Liu (Department of Physiology, Anatomy & Genetics, University of Oxford) assisted in the immunostaining experiments.

2.3. hiPSC Characterization

hiPSCs are a type of pluripotent stem cell that can be generated directly from somatic cells. The iPSC technology was initially reported by Shinya Yamanaka, who showed in 2006 that the inducted expression of four transcription factors (Myc, Oct3/4, Sox2 and Klf4) can convert somatic cells into pluripotent stem cells[48]. hiPSCs can propagate indefinitely, providing an unlimited resource for regenerative medicine. The cells also have the potential to differentiate to every other cell type developed from three germ layers (ectoderm, mesoderm, and endoderm), such as neurons[83], heart[49], pancreatic[84], and liver cells[85].

The quality of hiPSCs could vary, and the preservation of pluripotency is critical for the success of subsequent research. In this project, both pluripotent marker expression and hiPSC colony morphology were used to evaluate the preservation of pluripotency. Immunocytochemistry on three critical pluripotent markers, TRA-1-60[86], NANOG[87], and OCT4[88], are shown in Figure 2.1, revealing a high expression of these markers and therefore well-preserved pluripotency. Further morphological examination of hiPSC colonies showed a circular or oval/tear-drop shape with smooth edges, an indicator of an undifferentiated hiPSC population[89].

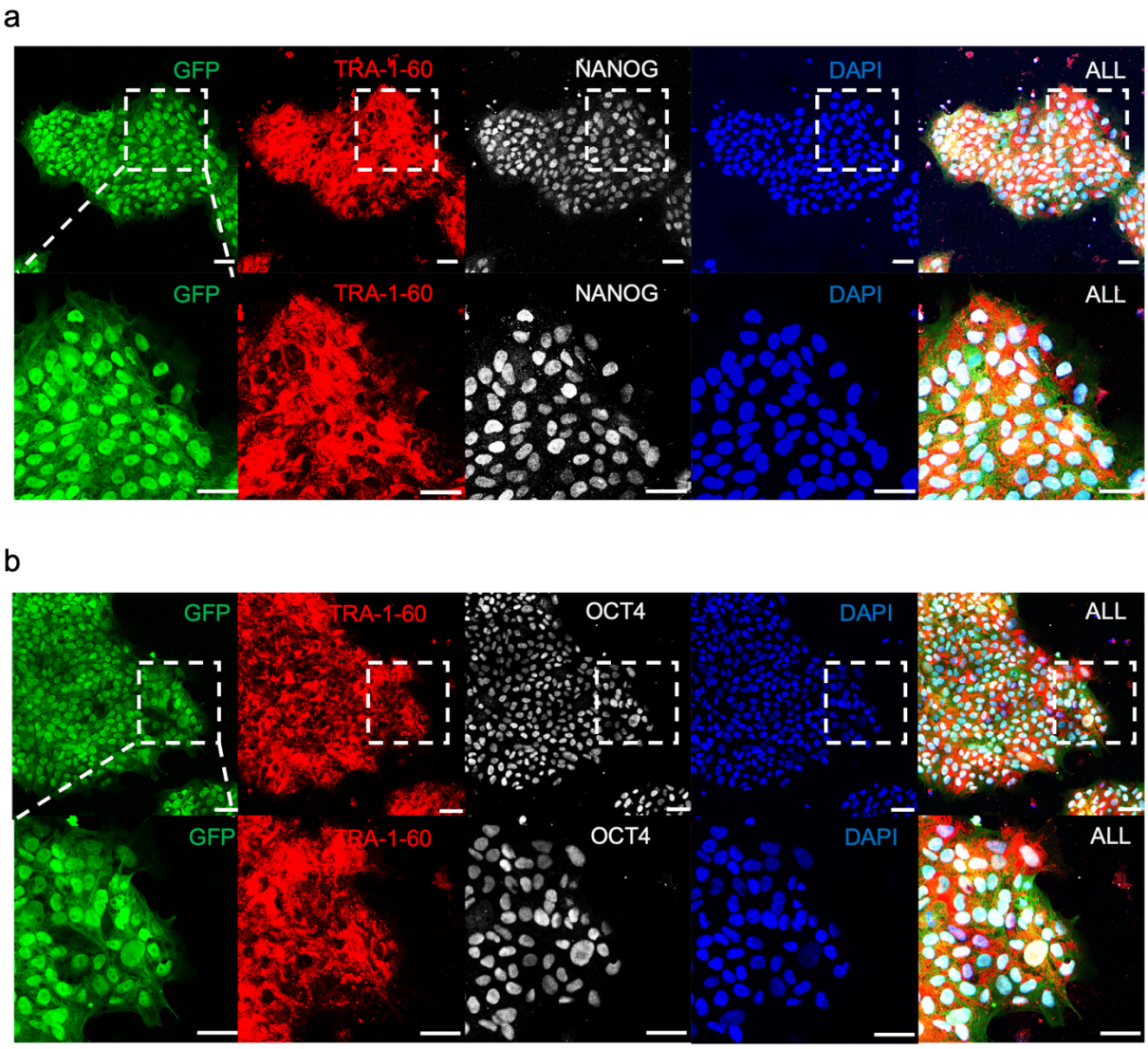

Figure 2.1 Pluripotency assessment of hiPSCs.

a&b. Confocal images of immunostained hiPSC colonies revealed the expression of pluripotent markers TRA-1-60, NANOG, and OCT4 in most cells. Images with a high magnification of the regions indicated by the dashed boxes are shown at the second row. Scale bar: 50 μm.

2.4. DN Differentiation

Neural progenitors refer to the progenitor cells of the CNS that give rise to many of the glial and neuronal cell types that populate the CNS. In 2012, Shi et al. reported a method to generate neural progenitors primarily producing neurons resembling the human cerebral cortex. These NPs are able to sequentially produce both DNs and UNs within approximately four months of the maturation process. Their layer specifies were characterized by the expression of several layer-specific biomarkers, such as CUX1, CUX2, BRN2, CTIP2, and TBR1[52]. Shi's protocol was then optimized and improved by many other groups[90-92]. In the current study, to generate DNs from hiPSCs, we adopted a modified version of Shi's protocol with the application of a dual-SMAD inhibition differentiation strategy[93] to generate neural progenitors in monolayer cultures. Figure 2.2 shows the overall process of DN and UN differentiation. In short, we used a defined neural induction medium (NIM) containing two SMAD inhibitors, LDN193189 and SB431542, to induce hiPSCs into the neural ectoderm lineage. The neural ectoderm cells were then cultured in neural maintenance medium (NMM), which enables the generation of NPs over 19 days *in vitro* (DIV19). Three 1:2 passages were conducted to increase the cell yield and avoid over-propagation in the monolayer culture. Further maturation was achieved by seeding NPs at a low density (100,000 cells/cm^2) and using a neural terminal medium (NTM) containing the γ-secretase inhibitor (DAPT), which blocks the presenilin–γ-secretase complex[94] and prevents the downstream activation of Notch[95]. Inhibition of the Notch pathway switches differentiation from glial to neuronal cell fates. DAPT has been applied in various hiPSC differentiation protocols to facilitate neuron differentiation and maturation[55,96,97]. After 10 days of culture in the NTM, DNs were collected for morphology and identification assessment. Figure 2.3 shows a bright-field image of the DIV 29+ DN culture.

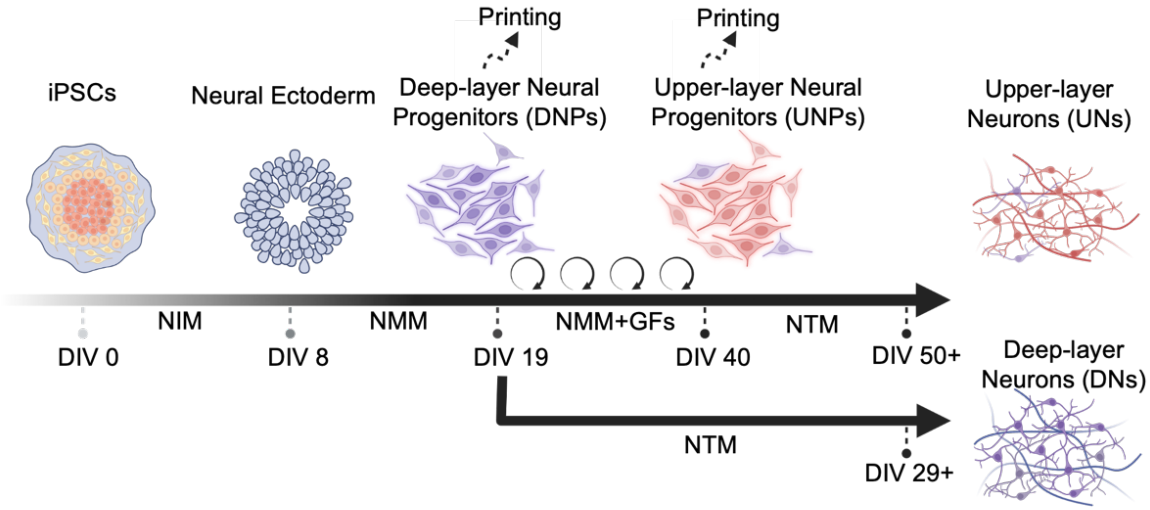

Figure 2.2 Differentiation protocols of hiPSCs to DNs and UNs, via DNPs and UNPs.
DIV 0–8: hiPSC induction and commitment to neural ectoderm lineage; DIV 8–19: continuous differentiation into DNPs; DIV 19–40: DNPs differentiate to UNPs through extended culture in NMM supplemented with FGF-2, EGF, and BDNF. DIV 19–29+ and DIV 40–50+ DNPs and UNPs mature into DNs and UNs, respectively.

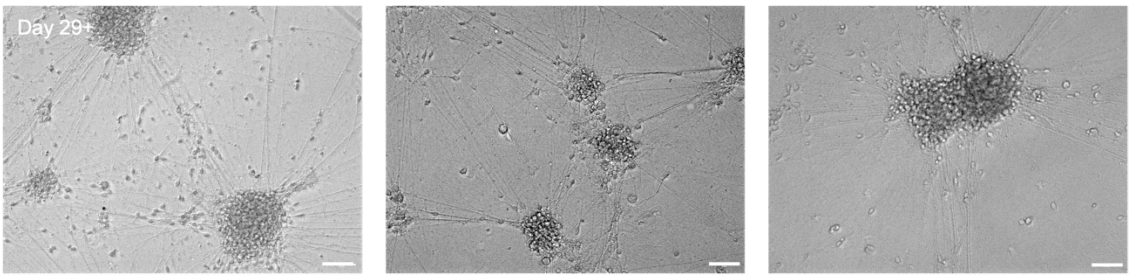

Figure 2.3 Morphology of DNs.
Three example bright-field images of hiPSC-derived DNs revealed mature neural morphology. Scale bar: 50 μm.

2.5. DN Characterization

2.5.1. Biomarker Expression

hiPSC-derived DNs with 10 days of maturation in NTM were used for characterization. Immunocytochemistry is a laboratory method for identifying and visualizing proteins or other antigens in cells via antibodies that specifically recognize the target of interest [98]. In the current study, immunocytochemistry was used to detect and visualize protein biomarkers related to neuronal phenotype and layer identity.

Tbr1, a T box family transcription factor, and CTIP2, a zinc finger transcription factor, were reported as DN-specific markers. Tbr1 is a transcription factor that is highly expressed in glutamatergic early-born cortical neurons. In the Tbr1 mutant cortex, early-born cells form a preplate but do not express markers of Cajal-Retzius, subplate, or layer VI neurons. The Tbr1 mutants also result in abnormalities in the laminar organization of neurons and in the generation of cortical afferent and efferent axons[99]. The Tbr1 expression is primarily positioned in layer V–VI of the cortex in adults and therefore serves as a DN biomarker [100,101]. In comparison, CTIP2 is expressed in a 3-week-old mouse in the middle to deep layers of the cerebral cortex, which most likely correspond to layers V and VI[102]. CTIP2 is required to regulate identity and projection patterns during neurodevelopment, as evidenced by the loss of subcerebral projecting axons in CTIP2 knockout (KO) mice[103].

Drosophila homeobox Cut gene-1 and gene-2 (CUX1 and CUX2) are specific to the pyramidal neurons of the upper layers (II–IV) of the murine cortex, defining the molecular identity of these neurons[104]. Later research indicated that CUX1 and CUX2 play an important role in specifying the dendritic structures of the upper layer neurons of the cortex[105]. Similarly, POU homeodomain

proteins BRN1 and BRN2 co-express in the developing neocortex, both in the migrating neurons and in the late precursors. The double disruption of BRN1 and BRN2 in mice leads to abnormal formation of the neocortex, with reduced production of layer II–IV neurons[106]. SATB2, a DNA-binding protein that regulates chromatin organization and gene expression, functions as a repressor of CTIP2 and a regulatory determinant of corticocortical connections in the developing cerebral cortex. SATB2-mutated neurons acquire expression of CTIP2, while ectopic expression of Satb2 in neural stem cells decreases CTIP2 expression[107]. CUX1, BRN2 expression is specific to cortex layers II–IV[105,106] and SATB2 expression is highly enriched in layers II–III and less enriched in deep layers[108]. Therefore, CUX1 and BRN2 were widely applied as an upper-layer marker, and STAB2 was applied as a middle-upper layer marker[109,110].

Here, our hiPSC-derived DNs showed the features of mature neurons at DIV 29+ with a polarized morphology and the expression of the deep-layer marker CTIP2, but low expression of the middle-upper (SATB2) and upper layer (CUX1 and BRN2) markers (Figure 2.4). These results reveal that the neurons retained a deep-layer cortical identity.

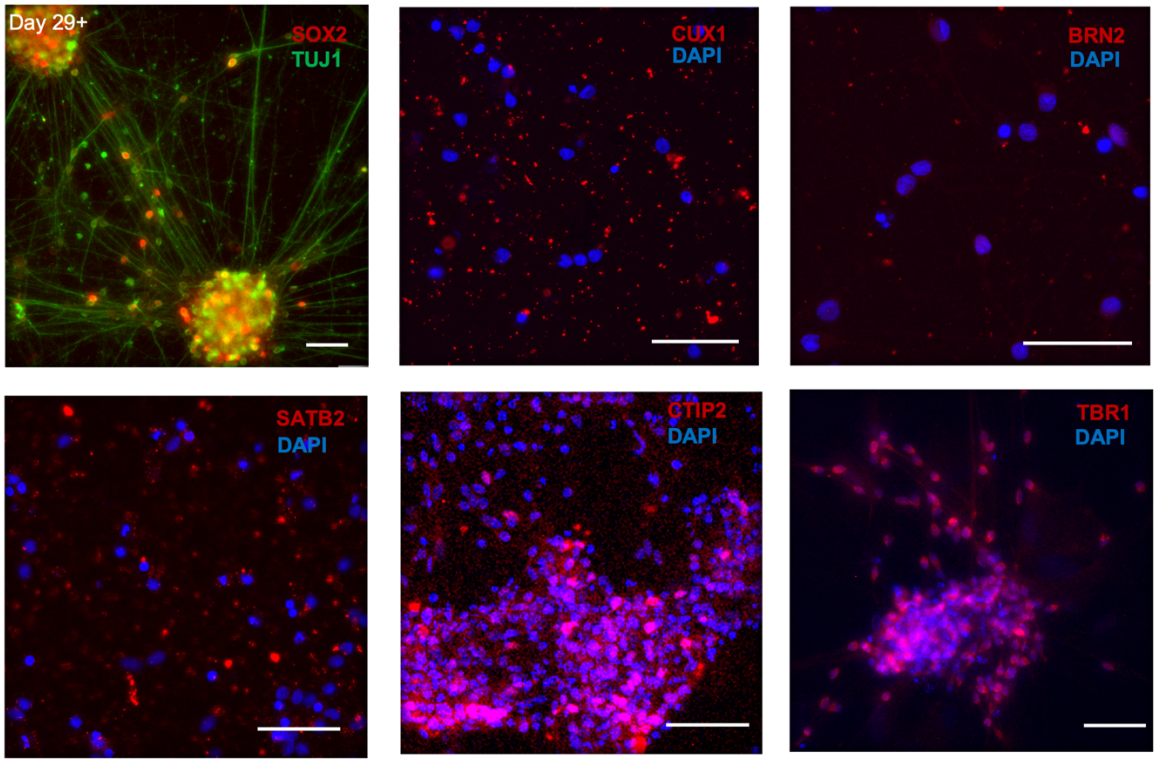

Figure 2.4 Biomarker expression of DIV 29+ hiPSC-derived DNs.

Immunostaining of DNs revealed the expression of neural stem cell marker SOX2, general young neuronal marker TUJ1, the deep-layer markers (CTIP2 and TBR1). The expression of upper-layer markers (CUX1 and BRN2) and middle-upper-layer marker (SATB2) were not found, even when high fluorescence intensity was applied to exhibit the background. For all panels, the scale bar was 50 μm.

2.6. UN Differentiation

During the later stage of cortical neurogenesis, RGC-generated neurons migrate radially into the cortical plate, passing through the DNs to become UNs[54,82]. Boissart et al. reported a method in 2013 to generate homogeneous UNs *in vitro* through the prolonged pro-proliferative culture of NPs, mimicking the *in vivo* late production of UNs[55]. Following this method, we conducted an extended treatment of growth factor cocktails to NPs, resembling the key steps of Boissart's protocol[55]. Unlike the original protocol, we adopted small molecules and a monolayer system for

induction in our neural differentiation protocol to reduce batch-to-batch variations. The growth factor cocktail includes a combination of growth factors that support proliferation (FGF-2 and EGF)[111], and survival and maturation (BDNF)[55,112]. During the treatment, the cells retained progenitor morphology and underwent 8–10 doublings from the beginning of neural induction until DIV 40. Figure 2.2 illustrates the differentiation protocol, and Figure 2.5 shows a representative culture on DIV 31. The UNPs at DIV 40 can be harvested for further maturation culture or cryopreservation. For the maturation of UNPs, growth factors were withdrawn at DIV 40, and further incubation in NTM containing DAPT over 10 days was conducted to generate mature UNs at DIV 50+ (Figure 2.5 and Figure 2.6). Without DAPT, however, the cells showed a nonpolarized morphology, which was similar to the UNPs, indicating a failed maturation (Figure 2.7). The DIV 50+ UNs were collected for further characterization.

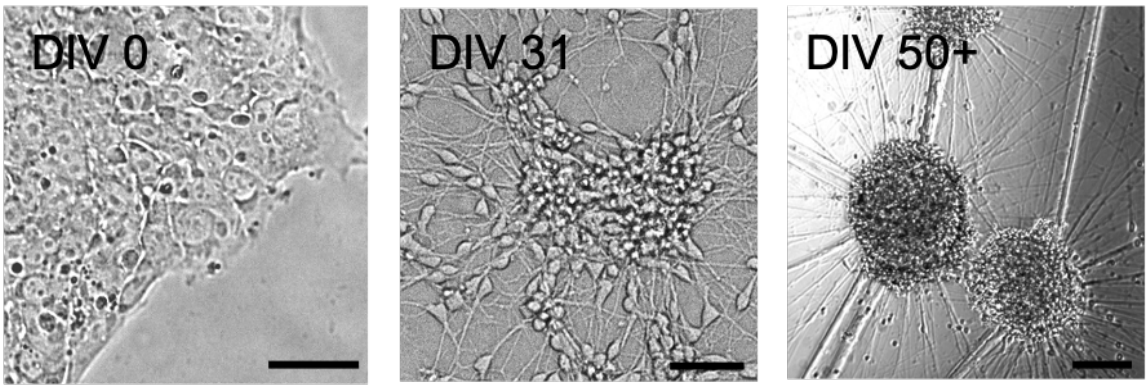

Figure 2.5 Cells at each stage of differentiation

Bright-field images of differentiating neurons at different stages: DIV 0, 31, and 50+ correspond to hiPSCs, NPs, and UNs, respectively. Scale bar: 50 μm.

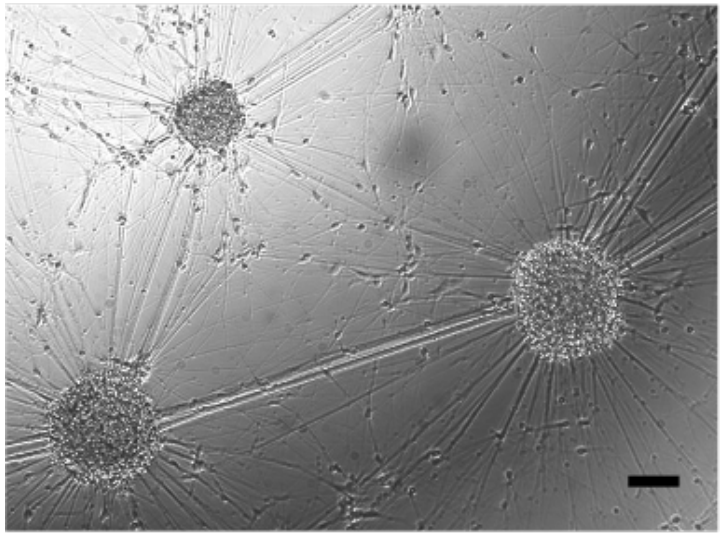

Figure 2.6 Morphology of UNs.

Another representative bright-field image of hiPSCs-UNs revealed mature morphology, as indicated by extensive axon outgrowth. Scale bar: 50 μm.

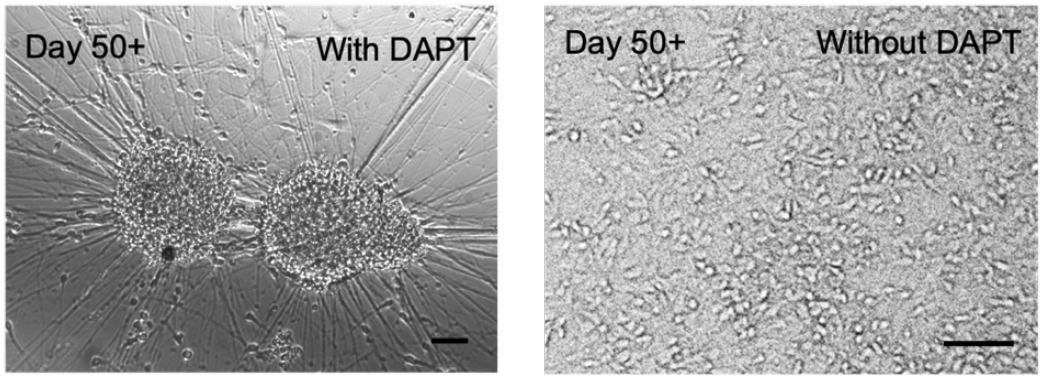

Figure 2.7 Morphology of UNs with and without DAPT treatment.

Bright-field images of DIV 50+ hiPSCs-derived UNs exhibiting neuronal morphologies with (left) and without (right) DAPT treatment during the maturation process. UNs matured in NTM with DAPT were demonstrated in other studies. Scale bar: 50 μm.

2.7. UN Characterization

2.7.1. Biomarker Expression

Similar to the characterization of DNs, the immunocytochemistry of DIV50+ UNs showed the expression of upper-layer markers CUX1, CUX2, and BRN2, and the middle-upper layer marker SATB2, whereas CTIP2 expression was rarely detected (Figure 2.8 and Figure 2.9). Quantitative counting of marker-positive cells was conducted to further understand the differentiated UNs. For each biological replicate, at least three random microscopic views were selected for counting. The proportion of marker-expressing cells was calculated by the number of marker-positive cells divided by the number of cell nuclei visualized by DAPI staining. Results showed that DIV50+ UNs expressed CUX1, BRN2, and SATB2 at proportions of 68 ± 8%, 74 ± 7%, and 70 ± 7%, respectively. By contrast, only 16 ± 4% of the cells expressed the deep-layer marker CTIP2 (Figure 2.10). These results evidenced that the majority of DIV 50+ UNs, unlike DNs, demonstrated upper-layer phenotypes comparable to the neuron population reported in Boissart's protocol[55].

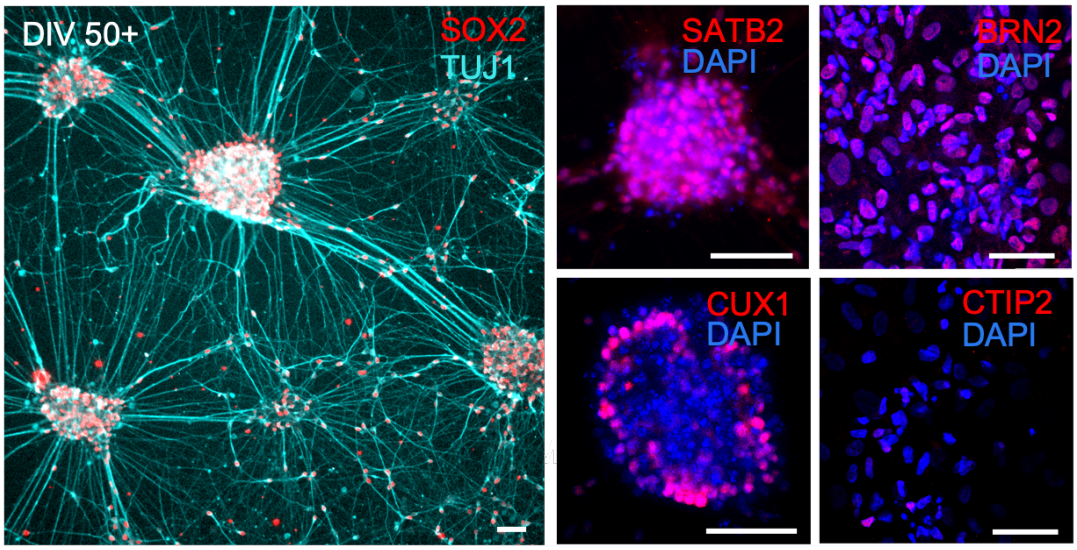

Figure 2.8 Biomarker expression of DIV50+ hiPSC-derived UNs.

Immunocytochemistry analysis of neural stem cell marker (SOX2), general young neuronal marker (TUJ1), middle-upper layer marker (SATB2), upper layer markers (CUX1 and BRN2), and deep layer marker (CTIP2) expression in hiPSC-derived UNs. Scale bar: 50 μm.

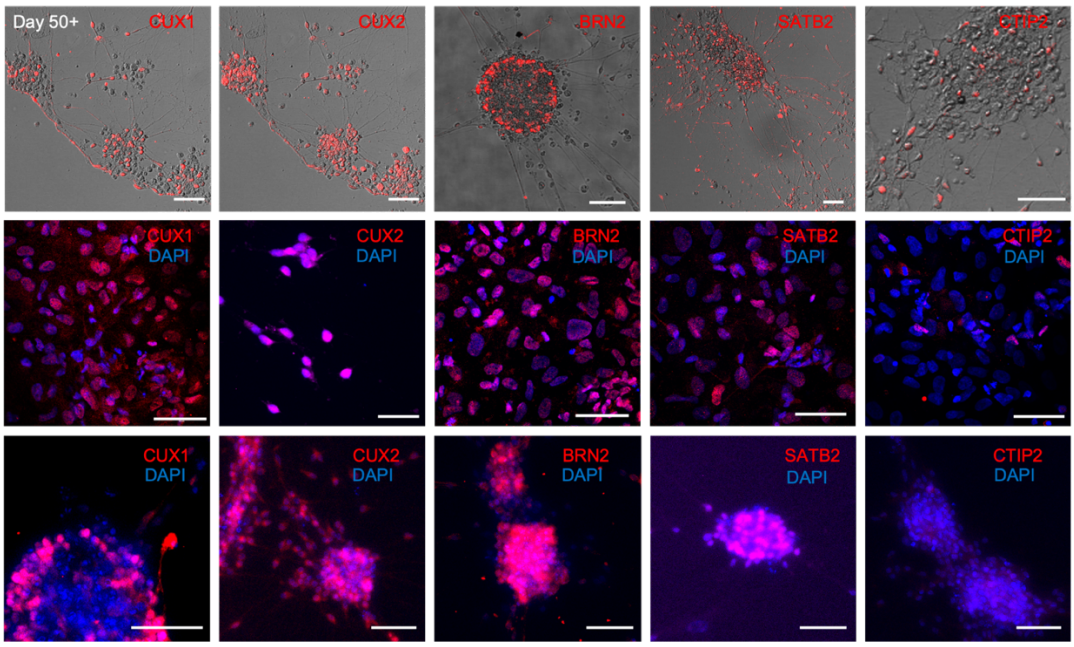

Figure 2.9 Further biomarker characterization of DIV50+ hiPSC-derived UNs.

Fluorescence images of DIV 50+ UNs from three independent experiments are shown in each row. UNs demonstrated the expression of upper-layer markers (CUX1, CUX2 and BRN2) and middle-upper-layer marker (SATB2) but low expression of deep-layer marker (CTIP2). For all panels, the scale bar was 50 μm.

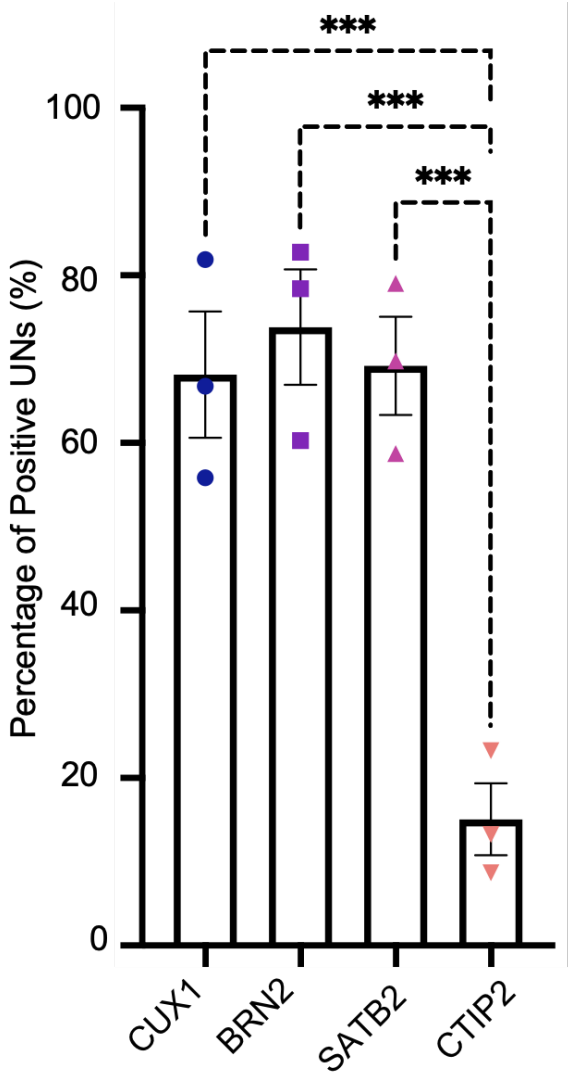

Figure 2.10 Quantitative analysis of biomarker expression in DIV 50+ hiPSC-derived UNs. Biological independent replicates n = 3; one-way ANOVA test.

2.7.2. mRNA Expression

To further confirm the identities of DNs and UNs, we conducted gene expression analysis using a real-time quantitative polymerase chain reaction (RT-qPCR). According to the central dogma, DNA transcript into messenger RNA (mRNA) and then further translate into protein. In the RT-qPCR assessment, mRNA was first reverse transcribed into complementary DNA (cDNA) by

reverse transcriptase from the total mRNA. The total cDNA was then used as the template for the RT-qPCR reaction. Specific cDNA fragments were replicated using designed sequence-specific primers. The cDNA amplification process can be semi-quantitatively detected by a DNA-binding fluorescent dye that binds to double-stranded DNA. An increase in DNA products during PCR leads to an increase in the fluorescence intensity measured at each cycle[113].

In the current study, RT-qPCR showed that the treatment with the growth factor cocktail significantly upregulated CUX1 expression, with a 20- and 22-fold change in DIV40+ UNPs and DIV50+ UNs compared to hiPSCs, whereas no upregulation was detected in DIV19 DNPs. In addition, we did not detect changes in CTIP2 expression in the DIV40 UNPs. By comparison, DIV 47+ UNs in Boissart's original protocol also revealed ~20-fold upregulation of CUX1, along with an ~10-fold increase in CTIP2 expression[55]. PAX6, a neural stem cell marker[114], was identified in DIV19 DNPs, indicating successful cortical neural induction. The expression of PAX6 decreased in DIV40 UNPs and dropped further after maturation in DIV50+ UNs, with ~160-, 12-, and 3-fold expression compared with hiPSCs in DIV19 DNPs, DIV40 UNPs, and DIV50+ UNs, respectively. NESTIN, a neural marker, was upregulated over the differentiation and maturation process from a low level in DIV19 DNPs, and showed a 2-fold increase in DIV40 UNPs and a 7-fold increase in DIV50+ UNs compared with hiPSCs (Figure 2.11)[115].

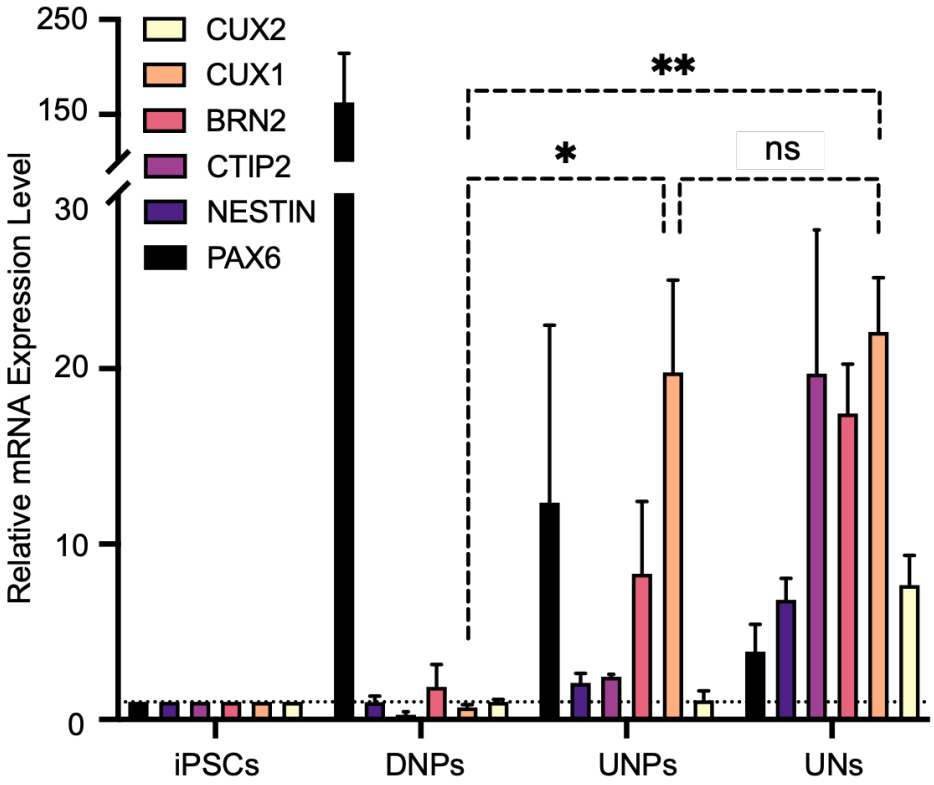

Figure 2.11 Quantitative RT-PCR analysis on different cell types.

Quantitative RT-PCR analysis of upper layer markers (CUX1, CUX2 and BRN2), deep layer marker (CTIP2), neurofilament marker (NESTIN) and neuroectoderm marker (PAX6). Marker expression of the indicated cell types related to hiPSCs. (n = 3; one-way ANOVA test).

2.8. Chapter Conclusion

The differentiation of layer-specific cerebral cortical progenitor cells from hiPSCs served as the essential first step toward fabricating the two-layer cortical tissue. Most mammals' cortexes have a six-layer architecture and are formed in an inside-first-outside-last order. We adapted two hiPSC-neuron differentiation protocols to produce DNs and UNs, which resemble the sequential generation of cortical neurons during corticogenesis[52,55,93]. For the generation of UNs, a pro-proliferation growth factor cocktail (FGF-2, EGF, and BDNF) was applied to NPs for extended culture. The neurons generated from the two protocols were harvested and characterized with their

neuronal and layer-specific biomarker expression. Quantitative PCR was also used to further evidence their layer identities. Both biomarker expression and RT-qPCR studies evidenced the deep-layer and upper-layer identities of DNs and UNs, respectively. The neuronal progenitors giving to DNs and UNs, termed DNPs and UNPs, were therefore collected and cryopreserved for later 3D printing, forming layered cerebral cortical tissues.

Chapter 3.

Three-dimensional Printing of Cerebral Cortical Tissue

3.1. Chapter Introduction

This chapter describes the development of a droplet-in-oil 3D bioprinting technique that was used to pattern networks containing thousands of picoliter volume droplets. These droplets were bound through lipid droplet-interface bilayers (DIBs). These self-standing compartmentalized networks reach millimeter- to centimeter-scale size. Incorporating various types of cells into the network led to the later formation of living tissue.

3.2. Acknowledgments

All work included in this chapter was performed by the author, unless specifically stated in the text. I acknowledge that Dr. Linna Zhou (Department of Chemistry, University of Oxford) provided training for 3D droplet printing and helped with the printer setup.

3.3. Printing Technique Development

The Bayley laboratory established the technique of 3D patterning of droplets in lipid-containing oil baths to generate droplet networks in 2012. Communication between network droplets or the environment was demonstrated through the inclusion of membrane proteins, which allow the

translocation of small molecules[7]. In 2020, the Bayley Group reported forming cell-laden tissue using the droplet-fabrication technique[76].

The primary goal of the current study is to develop a complex shape of droplet-printed tissue, particularly those containing laminar structure, which mimics the six-layer architecture of human and most other mammals' cerebral cortexes. To achieve this, networks need to be precisely ordered in a 3D manner. Micropipetting could only form individual droplets with a diameter over 500 μm, which would be impractical to assemble into complex networks within a reasonable size. Alternatively, microfluidic devices could generate networks composed of picoliter droplets. However, there is little control over the vertical structure of microfluidics-fabricated networks[116]. To attain droplet networks that mimic tissue architecture, we adopted and optimized the droplet-in-oil 3D printing technique in the Bayley laboratory. The 3D droplet printer contains a piezo driver that generates mechanical pulses and ejects aqueous droplets from a printing nozzle into a bath of lipid-containing oil mounted on a motorized micromanipulator. A single droplet network was built up in horizontal layers (Figure 3.1).

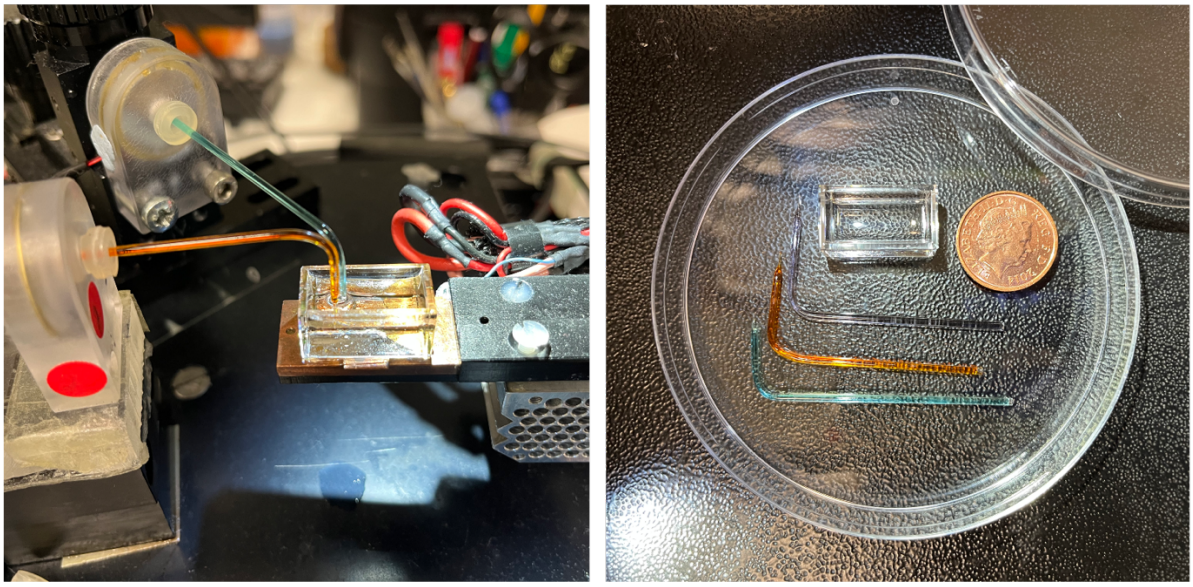

Figure 3.1 The outlook of 3D droplet printer.

The droplet-based 3D bioprinter (left) and various components (right), including the glass printing cuvette and printing nozzles, were compared to a 10-pence coin.

The printing oil bath was composed of 2 mg/mL DPhPC (1,2-diphytanoyl-sn-glycero-3-phosphocholine) in a mixture of undecane and silicone oil AR20 1:4 (v/v). For the printing of small and aqueous-only droplets, a mixture of undecane and silicone oil AR20 1:3 (v/v) can also be used. A network is defined as horizontal cross sections one droplet thick. A custom computer program synchronizes the motion of the oil bath with the ejection of to construct the desired network (Figure 3.2).

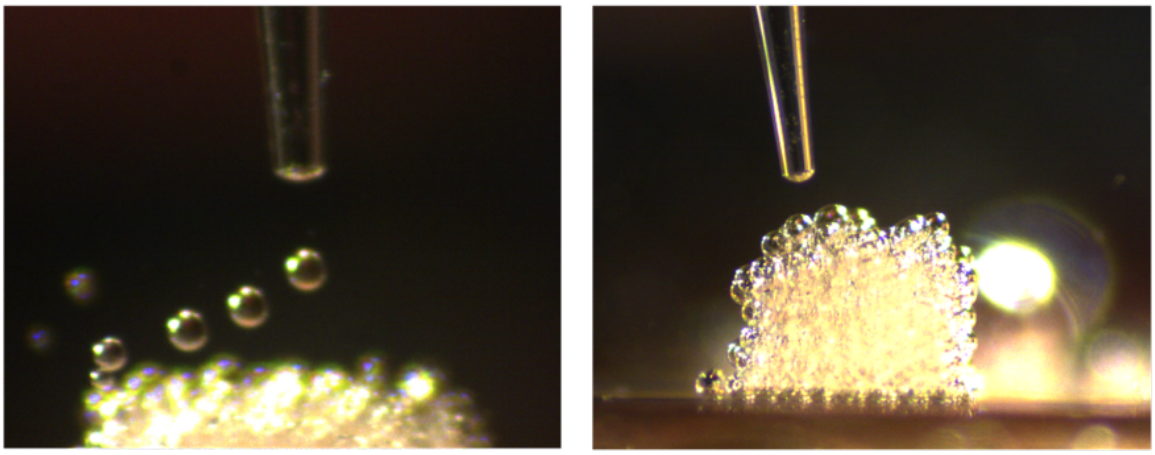

Figure 3.2 Example of ongoing printing.

(Left) Side view of on-going printing. (Right) Side views of printed droplet networks.

The droplets containing water, salt solution, microbeads, ECM, or cell-laden ECM were applied in the current project. Ejected droplets spontaneously acquire a lipid monolayer at the droplet/oil interface, and the contacting droplets formed DIBs[7]. We printed droplet(s) into 8 × 8 × 8 networks with homologous droplets and 12 × 12 × 12 networks with heterologous droplets at an ejection speed of ~1 s^{-1}. RFP-labelled hiPSCs differentiated DNPs, as described in Chapter 2, were applied in the bioprinting of the single droplet and homologues 8 × 8 × 8 network. Commercial available GFP-labeled 3T3 cells and RFP-labeled MDA breast cancer cells were applied to fabricate the 12 × 12 × 12 networks.

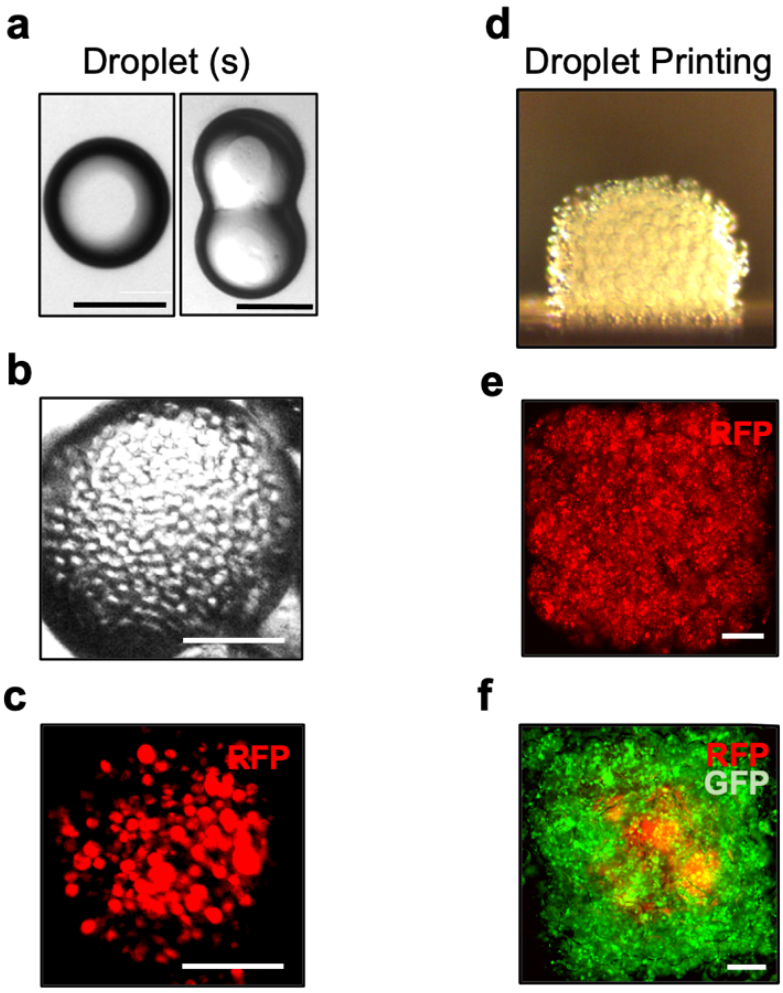

Figure 3.3 Formation of cell-laden network.

a. Bright-field images of a single droplet (left) and a pair of droplets connected through the DIB (right). The droplets consisted of solidified ECM. **b.** and **c.** Image of a droplet printed with RFP-labeled DNPs in the ECM.**d.** Side view of an 8 × 8 × 8 printed droplet network containing DNPs. **e**. Image of a printed droplet network containing RFP-labeled DNPs. **f.** Image of a patterned droplet network containing GFP-labeled 3T3 cells (outer compartment) and RFP-labeled MDA breast cancer cells (center compartment). Scale bars: 'a' ,'b'&'c', 100 μm; 'e' & 'f', 200 μm.

3.4. Adjustment for Layered and Complex Shape Printing

The cerebral cortex, which is composed of layer-specific neurons organized into a six-layer architecture, delivers higher cognition through intricately wired neural circuits[31,32]. Layers I–IV are designated as the upper layer, while layers V–VI are the deep layers. We propose that the

implantation of tissues resembling the cellular architecture of damaged tissue could offer better regenerative effects. Therefore, we advanced the droplet-printing method, allowing us to fabricate a network with layered architecture.

Preliminarily, we spent effort on two-layer tissue printing strategies. An early attempt was made to print an 8 × 8 × 8 droplet network and then reload the printing nozzle to print another 8 × 8 × 8 droplet network directly on top of the first one. However, this strategy produced a 'vertical column structure' in which the droplets tended to fall from the higher layer. To solve this undesirable occurrence, we adapted a parallel printing strategy, in which we printed one 8 × 8 × 8 droplet network on one side and then reloaded the printing nozzle to print a second parallel that contacts the 8 × 8 × 8 droplet network on another side. The two networks automatically anneal due to the formation of DIBs. This method allowed us to stably produce two-layered droplet networks while preserving droplet orders (Figure 3.4).

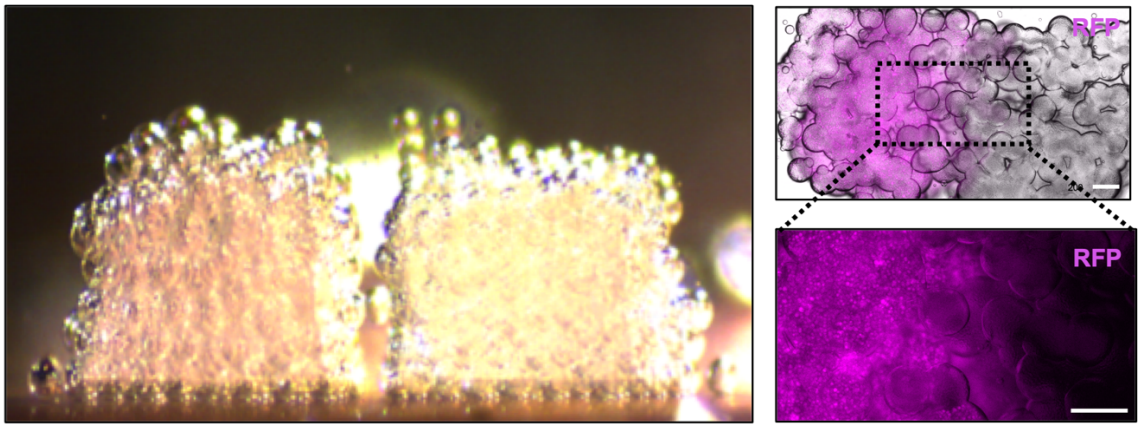

Figure 3.4 Example of printed two-layered droplet network.

Left: Side-view of a printed 16 × 8 × 8 droplet network containing two layers. Top right: Image of a printed two-layer droplet network containing RFP-labeled UNPs (left layer) and unlabeled DNPs (right layer). Bottom right: Fluorescence image of the same two-layer droplet network at higher magnification (indicated by the dashed box). Scale bar: 200 μm.

To demonstrate that our printing technique might produce structures representing all six layers of the cerebral cortex, we applied a layer-by-layer sequential printing strategy. Similar to the strategy for the two-layer network, each layer of the six-layer network, composed of an 8 × 8 × 8 droplet network, was labeled with a different color. One 8 × 8 × 8 droplet network was printed, and then the printing nozzle was reloaded to print the second parallel and contact 8 × 8 × 8 droplet network. This process was replicated six times to generate a continuous six-layer centimeter-scale network (Figure 3.5 and Figure 3.6).

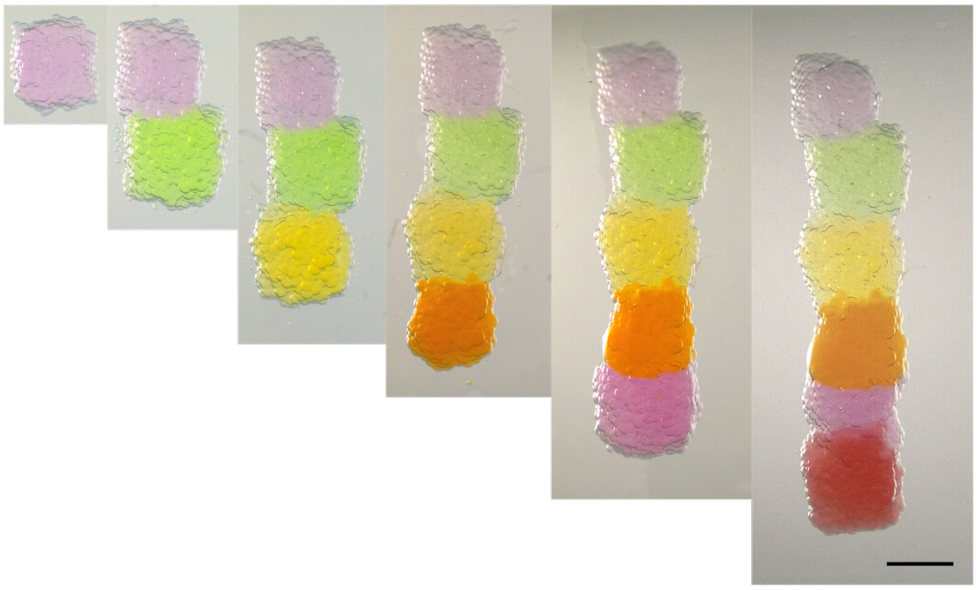

Figure 3.5 Generation of six-layered network.

Sequential generation of six-layered network by droplets containing food dye colored Dulbecco's phosphate-buffered saline (DPBS). Scale bar: 1,000 μm.

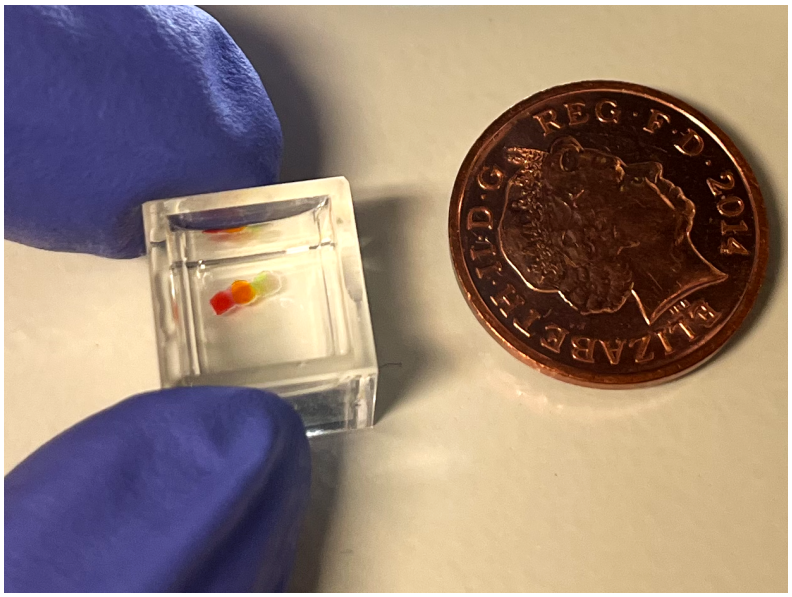

Figure 3.6 The size of six-layered network.

View of the six-layered network in Figure 3.5 compared to a 10-pence coin.

In the real medical scenario, most wounds have irregular shapes. A printing strategy that produces tissues with flexible and designable geometry is preferred for implantation in irregular wounds.

Here, in addition to sub-millimeter scale cubic structures, the printing of centimeter-scale networks with different shapes was achieved. We designed the printing map based on pixelized images of the word 'OXF' and a drawing of 'pigeon' in the customized droplet-printing software. Droplets with a size of ~100 μm were fabricated with a reduced printing speed to facilitate printing precision. The resulting centimeter-size network demonstrated a recognizable shape of 'OXF' and 'pigeon' with desired fine detail at edges (Figure 3.7 and Figure 3.8).

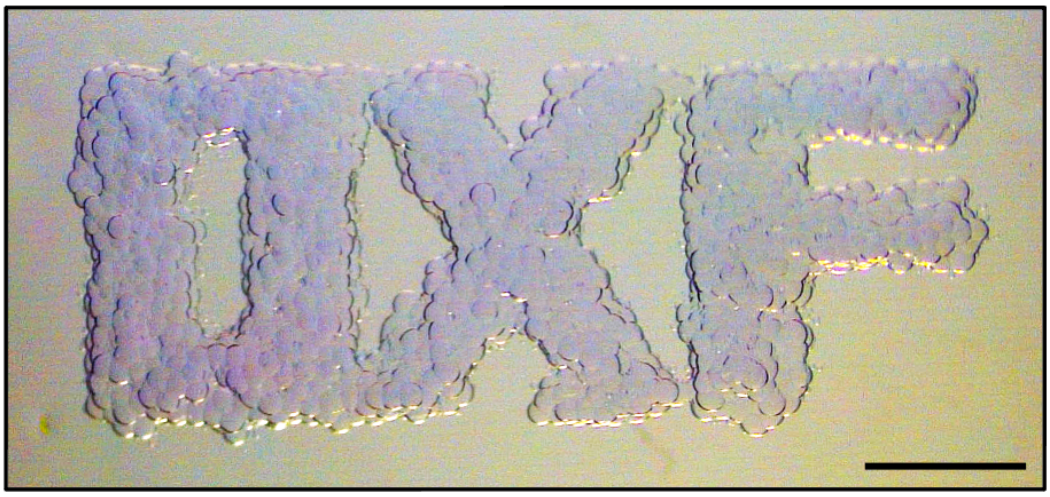

Figure 3.7 Centimeter-sized droplet networks showing 'OXF'.
Scale bar: 1,000 μm.

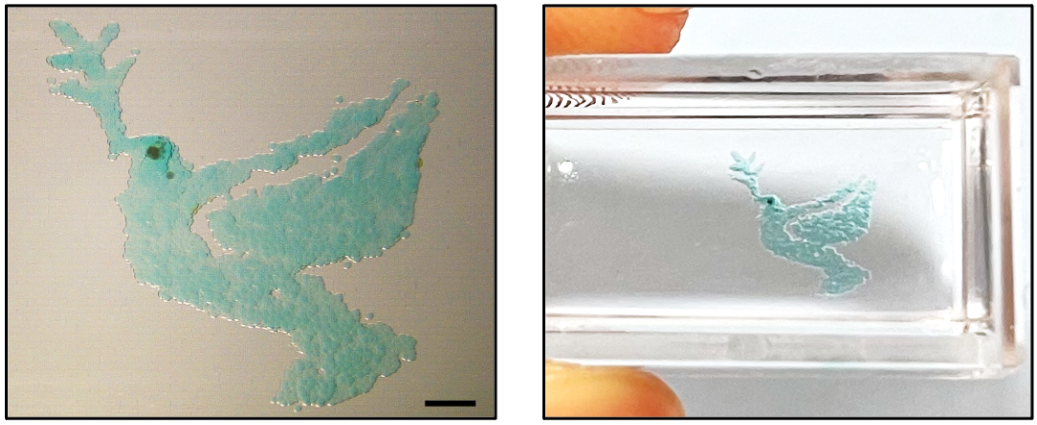

Figure 3.8 Centimeter-sized droplet networks showing a shape of 'pigeon'.
Scale bar: 1,000 μm.

3.5. Adjustment for Cortical Tissue Printing

To fabricate functional cerebral cortical tissues, progenitor cells, DNPs, and UNPs were harvested for printing. Although we demonstrated that our droplet-printing technique is capable of producing six-layered structures, mimicking the complex human cerebral cortex architecture, current hiPSC techniques cannot produce all kinds of neurons representing six layers. Further advances in the generation of layer-specific cortical neurons, along with our droplet printing technique, will enable the fabrication of finer-grained and more realistic 3D *ex vivo* cortical tissues[8,9]. Therefore, in the current study, the cortical tissues were designed as two layers. We printed two 8 × 8 × 8 droplet networks side by side, one containing DNPs and the other UNPs, to give a 16 × 8 × 8 droplet network. The printing of cell-containing ECM led to challenges that are usually absent in water or salt solution-droplet printing. This section further illustrates the adjustments we made to enable the fabrication of sensitive cells, such as neural progenitors, in our droplet printing system.

3.5.1. Printing Voltage

The original droplet printing method is limited to materials with low viscosities and low cell densities[7]. To improve the performance of the formerly reported droplet printer, a piezo driver generating higher output voltages (0–99 V) was applied to eject droplets composed of materials with higher viscosity. In the current study, viscose ECM, Matrigel, was used to embed the cells. The ejected, cell-laden Matrigel-containing droplets were automatically covered by a monolayer of lipids in the oil bath. Two droplets printed next to each other generated droplet interface bilayers, which provided the crucial adhesive force. DIBs are critical for supporting the 3D architecture of printed droplet networks and allowing patterning. The contact droplets are separated from each other and do not exchange ECM or cells.

3.5.2. Printing Nozzle Size

The inner diameters of the printing nozzles were also important in influencing the resulting droplet network. Here, nozzles with ~100 μm were prepared and used to generate droplets with a diameter of ~100 μm. With the same printing nozzle, the size of the ejected droplet could be further adjusted by controlling the pulse amplitude and pulse duration of the piezo.

3.5.3. Printing Nozzle Coating

Nozzle coating also serves as an important part of the adjustment for cell-laden ECM printing. Unlike water droplet printing, ECM-containing droplets experience the issues of ECM content linking into the oil bath without triggering ejection or oil entering the nozzle after each triggered ejection. To solve this challenge, glass printing nozzles were coated with (3-aminopropyl) trimethoxysilane to provide a hydrophilic coating, which prevented both ECM linkage and oil from entering the nozzle.

3.5.4. Printing Temperature

Temperature is critical for printing ECM, particularly the Matrigel used in this study. Matrigel is a type of solubilized basement membrane matrix secreted by Engelbreth-Holm-Swarm (EHS) mouse sarcoma cells. Matrigel mimics the laminin/collagen IV-rich basement membrane extracellular environment found in many tissues[117]. Chilled (4°C) Matrigel retains liquid and was therefore used to embed cells and droplet print in a lipid-containing oil bath. When Matrigel was cultured at 37°C (body temperature), the Matrigel proteins polymerized and produced a solidified 3D structure. Due to batch-to-batch variance, the minimal temperature required for polymerization is not well-defined, but partial solidification was usually observed at ~15°C. To avoid temperature raising and Matrigel polymerization, the printing platform was moved into a cold room so that the whole printing process could be performed in a 4–5°C environment.

3.5.5. Solidification

After printing, the network containing cell-laden Matrigel was solidified by changing the environment to room temperature (RT). During the process, the DIBs between the droplets kept the inner contents separate. Although Matrigel solidification is slow at RT, directly moving the network to 37°C incubation resulted in rapid rupture of the DIBs, leading to droplet fusion. To solve this problem, we applied a stepped-temperature increase protocol. The printed network was first warmed to an intermediate temperature of RT ~25°C for 20 min, whereby partial solidification of Matrigel occurs, but also where the DIBs preserve and separate the droplet contents. The network was then cultured at 37°C, resulting in DIB break and full solidification of Matrigel. This process can generate connected droplets without content mixing (Figure 3.9). A fully solidified network is ready for the subsequent operation of phase transfer.

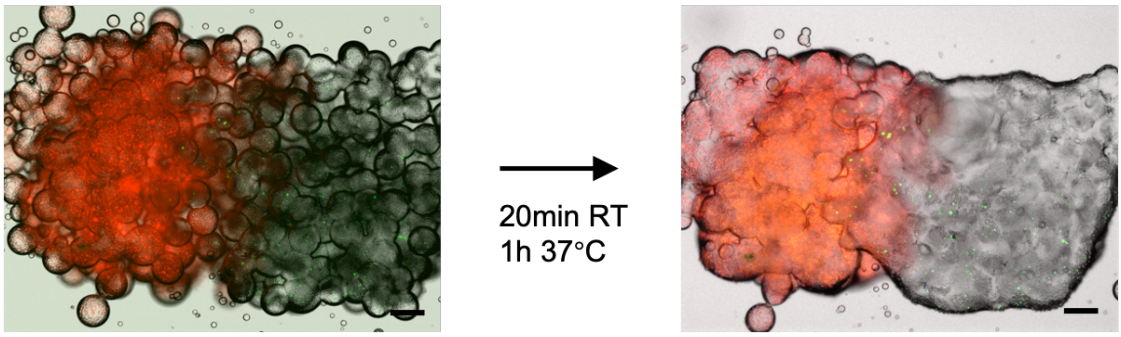

Figure 3.9 Stepped heating procedure.
Fluorescence images of a two-layered droplet network containing RFP-labeled UNPs and unlabeled DNPs. Raising the temperature from RT to physiological temperature facilitated gelation and annealing of printed two-layer network.

3.5.6. Phase Transfer

A droplet network can be transferred from the printing oil to the culture medium without deforming the cell contents or exchanging them between droplets. To achieve this, lipids in the printing oil were exchanged and diluted at least four times using non-lipid printing oil, leading to the lipid decreasing to 1/16 its original concentration. DIBs break and diffuse during this process.

Solidified ECM and cells can retain their morphology without the need for any additional mechanical support. Then, the printing oil was exchanged with the culture medium by dropping the medium into the oil bath. Due to the higher density of the culture medium, the culture medium sinks and occupies the bottom space of the printing vessel. Suspended oil can be removed using micro pipettes. This process can be repeated three to four times to eliminate residual oil. Therefore, this technique allows for the patterning of cells in scaffold-free soft ECM, avoiding the addition of biologically incompatible materials. The DIB-supported architecture can remain for several hours, which enables materials such as Matrigel to solidify. A detailed flow chart of the droplet-based 3D bioprinting process was demonstrated in ***Figure 3.10***.

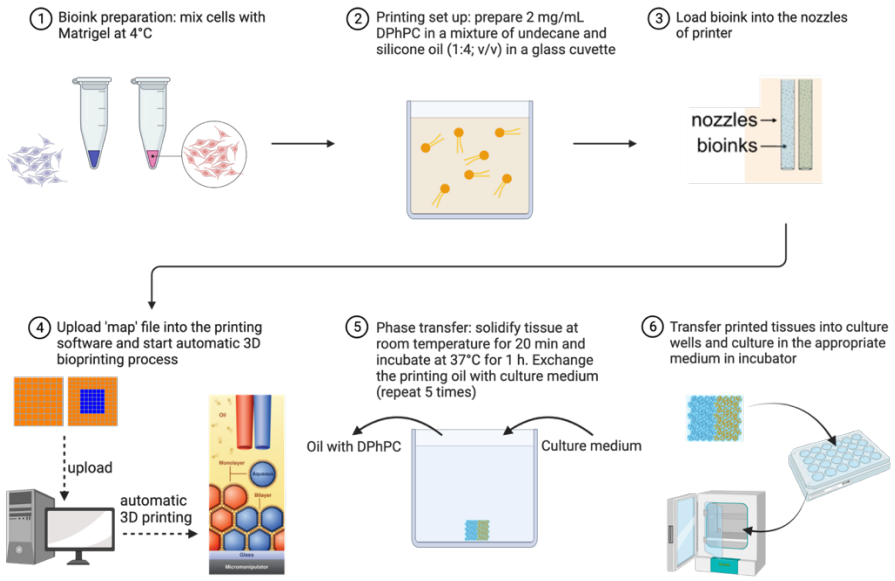

Figure 3.10 A flow chart of the droplet-based 3D bioprinting Proce[7,76,118].

3.5.7. Development of Neural Cell-laden Droplet Network

We next investigated whether we could use our printing technique to fabricate 3D neural tissue to resemble the human cerebral cortex. First, we harvested a 2D culture of DIV19-21 human iPSC-derived DNPs, as described previously. The harvested DNPs were re-suspended in Matrigel at a

cell density of 4–5 × 10^7 mL^{-1}. By applying the droplet-printing technique, we constructed 8 × 8 × 8 droplet networks containing DNPs (Figure 3.11). Following Matrigel solidification and phase transfer, these printed networks were cultured with the corresponding medium for further maintenance and differentiation.

Instead of mature neurons, progenitors were used because they were less sensitive to the dissociation procedure from 2D cultures than mature neurons. For the first week of post-printing culture (WPP), the cortical tissues were incubated in NMM supplemented with a combination of growth factors that support proliferation (FGF-2 and EGF)[111], and survival and maturation (BDNF)[55,112].At the end of 1 WPP, the growth-factor supplemented NMM was replaced with NTM to encourage the maturation of the cortical tissues. A medium change was conducted every 3–4 days. The tissues were harvested at 2, 4, and 8 WPP and assessed for morphology, cell migration, process outgrowth and gene expression. A previous study also demonstrated a high viability, polarization, and process outgrowth of printed DNPs on the next day post printing[119]. Antibiotics, such as penicillin-streptomycin, are usually used since the first day of printing to avoid bacterial contamination. We also found that applying 10 μM Rock inhibitor (Y-27683) for the first 3 days post printing can reduce apoptosis and improve cell survival. The next chapter describes the further characterization of droplet-printed cortical tissue.

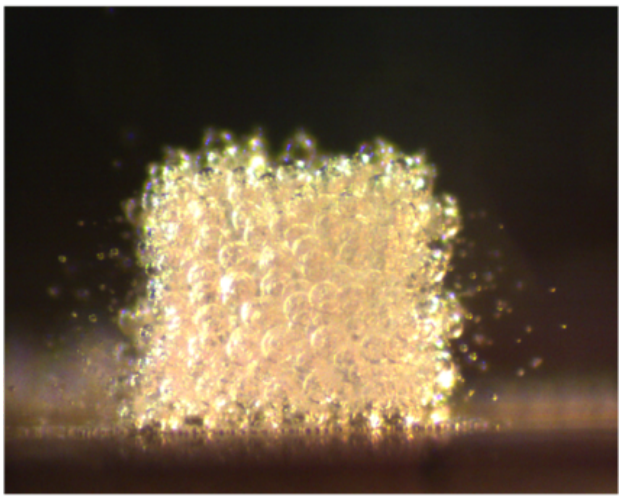

Figure 3.11 Side view of a droplet printed single-layer cortical network.

3.5.8. Development of Neural Cell-laden Two-layer Droplet Network

Here, we used the droplet printing technique to fabricate tissues comprising simplified cerebral cortical columns. Instead of all six layers, we generated cerebral cortical tissues with two layers, due to the absence of hiPSC differentiating protocols generating all cortical cell types.

To collect both DNPs and UNPs for printing at the same time, these differentiated neural progenitors were cryopreserved for long-term preservation. Three to four days prior to printing, the DNPs and UNPs were thawed at the same time and cultured for recovery. To generate a layered network, we printed two 8 × 8 × 8 droplet networks side by side, one containing DNPs and the other UNPs, to give a 16 × 8 × 8 droplet network (Figure 3.9). Droplets at the interface of two networks formed DIBs. A modified solidification process was applied to facilitate the two-layer annealing. Instead of moving the printed network into an RT environment, and without moving the network out of a 4°C cold room environment, we placed the printing vessel-containing networks in a room-temperature water bath for 20 min before transferring them to a tissue culture incubator at 37°C for 1 h. This approach avoids insufficient network annealing caused by motional

disturbance. Subsequent phase transfer was conducted using the method described above. The phase transferred two-layer cortical tissues were cultured in the corresponding culture medium for up to 8 weeks. A medium change was conducted every 3–4 days.

The developed human cortex contains intracortical circuits, which the upper-layer cortex generates/receives process to/from the deep layer to form a complex logical circuit[31,32]. Therefore, it is interesting to investigate the interaction between DNs and UNs in our 3D-patterned cortical tissue. We expected that the DNPs and UNPs would further differentiate during post-printing culture to give the corresponding mature neurons, DNs and UNs, in the layers where they were printed. To determine whether (1) the two layers were preserved during post-printing culture and (2) the DNPs and UNPs were converted to DNs and UNs, we harvested and printed two-layered cortical tissues at 2, 4, and 8 WPP and assessed for morphology, cell migration, process outgrowth, and gene expression.

3.6. Chapter Conclusion

To construct droplet networks resembling a simplified human cerebral cortex. We advanced a formerly established droplet-in-oil 3D printer. This approach can fabricate networks with droplets ejected by piezo actuation in a lipid-in-oil phase. To attain accurate networks, the printing process was assisted by customized software. A single 3D network was attained by assembling thousands of printed picoliter volume droplets in oil. Two-layered and six-layered networks were achieved by printing individual networks side by side sequentially. DIBs at the interface of two layers annealed the networks. Centimeter-scale networks with complex outer shapes, such as the words ‘OXF’ and ‘pigeon’, were also developed by elaborating computer-assisted design and printing speed.

Printing technology was also advanced to fabricate droplets containing cell-laden ECM. Sensitive cells, such as DNPs and UNPs, were harvested and printed into single- or two-layered networks. Following solidification and phase transfer, these fabricated networks formed integrated living tissues. The produced tissues can be cultured in at least 8 WPP. The next chapter provides a further characterization of these tissues.

Chapter 4. Characterization of 3D Printed Cortical Tissues

4.1. Chapter Introduction

In the current project, we used an advanced droplet printing technique to fabricate tissues comprising simplified cerebral cortical columns. The simplified two-layered cortical columns were composed of hiPSC-differentiated DNPs and UNPs. To investigate the subsequent self-regulation of printed neural progenitors in 3D pattern tissues. Printed tissues with different culture times (2, 4, and 8 WPP) were harvested for various assessments (Figure 4.1). This chapter focuses on the maturation, neuronal process outgrowth and migration, and spatial-temporal expression of general and layer-specific neural biomarkers in these printed cortical tissues.

4.2. Acknowledgments

All work included in this chapter was performed by the author, unless specifically stated in the text. I acknowledge that Dr. Linna Zhou (Department of Chemistry, University of Oxford) provided training in 3D droplet printing, cryostat, and tissue staining and analysis. Kaili Liu and Daniel Catarino (Department of Physiology, Anatomy & Genetics, University of Oxford) provided helps in immunostaining. A/Prof. Francis Szele (Department of Physiology, Anatomy & Genetics, University of Oxford) provided the tissue culture, tissue section, and tissue staining facilities.

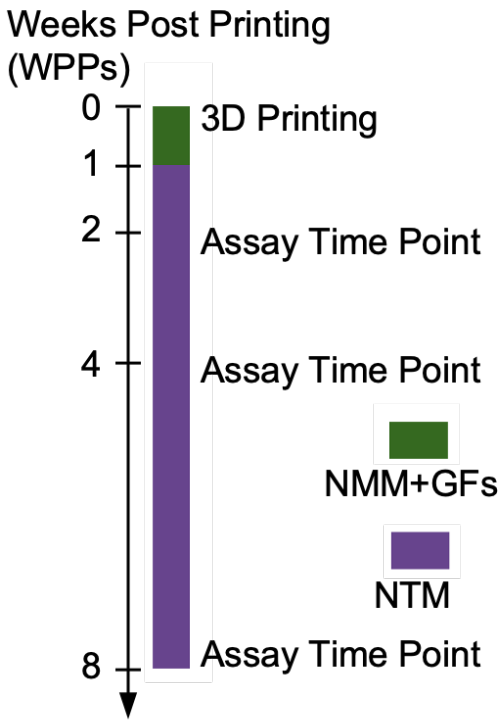

Figure 4.1 Schematic showing the tissue printing and assessment timeline.

Timeline for the fabrication and *in vitro* culture of droplet-printed cerebral cortical tissues. Cortical tissue was bioprinted at 0 WPP and cultured in NMM+GFs until 1 WPP. The tissues were incubated in NTM from 1 to 8 WPP. Fabricated tissues were collected and investigated at 2, 4, and 8 WPPs. More details are described in the Methods section.

4.3. Characterization of Single Deep-layer Cortical Tissue

4.3.1. Morphology

Droplets containing DNPs were printed as 8 × 8 × 8 square networks, which were then phase transferred into a culture medium for incubation. We observed a gradual transformation of the square network to sphere-shaped tissue over the first two weeks of incubation (Figure 4.2). Longer culture leads to protuberance formation on the surface of cortical tissue, presumably caused by proliferation and further differentiation in the protuberance region.

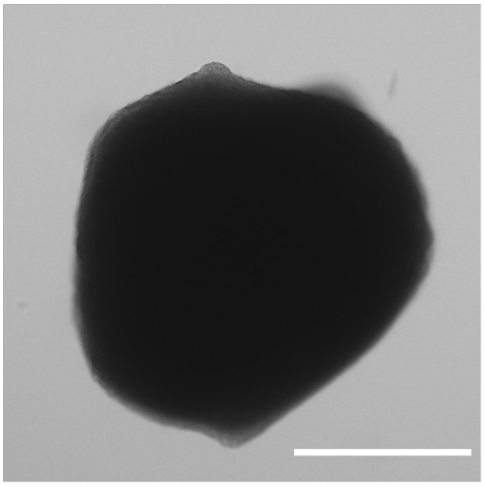

Figure 4.2 Bright-field image of 2 WPP single-layer cortical tissue containing DNs.
Scale bar, 200 μm

Identifying neuronal morphology in printed single-layer tissue is challenging, as all neurons express genetically encoded fluorescent proteins, such as red florescence protein or green fluorescent protein (RFP and GFP), and general neuronal markers. Direct epifluorescence or confocal microscopic observation makes it difficult to distinguish one neuron from the rest of the population. To solve this issue, we printed deep-layer cortical tissues with a DNP population with sparse GFP labeling. In this particular GFP-labeled DNP line, only 5–10% of the cells remained GFP positive after neural differentiation. This phenomenon is possibly caused by the lentivirus-mediated insertion of the GFP encoding sequence into a DNA region that is active in hiPSCs but not in neuronal cells, thereby impeding the GFP expression in the latter. These features allowed us to avoid over-crowding the fluorescence signals and to identify GFP-positive neurons in cortical tissues from other unlabeled areas. A 3D-reconstructed confocal Z-stack scanning image of printed deep-layer cortical tissue with 8 WPP incubation is shown in Figure 4.3. The green color represents the GFP-labeled DNs. These DNs demonstrated a mature morphology with long processes, indicating that DNPs further differentiated and matured after printing and incubation.

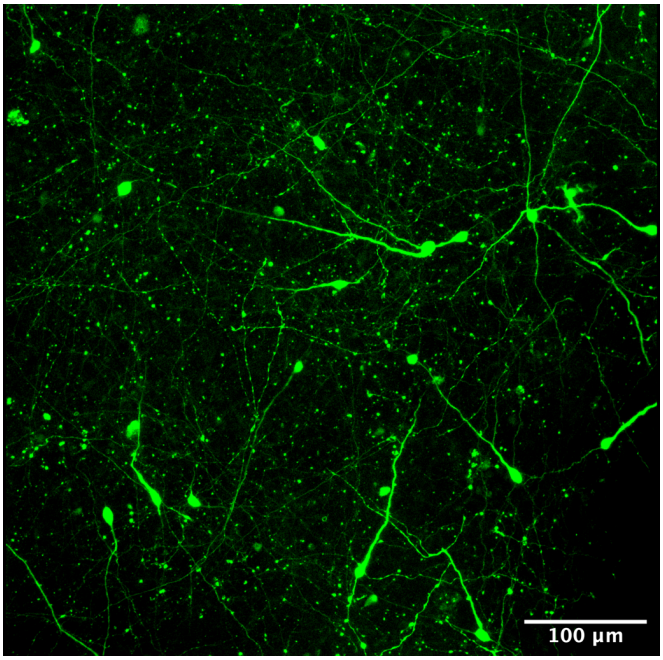

Figure 4.3 Neurons in a printed deep-layer cortical tissue.

Three-dimensional reconstruction of confocal Z-stack scanning image for printed deep-layer cortical tissue with 8 WPP incubation. The green color represents the GFP-labeled DNs.

Comparable results were also reported in former research from the Bayley lab[119]. Processes were observed using the living cell fluorescent dye (Calcein AM) in a 14-day post-printing tissue with low cell density.

4.3.2. Biomarker expression

The cellular behavior of neural progenitors in 2D and 3D environments could be distinctive. Although previous reports have shown that neural progenitors in 3D fabricated tissue can further mature and express general neural markers such as TUJ1 and MAP2 [119], the cortical layer identity of printed cells has not been described. Here, we applied immunohistochemistry to further characterize deep-layer cortical tissues fabricated from DNPs. The printed tissues were incubated for 2, 4, and 8 weeks in the culture medium, as indicated in Figure 4.1, and harvested, fixed, and sectioned by cryostat into 30 µm thick slices for immunostaining. Representative cortical tissue

at 8 WPP was sectioned and immunostained to reveal the tissue structure and the cellular composition by visualizing the following neural markers: stem cell marker SOX2, general marker of young neurons TUJ1, deep-layer markers (CTIP2 and TBR1), and upper-layer marker CUX1 (Figure 4.4). CTIP2/TBR1-expressing DNs and sparse CUX1-expressing UNs were observed, which indicates that DNPs primarily generate DNs, although a small proportion still produce UNs. These results are comparable with *in vitro* differentiated human cortical neurons[53] and brain organoids[120].

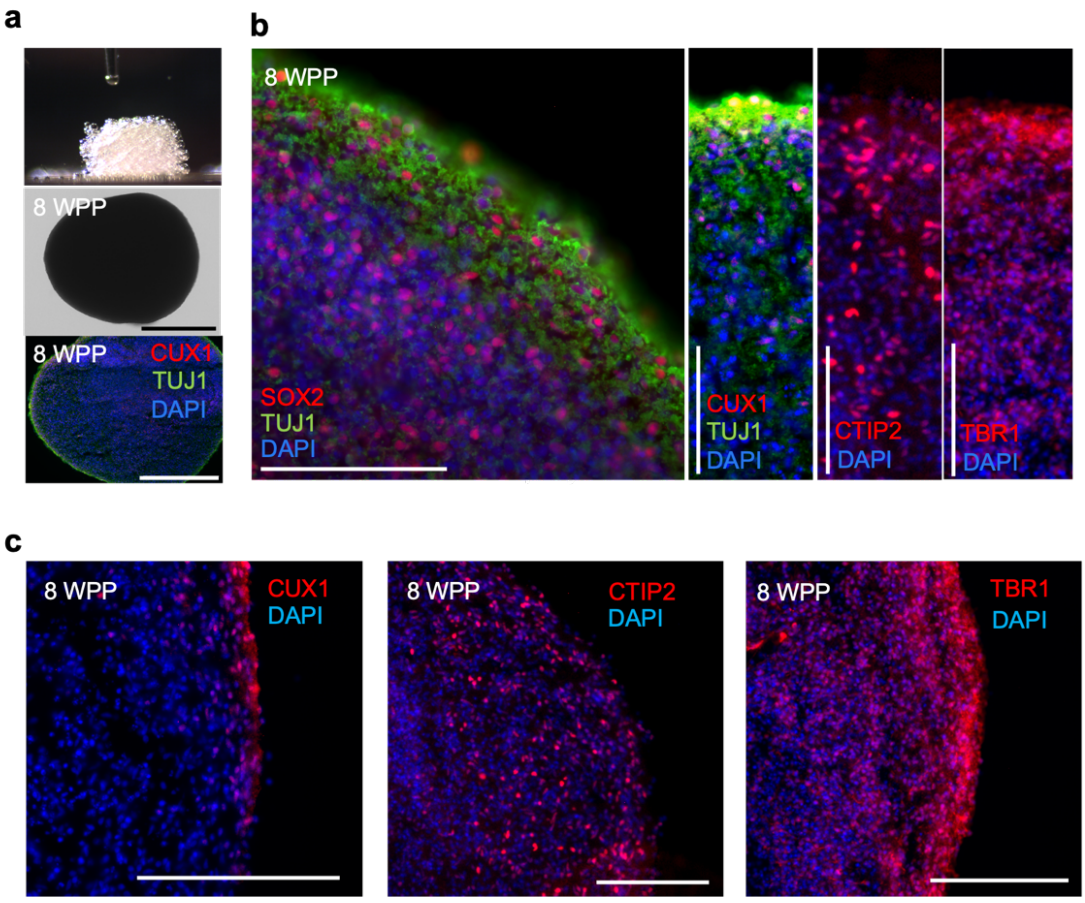

Figure 4.4. Characterization of droplet-printed deep-layer cortical tissues.

a. Side view of printing process (top), bright-field image of the deep-layer cerebral cortical tissue at 8 WPP (middle), and immunostaining of sectioned 8 WPP tissue (bottom). **b.** Fluorescence images of sectioned 8 WPP deep-layer cortical tissues showing the expression of stem cell (SOX2), young neuronal (TUJ1), and layer-specific markers (CUX1, CTIP2 and TBR1). Scale bars: 100 μm. **c.** Zoom out fluorescence images of sectioned 8 WPP deep-layer cerebral cortical tissues exhibiting the abundant expression of the deep layer markers (CTIP2 and TBR1) and the sparse expression of upper-layer marker (CUX1).

4.4. Characterization of Single Upper-layer Cortical Tissue

4.4.1. Morphology

Similar to deep-layer cortical tissue, droplets containing UNPs were printed as an 8 × 8 × 8 cube network, which was then phase transferred into culture medium for later incubation. A comparable transformation from a cube shape to a sphere shape was also observed over the first two weeks of incubation. No apparent morphological difference was found between printed deep-layer tissue and upper-layer cerebral cortical tissue.

4.4.2. Biomarker Expression

Immunohistochemistry was used to characterize the upper-layer cortical tissues formed by 8 × 8 × 8 droplet networks containing DIV 40+ UNPs. The printed tissues were incubated 2, 4, and 8 weeks in the culture medium, as indicated in Figure 4.1, and harvested, fixed, and sectioned by cryostat into 30 μm thick slices for subsequent immunostaining. Comparable to deep-layer tissues, sectioned and immunostained upper-layer tissue at 8 WPP revealed the expression of the stem cell marker SOX2 and a general marker of young neurons TUJ1, indicating their identity of young neuronal cells. However, upper-layer tissues, unlike their deep-layer counterparts, demonstrated sparse CTIP2-expressing DNs and enriched CUX1-expressing UNs population. The majority of cells expressed the upper-layer marker CUX1, which indicates that printed UNPs primarily generated UNs, comparable with the process of 2D *in vitro* UNP maturation.

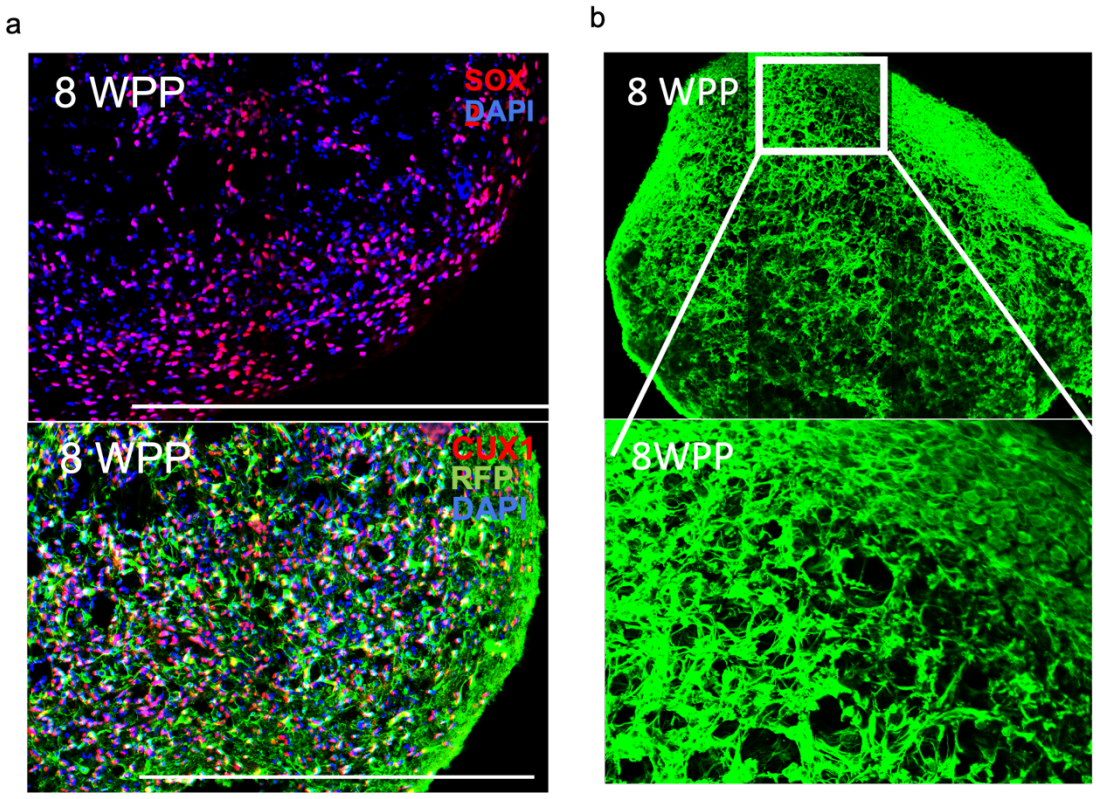

Figure 4.5 Characterization of droplet-printed upper-layer cortical tissues.
a. Fluorescence images of sectioned 8 WPP upper-layer cortical tissue showing the expression of stem cell (SOX2) and layer-specific markers (CUX1). Scale bars: 500 μm. **b.** Fluorescence images of sectioned 8 WPP upper-layer cortical tissue showing the expression of a young neuronal marker (TUJ1). The white line box indicates the magnified area shown in the bottom image.

4.5. Characterization of Two-layered Cortical Tissue

4.5.1. Morphology

To generate cortical tissues with two layers, we printed two 8 × 8 × 8 droplet networks side by side, one containing DNPs and the other UNPs, to give a 16 × 8 × 8 droplet network. We expected that the DNPs and UNPs would further differentiate during post-printing culture to give the corresponding mature neurons, DNs and UNs, in the layers where they were printed. To determine whether (1) the two layers were preserved during post-printing culture and (2) the DNPs and

UNPs were converted to DNs and UNs in a common medium, we characterized the printed tissues at different differentiation time points (2, 4, and 8 WPP).

The two-layered network was initially printed into a cuboid (16 × 8 × 8). Subsequently, incubation of the network led to transformation toward an ellipsoid. After two weeks of culture, the printed cortical tissues remained in a desired two-layered architecture, as illustrated by bright-field images (Figure 4.6) and immunofluorescence images with a combined DAPI-stained cell nucleus and RFP-labeled UNPs (Figure 4.7). Longer culture results in the formation of protuberances on the surfaces of two-layer cortical tissues like these previously observed in single-layer tissue made from DNPs or UNPs.

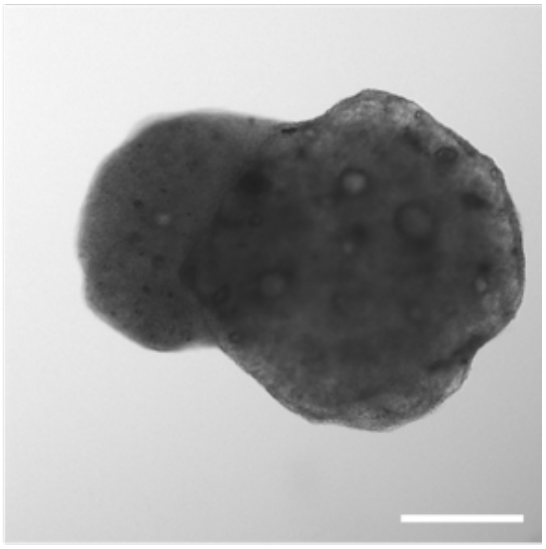

Figure 4.6 Bright-field image of 2 WPP two-layered cortical tissue printed using UNs and DNs. Scale bar: 200 μm.

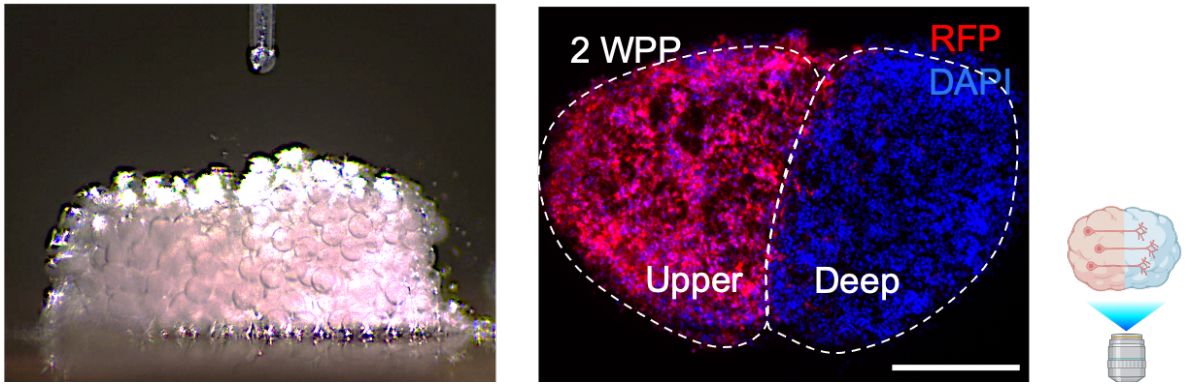

Figure 4.7 Printing of two-layer cortical tissues.

Side view of a two-layer cortical tissue printing process (left), and fluorescence images of a sectioned 2 WPP two-layered tissue (right). Layers were distinguished by the colocalization of RFP-labeled UNs and DAPI-labeled both UNs and DNs nuclei. Scale bars: 500 μm.

4.5.2. Process Outgrowth and Cell Migration

Neuronal process outgrowth and migration are two critical developmental phenomena of cortical neurogenesis. To understand the self-regulation of printed two-layer cerebral cortical tissues, RFP-labeled UNPs and unlabeled DNPs were used to fabricate the two-layer cortical tissues. By applying direct fluorescence imaging, nucleus staining, and immunostaining, we can identify the processes of outgrowth and cell migration between the two layers. As an essential step before further analysis, immunostaining of sectioned two-layer cerebral cortical tissues revealed that the majority of cells in both layers committed into a neural lineage, evidenced by their expression of neuronal marker TUJ1 and the neural stem cell marker SOX2 (Figure 4.8).

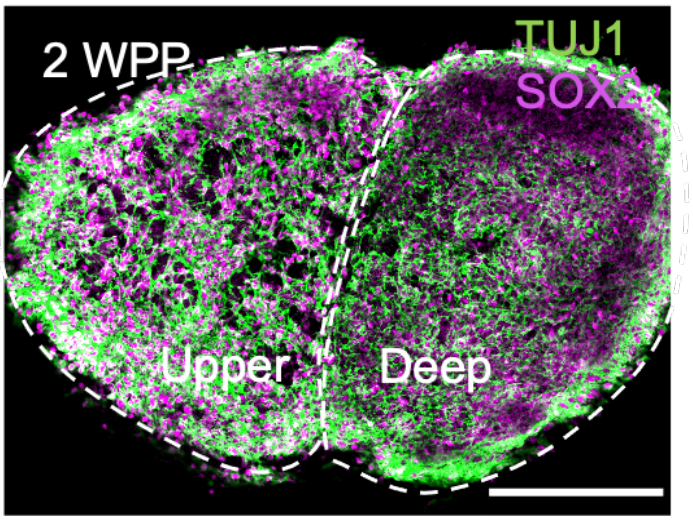

Figure 4.8. Two-layer cortical tissues showing the expression of TUJ1 and SOX2.
Fluorescence images of a sectioned 2 WPP two-layer tissue showing the expression of neuronal markers (TUJ1 and SOX2). Scale bar: 200 μm.

For process outgrowth, confocal Z-projection scanning was used in a two-layered tissue at 8 WPP, revealing that most of the RFP-labeled UNs had acquired a polarized morphology with long processes, suggesting that neural differentiation and maturation had occurred in the printed tissue (Figure 4.9).

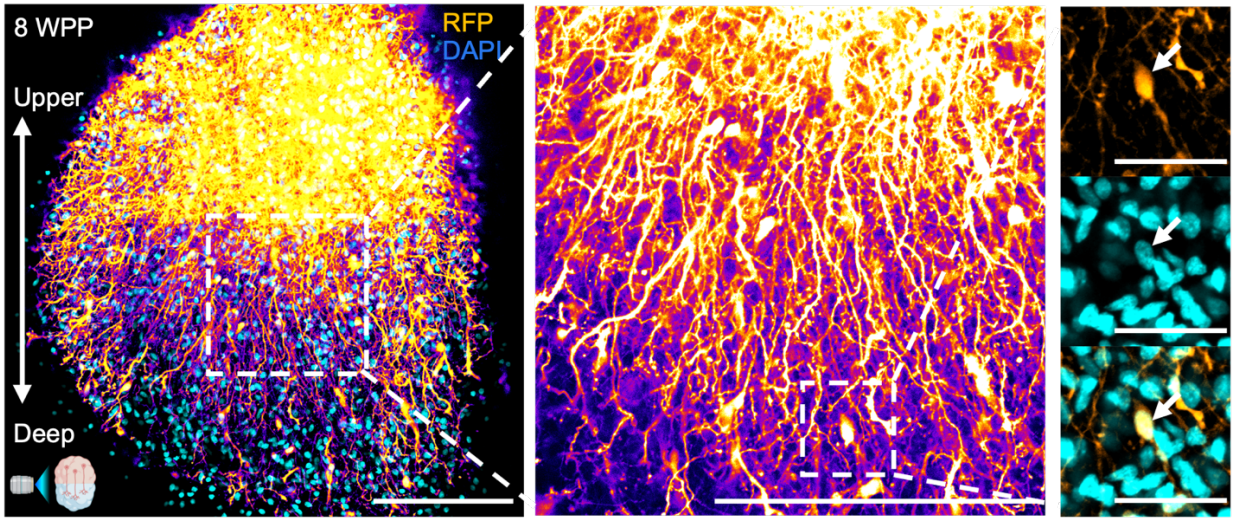

Figure 4.9 Two-layer cortical tissue with 8 WPP incubation.

A reconstructed confocal z-projection image (left) and the magnified image (middle and right) exhibiting cross-layer process outgrowth and neuronal migration in droplet-printed two-layer tissue at 8 WPP. Neurons were visualized by RFP (false-colored as fire) expression in UNs and DAPI cell nucleus staining in both UNs and DNs. The arrow indicates a migrating UN. Scale bars: left and middle, 500 μm; right, 50 μm.

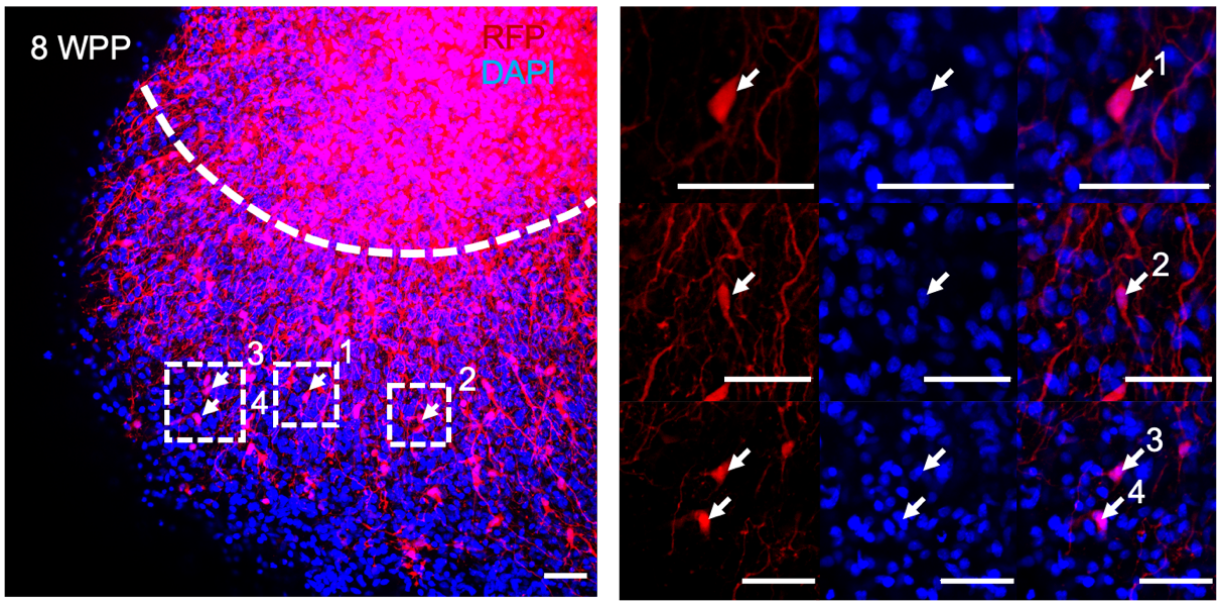

Figure 4.10 Neuron migration in two-layer cortical tissue with 8 WPP incubation. Reconstructed confocal z-projection image (left) and high magnification images (right) exhibiting cross-layer neuron migration in printed two-layer tissue at 8 WPP, visualized by RFP expression in UNs and DAPI nuclear staining in both UNs and DNs. Dashed boxes indicate magnified regions. Arrows and numbers indicate migrating neurons. Scale bar: 50 μm.

Process outgrowth and neuron migration are two different cellular behaviors that can be determined separately. A magnified view of two-layered cortical tissue showed that the UNs had produced processes projecting toward the deep layer (Figure 4.9). To identify individual neuron migration between layers in printed tissues. We further magnified the view and found migrating UNs into the deep-layer region, as indicated by the arrows in Figure 4.9 and Figure 4.10. The identity of UNs was confirmed by the colocalization of the RFP-expressing cell body and the general cell nucleus staining DAPI.

Neurodevelopment is a continuous process. Therefore, it is critical to investigate the dynamic changes in cross-layer process outgrowth and neuron migration over the incubation period. We applied two indicators to quantitatively evaluate the outgrowth and migration processes. First, we

evaluated the area of the RFP-labeled UNs in the unlabeled deep-layer region. Comparisons of the sectioned two-layer cerebral cortical tissues at 2, 4, and 8 WPP illustrated the dynamics of cross-layer process outgrowth and neuron migration (Figure 4.11). Quantitative analysis revealed significantly increased migration of RFP-labeled UNs into the deep layer during the 8-week incubation period, but no significant change in the RFP signal was identified in the upper layer (Figure 4.12 and Figure 4.13). Subsequently, we used the number of neurons migrating from the upper layer to the deep-layer region as our second indicator. The number of migrating UNs was counted as RFP-labeled cells per field (0.1 mm^2) in the deep-layer region. Sectioned two-layer cerebral cortical tissues at 2, 4, and 8 WPP illustrated a significant increase in RFP-labeled migrating UNs over the period. UN identity was confirmed by the colocalization of RFP-labeled cell bodies with DAPI staining.

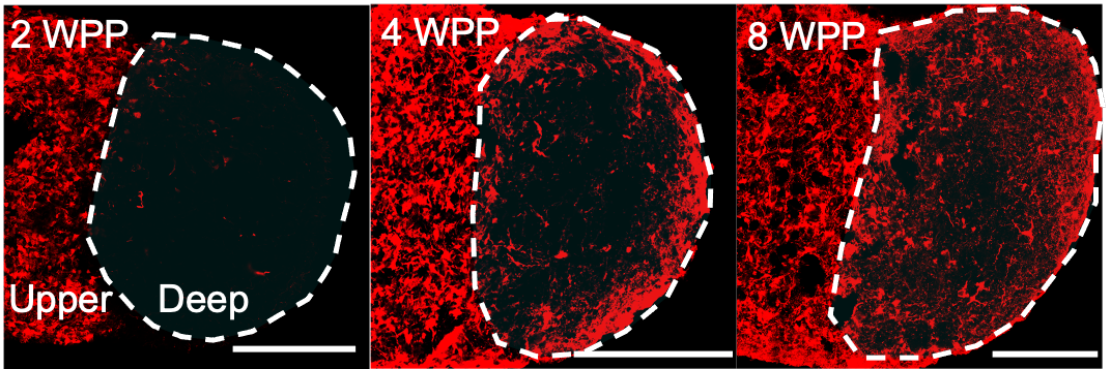

Figure 4.11 Process outgrowth and neuron migration in the sectioned two-layer cortical tissues.

Fluorescence images of cortical tissue sections with cross-layer process outgrowth and cell migration at 2 (left), 4 (middle) and 8 (right) WPP. Dashed circles indicate the deep-layer segment with invading RFP-labeled UNs. Scale bars: 200 μm.

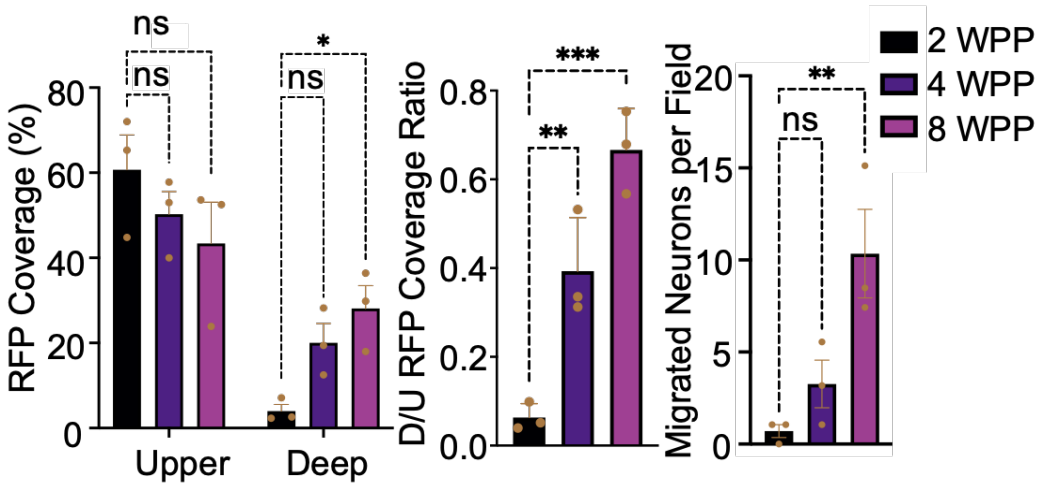

Figure 4.12 Quantitative analysis of process outgrowth and neuron migration in two-layer cortical tissues.

Quantitative analysis of process outgrowth by RFP coverage (left and middle), and neuron migration by cell body counting (right), as shown in Figure 4.11 (n = 3, one-way ANOVA test). Field size: 0.1 mm^2.

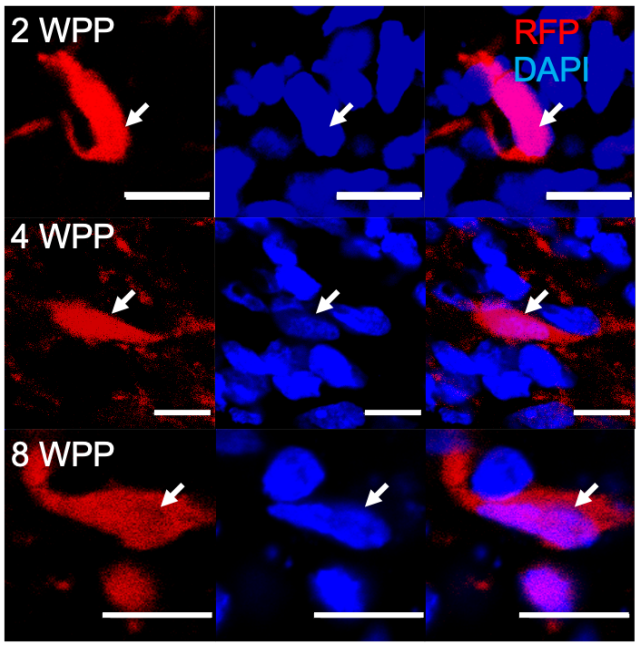

Figure 4.13 Examples of migrating RFP-labelled UNs.

Confocal images of 30 μm-thickness sections of 2, 4, and 8 WPP two-layer tissues showing cross-layer neuron migration, visualized by RFP and DAPI colocalization. Scale bar: 10 μm.

4.5.3. Spatiotemporal Biomarker Expression

Biomarker expression patterns in printed two-layer cerebral cortical tissues play an important role in reflecting dynamic self-regulation. We determined the spatial-temporal expression of both general and layer-specific neural biomarkers to reveal neuronal maturation during post-printing incubation (Figure 4.14). Figure 4.15 and Figure 4.16 show examples of magnified views of sectioned and stained cerebral cortical tissues.

Immunostaining of sectioned cortical tissues at the three time points (2, 4, & 8 WPP) demonstrated a significantly higher population of neurons in the upper layer compared to the deep layer, which expressed the upper-layer marker CUX1 (78 ± 2% vs. 37 ± 3%, mean value over 2, 4, & 8 WPP) and the middle-upper layer marker SATB2 (68 ± 4% vs. 39 ± 4%). By contrast, a higher proportion of neurons in the deep layer compared to the upper layer expressed the deep-layer marker CTIP2 (35 ± 4% vs. 10 ± 2%) at 2 WPP. The ratio of cells expressing CTIP2 in the deep and upper layers decreased to 18 ± 5% and 5 ± 0.2%, respectively, at 4 WPP and subsequently dropped at 8 WPP (4 ± 2% and 3 ± 0.6%, respectively). Quantification and statistic analysis were described in the Method Section (Chapter 7.6.4. and 7.8.). This result is comparable with a former study in cerebral organoids where the proportion of cells expressing CTIP2 dropped from 30 to 105 days in incubation following an initial lift during the first 4 weeks, thus resembling the temporal patterning determined in the mouse[121]. Furthermore, a high population of cells (over 90%) showed a positive expression of neuronal marker TUJ1 at 2, 4, and 8 WPP in both layers, demonstrating that most cells in the printed two-layer tissues had committed to the neuronal lineage (Figure 4.14 and Figure 4.17). Together, these results confirmed that the droplet printed two-layer tissues maintained the designed cellular architecture, with dynamic self-regulation-like processes of outgrowth and cell migration. Furthermore, we observed the expected layer-specific marker expression during the eight-week maturation process.

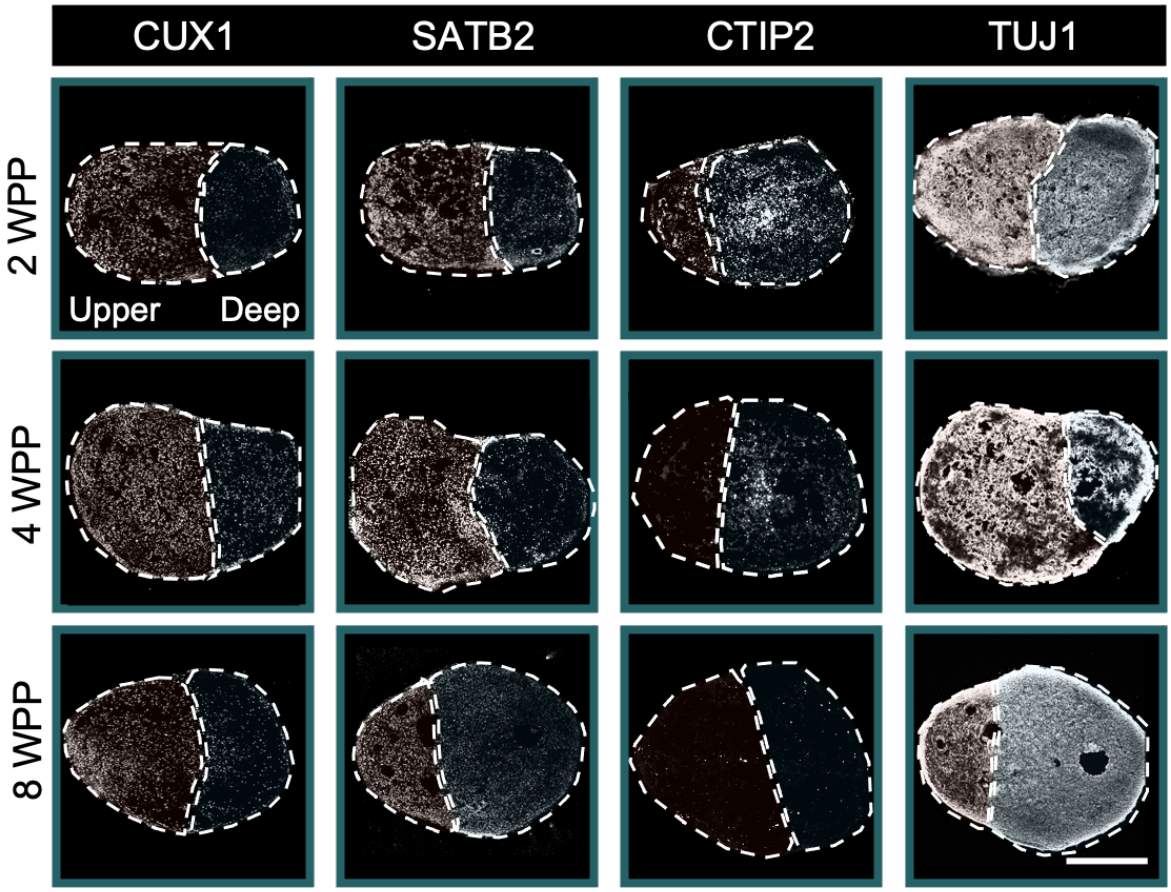

Figure 4.14 Spatiotemporal marker expression assessment in two-layer cerebral cortical tissues.

Spatiotemporal immunofluorescence analysis of general neural (TUJ1) and layer-specific marker (CUX1, SATB2 and CTIP2) expression in sectioned two-layer cortical tissues. Dashed line outlines the layers. Scale bars: 500 μm.

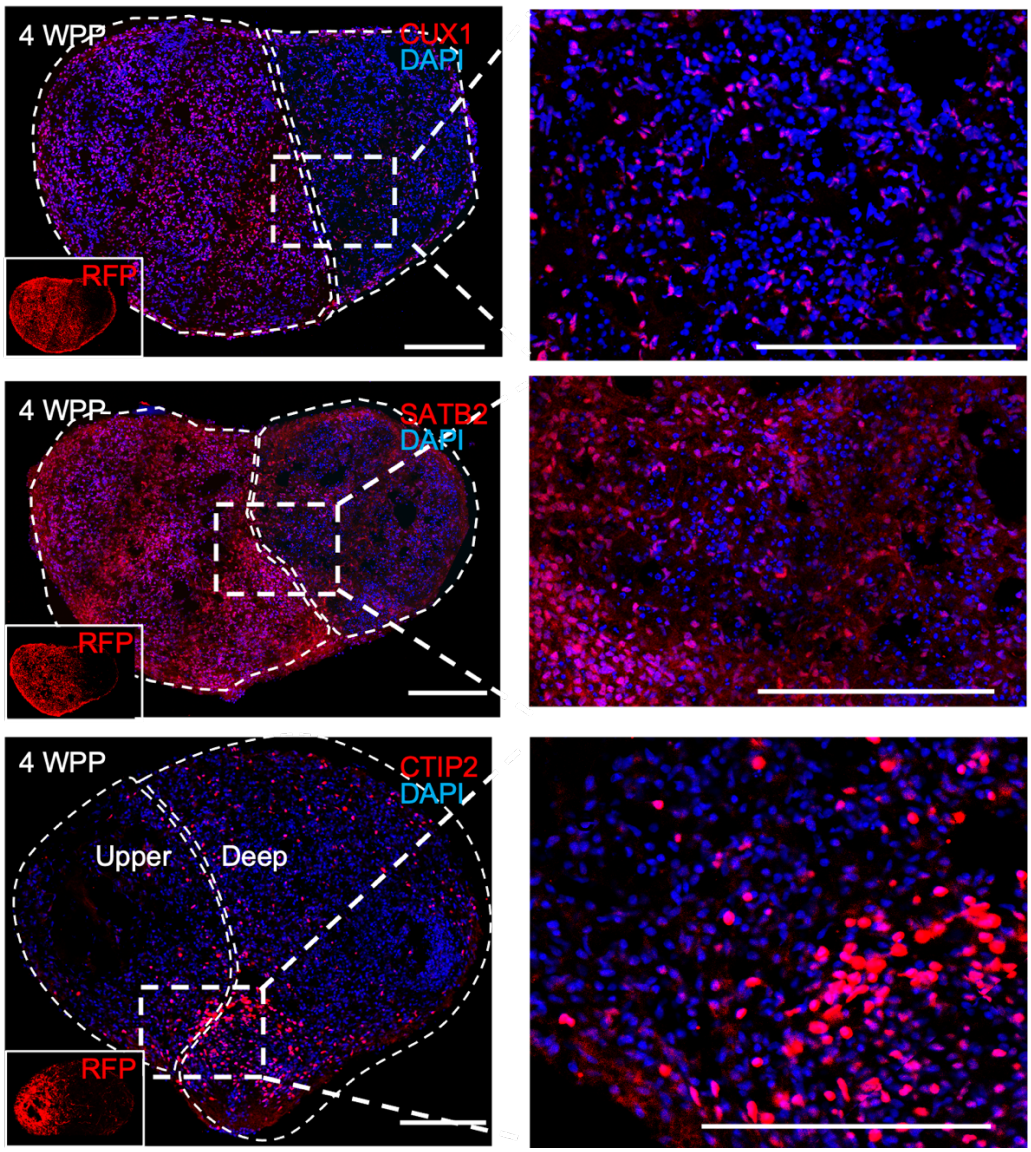

Figure 4.15 Magnified examples of marker expression assessment for two-layer cortical tissues.

Immunofluorescence images of sectioned two-layer tissues at 4 WPP showing the expression of layer-specific markers (CUX1, SATB2 and CTIP2). The bottom left small images show the RFP expression of the tissue. Dashed lines outline the layers, and dashed boxes indicate the magnified areas. Scale bar: 200 μm.

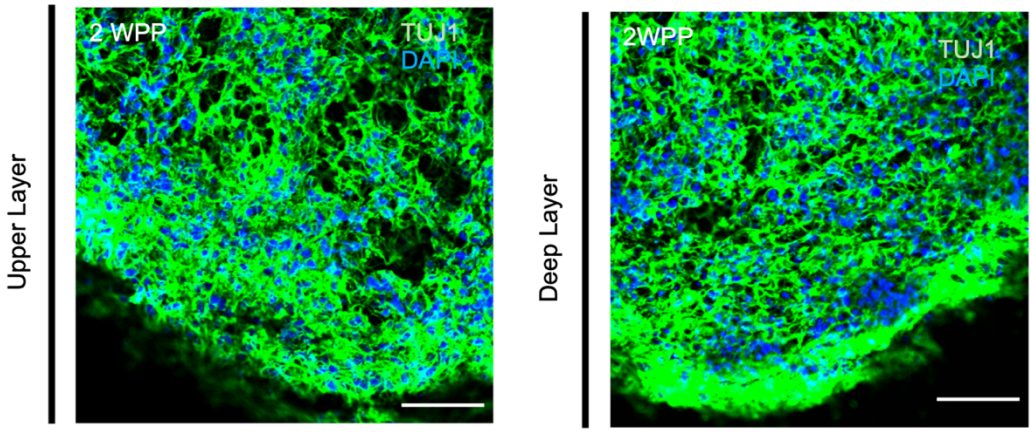

Figure 4.16 Magnified images of two-layer cortical tissues showing neuronal marker TUJ1. Confocal images of sectioned two-layer tissues showing the expression of the young neuronal marker TUJ1. Scale bar: 50 μm.

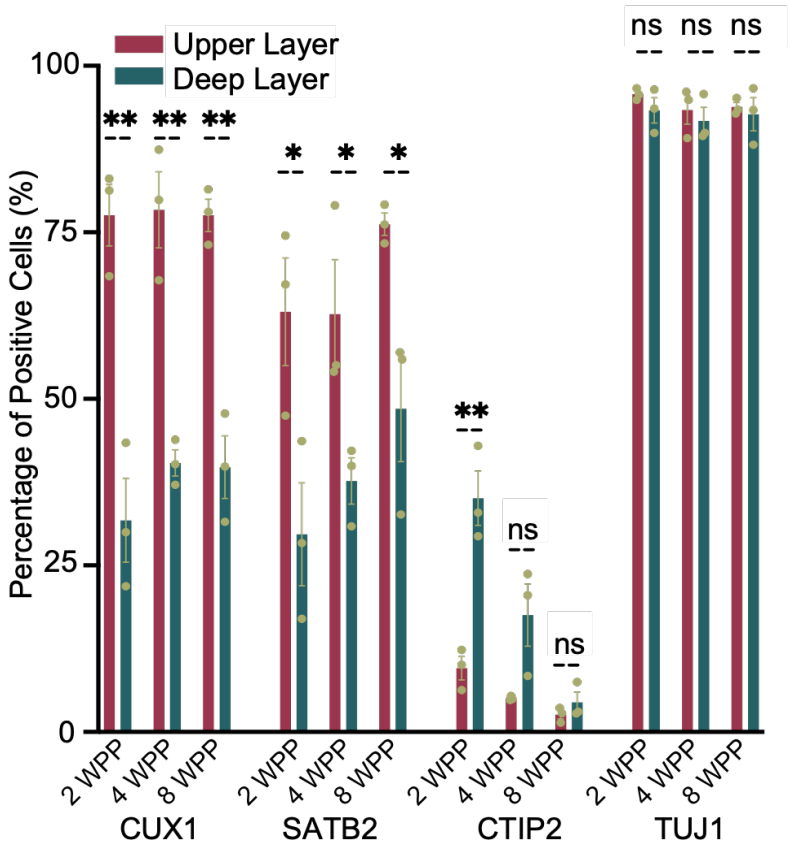

Figure 4.17 Quantitative analysis of marker expression in two-layer cortical tissue. Quantitative analysis of marker expression in the upper and deep layers of cortical tissues in Figure 4.14 (n = 3; unpaired student t-test). ns = not significant; *, $P < 0.05$; **, $P < 0.01$; ***, $P < 0.001$.

4.6. Chapter Conclusion

It is a considerable challenge to engineer human tissue with diverse cell types and desired cellular architectures and functions. In this chapter, we used a droplet printing technique to pattern single deep-, single upper-, and two-layer cerebral cortical tissues. The cortical tissues were fabricated by bioink containing hiPSC differentiated DNPs or/and UNPs. The self-regulation of DNPs and UNPs in two-layer patterned tissues was investigated at different culture times (2, 4, and 8 WPP). The identity and architecture of the deep and upper layers were maintained during *in vitro* culture after printing. During this period, cellular self-regulation behaviors, such as maturation, process outgrowth and neuron migration, were also observed. This strategy allowed us to avoid the difficulties related to handling mature neurons, which are known to be sensitive to dissociation from a 2D culture environment and very possibly damage in the 3D printing process because of their sensitivity to physical stress, fluctuation in temperature, and modification in osmolarity[122].

Notably, after printing, the DNPs and UNPs continued to mature toward DNs and UNs, respectively, even though they were in a common growth medium. The application of lineage-committed progenitors represents a novel method for the fabrication of 3D tissues. Recently, the Lewis group reported a codifferentiating method in 3D tissues differentiated from two kinds of hiPSCs, transfected with either endothelial- or neural-associated transcription factors, to produce vascularized 3D neural tissues[123]. Although the report produced patterned neural tissues composed of different cell types, it relies on lentivirus-based genetic engineering, which might limit its potential application in implantation therapies[124,125]. In our strategy, the generation of 3D neural tissues composed of different types of neurons without genetic modification reduces concerns over clinical safety and might be used to construct other tissues containing multiple cell types.

Chapter 5. Printed Cortical Tissue Implanted in Brain Explant

5.1. Chapter Introduction

Organotypic brain explant culture can preserve brain architecture and cellular function in an *ex vivo* environment[126,127]. Therefore, many neuroscience research studies, including modeling the neural development process[127], neural degenerative disease[128], brain repair[129], and malignant brain tumors[130], have applied organotypical brain slices. In the current study, we leverage the advantage of organotypic brain explant culture and investigate the repairing effect of droplet-printed cortical tissues. To do so, we implanted one- or two-layer printed cerebral cortical tissues into the lesions in the cortex of mouse brain explants. To evaluate the effects of nutrients and chemicals on the integration between implant and brain, implanted explants were cultured under two different culture media with or without a treatment of small molecule DAPT. Cellular and tissue regulations, such as process outgrowth and neuron migration from the implants into the host, were measured. We also investigated the neuronal activity in the implant and brain explant, and their potential implant-explant functional connection across their boundary, primarily through the Ca^{2+} oscillations in cells.

5.2. Acknowledgments

All work included in this chapter was performed by the author, unless specifically stated in the text. I acknowledge that the preliminary effort of cortical tissue implantation work was completed with the assistance of Dr. Luna Campos Soares and Sara Bandiera in A/Prof. Francis Szele's Group and Prof. Zoltan Molnar's Group (Department of Physiology, Anatomy & Genetics, University Oxford). Mice scarifications were completed by A/Prof. Ming Lei and Dr. Tianyi Sun (Department of Pharmacology, University of Oxford). P8 C57BL/6J mice were sacrificed by cervical dislocation in accordance with the Animals Scientific Procedures Act (1986) under license no. PP8557407.

5.3. Establishment of Printed Tissue Implanted Brain Explant

5.3.1. Model Establishment

Directly implanting cortical tissue into a mouse brain requires complicated animal ethical approval, a licensed operator for surgery, and long-term optimization for the procedure. Here, we focus on an *ex vivo* system that can resemble brain architecture and cellular function.

Our first attempt involved the section and culture of organotypic brain slices. A preliminary experiment applied the vibratome to section agarose-embedded brain into 200 μm slices and cultured in the NMM supplemented with 10% horse serum. However, despite several rounds of experiments, most of the brain slices did not survive until the next day. Our later work improved the brain slice section method and optimized the culture medium. Instead of using vibratome, we used compresstome to section the brain. To do so, mouse brains were harvested and kept in ice-cold carbogen-saturated (95% O_2/ 5% CO_2) Earle's balanced salt solution (EBSS). Coronal slices (300 μm) were obtained by sectioning them with a compresstome. The brain slices were then

cultured on 0.4-μm Millicell-culture inserts. In terms of culture medium, we optimized two different culture mediums, condition A and condition B, with an increased percentage of horse serum from 10% to 25%, comparable with the published organotypic brain slice protocols[128]. Condition A was a culture medium with a nutrient-enriched formula modified from DMEM/F12 and Neurobasal medium composed of a high glucose level (~25 mM)[131], while condition B was a culture medium primarily containing the commercially available BrainPhys medium with a physiological glucose level (~2.5 mM). The high glucose level was reported previously to interfere with neuron differentiation through oxidative and endoplasmic reticulum stress[132]. Former studies have indicated the superior performance of BrainPhys medium compared to the mixture of DMEM/F12 and Neurobasal medium on the 2D culture of hiPSC-differentiated neurons in two aspects, neuronal survival and function, illustrated by improved frequent action potential firing and long-term electrical activity[131]. Both culture mediums enabled the survival of the brain slices. Table 5.1 presents the formula in detail.

Table 5.1 Formula of Brain Explant Culture Condition A and B

Brain Explant Culture Medium Condition A 100mL					
Item	**volume**	**Final Conc**	**Stock Conc**	**Supplier**	**Cat no**
DMEM/F12 Medium	~36 mL	NA	1X	Life Technologies	21331020
Neurobasal Medium	~36 mL	NA	1X	Life Technologies	21103-049
B27 supplement	1 mL	NA	NA	Life Technologies	17504044
N2 supplement	0.5 mL	NA	NA	Life Technologies	17502-048
GlutaMax	1 mL	NA	100X	Life Technologies	35050-038
Pen/Strep	1 mL	NA	10,000 U/mL	Gibco	15140122
Horse Serum	25 mL	NA	NA	Life Technologies	16050130
Brain Explant Medium Condition B 100mL					
Item	**volume**	**Final Conc**	**Stock Conc**	**Supplier**	**Cat no**
Brainphys Neural Medium	72.5 mL	NA	NA	Stemcell Technologies	5792
SM1 supplement	1.5 mL	NA	NA	Stemcell Technologies	5792
Pen/Strep	1 mL	NA	10,000 U/mL	Gibco	15140122
Horse Serum	25 mL	NA	NA	Life Technologies	16050130

To implant the printed tissues into a brain explant and assess their integration, we printed the cerebral cortical tissues 1 day before the mouse brain slices were acquired. On the same day, a biopsy punch with 800-μm outer diameter was used to punch a lesion in the cortex of the

explant. The 800-μm circle spanned most of the thickness of the P7 mouse cortex (~800–1000 μm)[133]. The printed cortical tissue was then implanted into the lesion in a natural orientation (upper layer out). The implanted explants were maintained in culture medium under either culture medium condition A or condition B at 37°C under 5% CO_2. On day 2, DAPT was added directly to the cultures without a medium change to generate a final concentration of 10 nM. Culture medium was then changed every 3 days. Most implanted brain explants were harvested, fixed, and immunostained for assessment at 3- or 5-days post implantation (DPIs). Figure 5.1 shows the overall process.

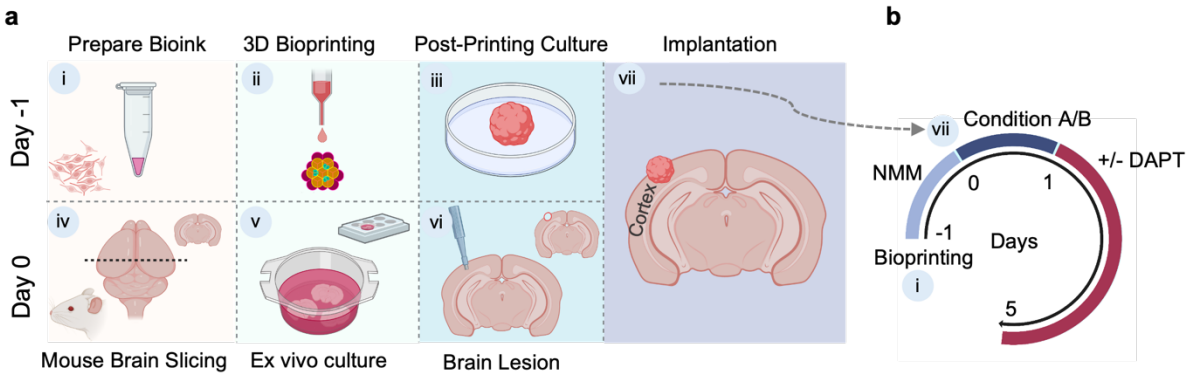

Figure 5.1 Schematic of implanting printed cortical tissue into brain explant.

a. Steps in the implantation process. Step i: Bioink made from a mixture of DNPs and/or UNPs and Matrigel. Step ii: Droplet-based bioprinting of cerebral cortical tissue. Step iii: Post-printing incubation of the fabricated tissue for one day. Step iv: Section 300 µm-thick mouse brain slices. Step v: Brain slices (explants) were maintained under condition A/B medium before implantation. Step vi: Create a brain lesion through an 800 µm biopsy punch. Step vii: Implant fabricated tissue into the lesion of brain explant, which was subsequently incubated. **b.** Culture of implanted explant and compound treatment. Brain explants were cultured under either condition A or B for one day, followed by treatment with or without compound DAPT for another four days.

5.3.2. Survival Study

Before further characterization, we assessed the survival of the brain explants and implanted printed tissues. Implanted brain explants at 5 DPIs were incubated with 2.5 µM calcein-AM and 5.0 µM propidium iodide (PI) for 30 min before imaging. Calcein AM is a cell-permeant dye that can measure cell viability in most eukaryotic cells. In live cells, the nonfluorescent calcein AM is converted into a green-fluorescent calcein after acetoxymethyl ester hydrolysis by intracellular esterases[134]. PI is a red-fluorescent nuclear and chromosome counterstain; it is not permeant to live cells and is commonly used to detect dead cells[135].

To quantitatively analyze viability, three randomly selected cortical regions of the explants were imaged. Images were processed in ImageJ and counted manually. Live/dead staining showed that

the cell population in the brain explants was 86 ± 3% viable at 5 DPIs (Figure 5.2a,b). The viability of the implants was similar, as indicated by their RFP expression (Figure 5.4a) in the next section.

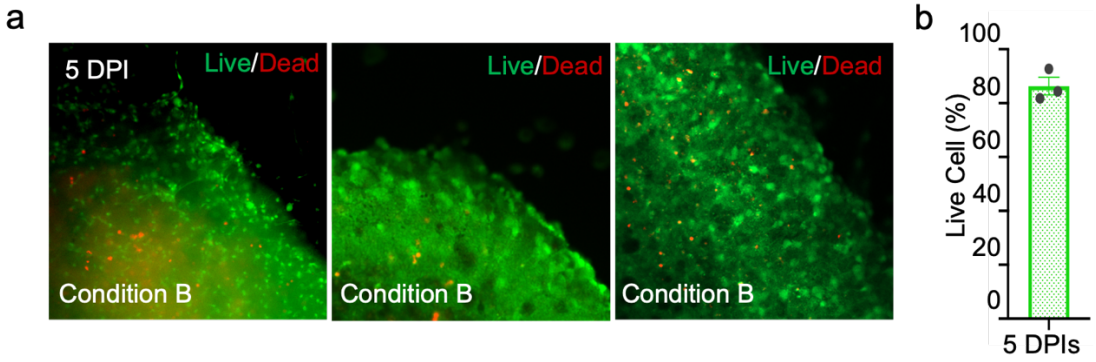

Figure 5.2 Brain explant live/dead assay.

a. Fluorescence images of a live/dead assay of deep-layer cerebral cortical tissue implanted explant cultured under condition B at 5 DPIs. **b.** Quantitative live/dead analysis of host cells of 5 DPIs at condition B (n = 3).

5.4. Fundamental Characterization

5.4.1. Simplified TBI Model

To investigate the potential of droplet-printed tissue to repair damaged brain, we established a simplified TBI model by creating lesions on brain explants. The lesioned explants were then implanted with printed cortical tissue. Figure 5.3 shows two examples of printed tissue-implanted in brain explants under a bright-field microscope. The integration between the implanted cortical tissue and the brain explants was determined using several characterization methods.

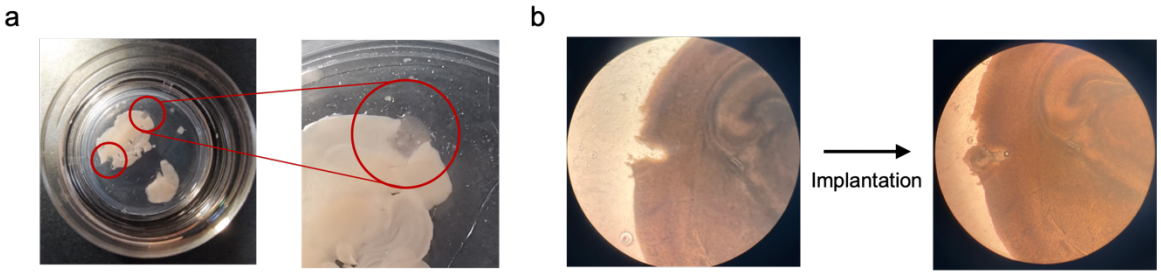

Figure 5.3 Examples of 0 DPI printed tissue implanted brain explants.

a. Left: Brain explant with a lesion in the left cerebral hemisphere and implanted with printed deep-layer tissue in the right cerebral hemisphere at 0 DPI. Right: A magnified image of a lesion in the right hemisphere, which is implanted with cortical tissue. **b.** A bright-field image of a brain explant with a lesion implanted with printed deep-layer cortical tissue at 0 DPI.

Process outgrowth and neuron migration from the implant to the host brain were measured as important indicators of integration. The implanted brain explants at 3 DPIs were harvested. At the edge of the implanted printed tissue, we found RFP-labeled neurons generated process outgrowth and neuron migration, crossing boundary, toward the host, indicating that the printed tissues had integrated into the brain explant (Condition B, no DAPT; Figure 5.4a).

By analyzing a living brain explant with confocal scanning, the RFP-labeled neurons revealed a dynamic process outgrowth and neuron migration from 1 to 5 DPIs (Figure 5.4b). To quantitatively determine the distance between process outgrowth and neuron migration, we applied a profile plots method of fluorescent intensity in ImageJ, a widely used open-source Java-based image processing program. The fluorescence intensities were plotted with "profile plots," and the width of the decreasing phase of gray value was used to represent the outgrowth distance. By applying this method, we determined the extent of process outgrowth at 1 DPI (220 μm) and 5 DPIs (405 μm; Figure 5.4c). The same method was applied to perform a later analysis.

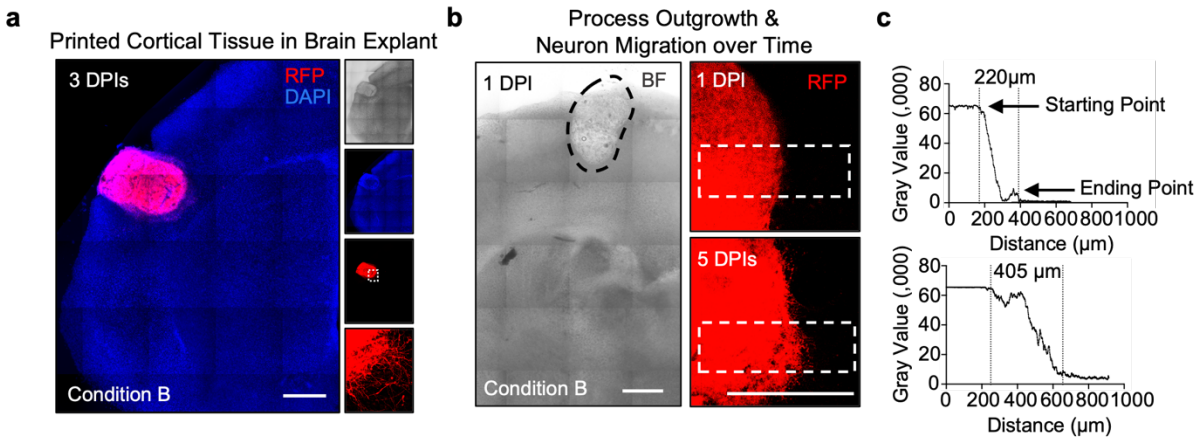

Figure 5.4 Printed cortical tissue implanted brain explants.

a. Left: A tiled fluorescence confocal image of a 3-DPI implanted brain explant cultured under condition B. The implant is composed of RFP-labeled DNs. Right: Bright field (top), DAPI nucleus staining (upper middle), RFP-labeled implanted tissue (lower middle), and its higher magnification view (bottom). Culture condition B is described in the Methods section. **b.** Confocal image of a 1-DPI cortical tissue implanted brain explant (left) and confocal live images of process outgrowth and neuron migration from an implanted brain explant at 1 DPI (top right) and 5 DPIs (bottom right). **c.** Profile plots for fluorescence intensity along the white dashed boxes from left to right, as referred to "b." The vertical black dashed lines represent the margins of RFP fluorescence.

5.4.2. Implanted Explant Response to Nutrients and Molecule

Process outgrowth and neuron migration are regulated by microenvironmental cues during neurogenesis[136,137]. Hence, we hypothesized that process outgrowth and cell migration could respond to distinct nutrient conditions and treatment of small molecules, such as DAPT. Gamma-secretase inhibitor, DAPT, blocks the presenilin–γ-secretase complex [94] and prevents the downstream activation of Notch[95]. DAPT has been applied in various hiPSC differentiation protocols to facilitate neuron differentiation and maturation[55,96,97]. We incubated implanted explants with four conditions: condition A and condition B, with and without DAPT. By applying fluorescent confocal scanning, we exhibited differences in the distance of outgrowth and

migration with the four conditions at 5 DPIs (Figure 5.5a). Subsequent quantitative analysis revealed a significant increase in the distance of process outgrowth in condition B (434 ± 41 μm) compared to condition A (265 ± 30 μm). The DAPT treatment resulted in a considerably increase in distance for both condition A (increased by 153 μm to 418 ± 70 μm) and condition B (increased by 287 μm to 721 ± 71 μm; Figure 5.5b). Hence, our results demonstrated that implanted brain explants are capable of evaluating the effect of nutrients and molecule treatment on implantation.

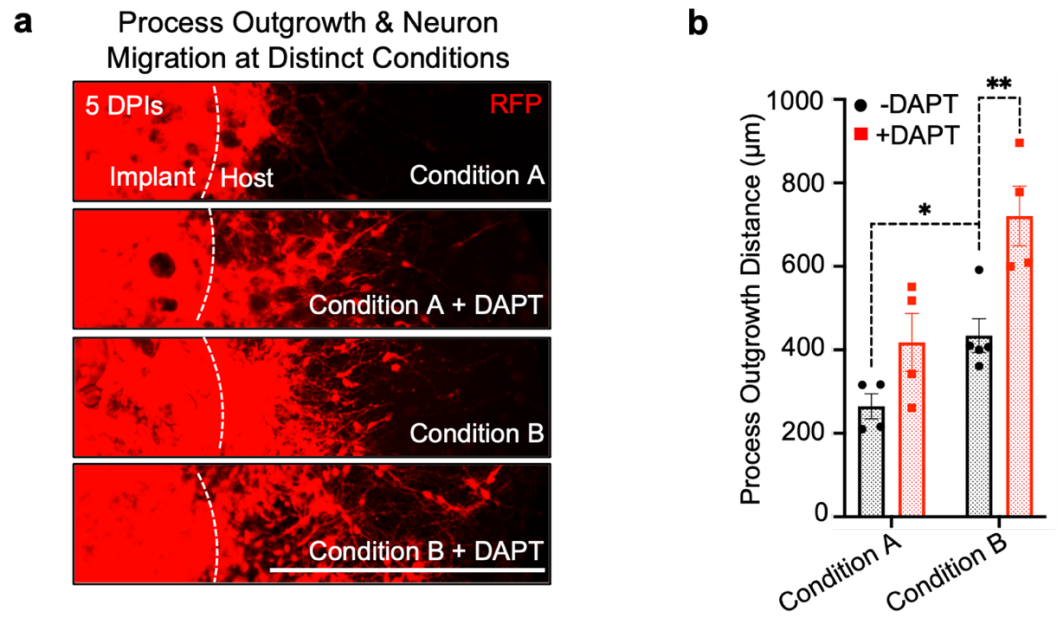

Figure 5.5 Printed cortical tissue implanted brain explant with four different conditions. **a.** Confocal images of 5-DPI implanted brain explants showing implant-to-host process outgrowth and neuron migration. The implanted brain explants were incubated under condition A/B with or without DAPT. Dashed lines demonstrate the original borders of the implants. **b.** Quantitative analysis of process outgrowth and neuronal migration is revealed in "f". ($n \geq 4$; unpaired student t-tests). ns = not significant; *, $P < 0.05$; **, $P < 0.01$. Scale bars: 500 μm.

5.4.3. Implanted Explant Response to Pre-implantation Culture

The former experience of culturing printed cerebral cortical tissues implies that freshly printed tissues gradually transform from a soft to a compact texture over the initial two weeks. Therefore,

it is worth investigating whether the pre-implantation culture of printed cortical tissues affects the integration between implants and brain explants. We thus compared the distance of process outgrowth and neuron migration from the implants with a 1- or 14-day pre-implantation incubation period in condition B. The outcome revealed that a 14-day pre-implantation culture of cortical tissues can extend implant-to-host process outgrowth (Figure 5.6h). We found an increase in process outgrowth of 222 μm to 656 ± 63 μm at 5 DPIs compared with the implants that had undergone a 14-day pre-implantation incubation (Figure 5.6b,c).

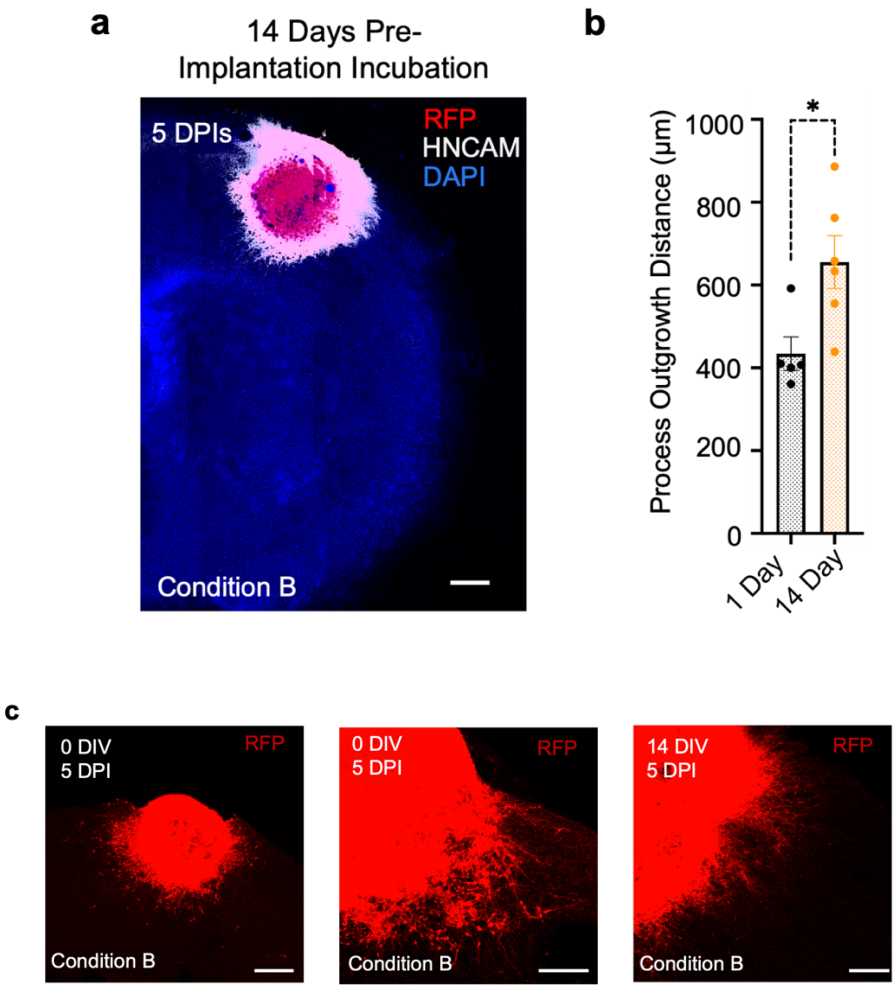

Figure 5.6 Pre-implantation culture for cortical tissue implanted brain explants.

a. A tiled confocal image of a representative brain explant implanted with deep-layer cortical tissue that had been cultured for 14 days before implantation. The implanted explant was immunostained with human-specific neural marker (HNCAM). RFP fluorescence reveals process outgrowth and neuron migration from the implant. **b.** Quantitative analysis of process outgrowth and neuron migration from cortical tissue with 1 day or 14 days pre-implantation incubation ($n \geq 4$; unpaired student t test). **c.** Additional examples of implanted RFP-labeled deep-layer cortical tissues under different culture conditions and pre-implantation incubation periods.

5.4.4. Implanted Explant Demonstrates Individual Migrating Neuron

We also investigated neuron migration, an important neurogenesis phenomenon. Under high magnification, we identified individual neurons migrating across the implant–host boundary (Figure 5.7 a). To determine that they are not debris of the outgrowing process, we colocalized them with cellular nucleus stain DAPI. Neurons demonstrating both a complete cell body and colocalized DAPI staining were counted as migrating neurons. Quantitative analysis was performed by quantifying the number of RFP-labeled neurons in an area between 200 and 400 μm away from the implant. The measures showed that 20 ± 2, 17 ± 3, and 18 ± 3 RFP-labelled neurons/0.1 mm^2 migrated into the host brain explant at 5 DPIs from implants composed of UNs, DNs, and 14 days pre-cultured DNs, respectively (Figure 5.7 b).. The migration of UNs was determined over three time points: 1, 3, and 5 DPIs (1.4 ± 0.4, 12 ± 4, 20 ± 2 neurons/0.1 mm^2 respectively).

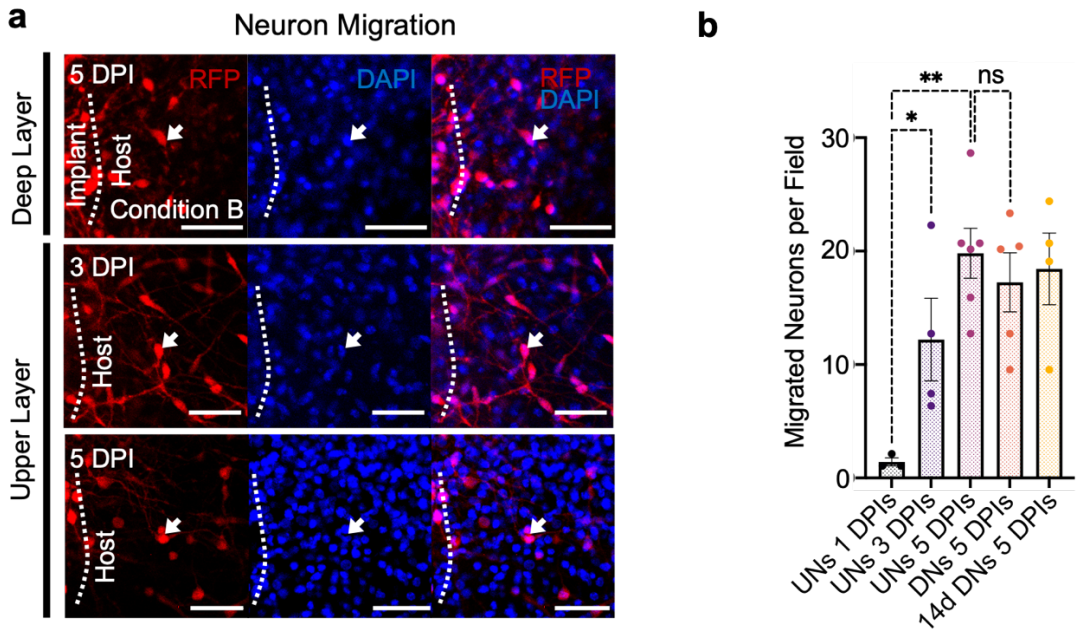

Figure 5.7 Individual neuron migration in cortical tissue implanted brain explants.
a. Representative confocal images of a 5-DPI implanted explant with DNs (top), and implanted explants with UNs at 3 DPIs (middle) and 5 DPIs (bottom), showing the migrating RFP-positive neurons from implants into the brain explants. The arrow shows a migrating human neuron. Scale bar: 50 μm. **b.** Quantitative analysis of neuron migration from implants into host brain explants ($n \geq 3$; one-way ANOVA). Field size: 0.1 mm^2. For "b": ns = not significant; *, $P < 0.05$; **, $P < 0.01$.

5.4.5. Implanted Two-layer Cortical Tissue in Brain Explant

Effective therapy using stem cell-derived cortical tissue for brain repair has not been established. One of the critical difficulties is forming a tissue resembling the brain tissue anatomy. Therefore, we printed cortical tissues with a height comparable to brain explants of the cerebral cortex of P8 mice (approximately 800–1,000 μm) [133] and a simplified laminar structure composed of deep and upper layers. The printed two-layer cortical tissue was then implanted into the lesioned cortex of a mouse brain explant. In particular, the orientation of the implanted brain tissues matched the cortex of the host brain, as the deep layer of the implant was implanted into the ventral area of the

cortex and the upper layer into the dorsal area. Process outgrowth and neuron migration from the implant, crossing the boundary, to the host brain was measured to determine the extent of integration between the implants and host (Figure 5.8a,c and Figure 5.9).

Neural cell adhesion molecule (NCAM) is a cell surface protein that participates in adhesion and neurite outgrowth during nervous system development[138]. Human NCAM (HNCAM), which is only expressed in human cells, was therefore used to distinguish human-originated implants from mouse brain explants. Quantitative analysis of process outgrowth and neuron migration was performed by measuring the longest distance from the implant to the host brain with detectable HNCAM expression. Two-layer cortical tissues implanted brain explants at 1, 3, and 5 DPIs revealed a rise in the process projection distance over the incubation periods: 85 ± 14 μm, 336 ± 22 μm, 419 ± 22 μm, respectively (Figure 5.8b). In addition, immunostaining exhibited human-specific biomarker HNCAM expression in both layers, evidencing the human origin of the implanted neurons. The expression of RFP was considerably lower in the deep layer compared to the upper layer, showing that the two-layer pattern remained in the implant (Figure 5.8d,e).

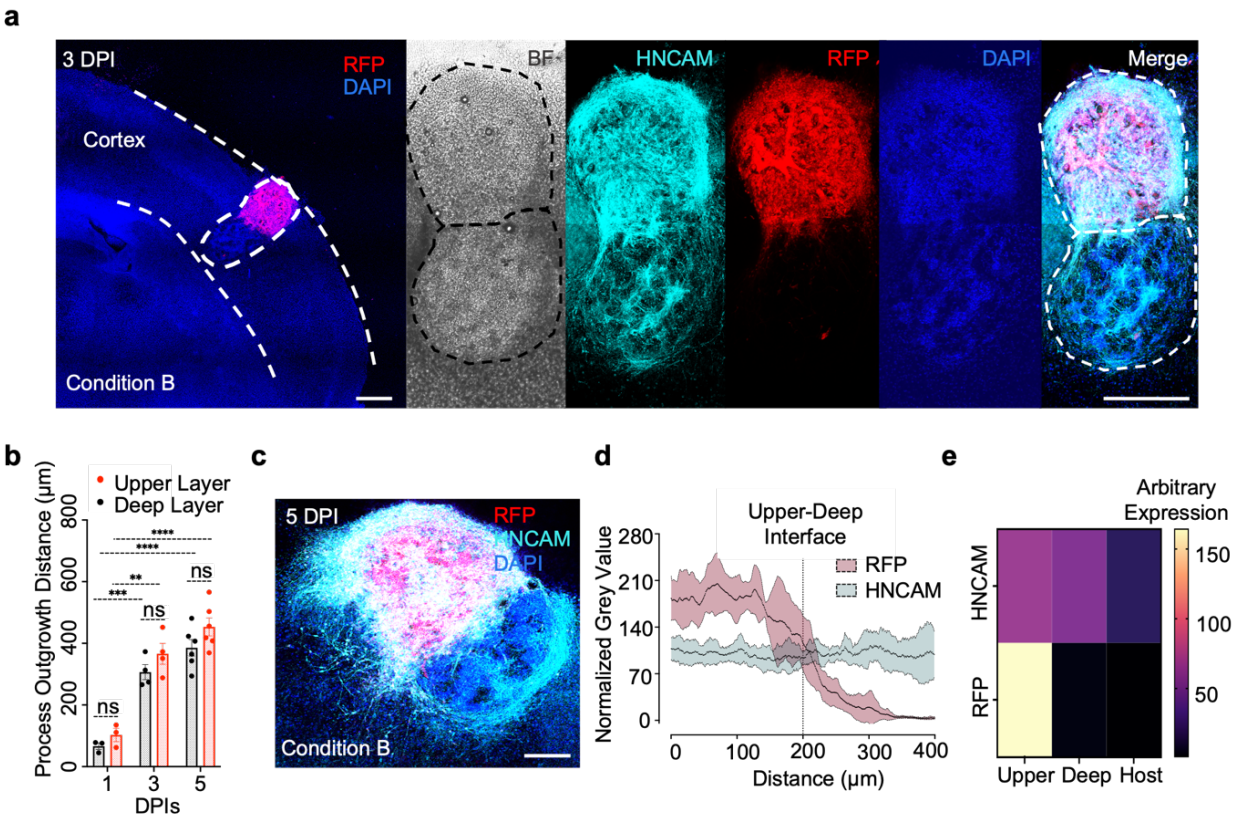

Figure 5.8 Two-layer cortical tissue integration with the host explant.

a. Tiled fluorescence confocal image of a 3-DPI implanted brain explant. Dashed lines show the cerebral cortex of the mouse and the implanted two-layer tissue. The human-specific marker HNCAM labels both layers of the implant. RFP labels only the upper layer. **b.** Quantitative analysis of process outgrowth and neuron migration from the two-layer implant into the host brain at 1, 3 and 5 DPIs ($n \geq 3$; ns = not significant; ***, $P < 0.001$; ****, $P < 0.0001$; unpaired student t tests). **c.** A tiled confocal image of a 5-DPI two-layer implanted tissue. **d.** Fluorescence-intensity profiles demonstrating HNCAM expression in both upper and deep layers of implant, whereas RFP expression decreased in the deep layer ($n \geq 3$) **e.** Heatmap exhibiting the marker expression by gray value in the 5-DPI upper and deep layers of an implant and in the host ($n \geq 3$).

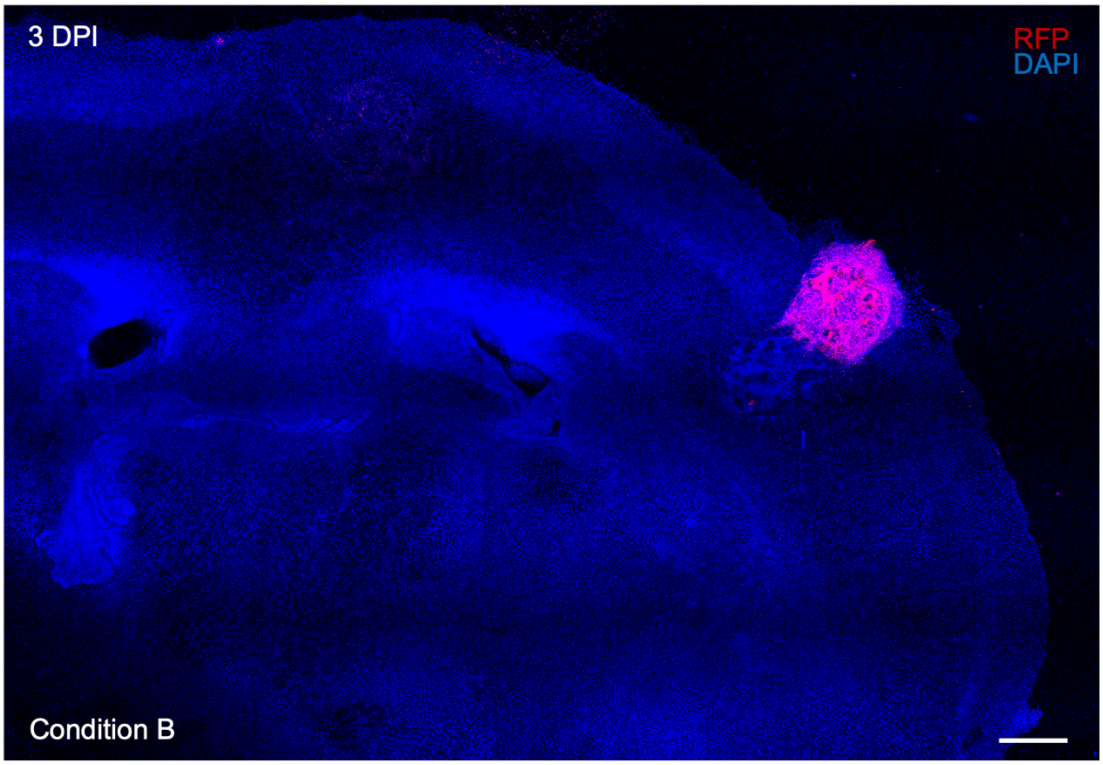

Figure 5.9 Tiled fluorescence confocal image of an explant implanted with a two-layer printed tissue, as shown in Figure 5.8a.

Cells were visualized with RFP (UNs) and DAPI nuclear staining in UNs, DNs, and the host. Scale bar: 200 μm.

5.5. Functional Characterization

5.5.1. Fundamental Functional Analysis

Functional connections between the implant and host brain serve as one of the challenges to establishing an effective regenerative therapy for repairing injured brain and restoring lost behaviors. In the nervous system, action potential is a basic neural activity triggered by ion channels and ion movement, leading to a rapid sequence of changes in voltage across a cellular membrane. When the action potential reaches the end of an axon, it triggers the release of neurotransmitters at the presynaptic nerve terminals, passing neural activity to the next neuron. During this process, voltage-gated calcium channels primarily mediated the influx of Ca^{2+}, leading to the subsequent release of neurotransmitters[139,140]. Fluorescent dye detects Ca^{2+}

oscillations, representing transient Ca^{2+} influx and outflux. Correlated Ca^{2+} oscillations of cells in connected neuronal circuits are necessary for brain functions[141-143]. To evaluate the functionality of the implanted cortical tissues, we performed Ca^{2+} imaging with Fluo-4, a widely used fluorescent calcium indicator.

Fluo-4 is a widely used fluorescent Ca^{2+}-indicator dye, optimized from its former analog, Fluo-3[144]. The membrane-permeant AM ester form of Fluo-4 was usually used, as it can enter into cells via a short-term incubation. Fluo-4 AM ester does not bind Ca^{2+}, but it hydrolyses to Fluo-4 by endogenous esterases in cells. Fluo-4 is considered almost nonfluorescent without Ca^{2+} present, but the fluorescence increases over 100 times when it binds to Ca^{2+}. In addition, as Fluo-4 binds Ca^{2+} more weakly than other dyes, such as fura-2 and indo-1, it is widely used for measuring high transient Ca^{2+} concentration during Ca^{2+} spikes[145].

To perform Ca^{2+} functional analysis, cortical tissue implanted explants on culture inserts were incubated with a mixture of BrainPhys™ Imaging Optimized Medium and Fluo-4 AM before imaging. After incubation, the brain explants were harvested and placed upside down on an imaging dish. Spontaneous calcium fluctuations were recorded at 37°C by fluorescence confocal microscopy at 1 frame per 1.29 s. Time-lapse recordings of implanted explants revealed spontaneous Ca^{2+} oscillations of cells in both the implant and the host brain at 5 DPIs (Figure 5.10 a). We also found simultaneous Ca^{2+} fluctuations in adjacent cells, possibly triggered by the first Ca^{2+} spike. Based on the recording of Ca^{2+} signals, Ca^{2+} traces of interested neurons were drawn, as demonstrated in Figure 5.10. These results suggest a potential correlation between these adjacent cells.

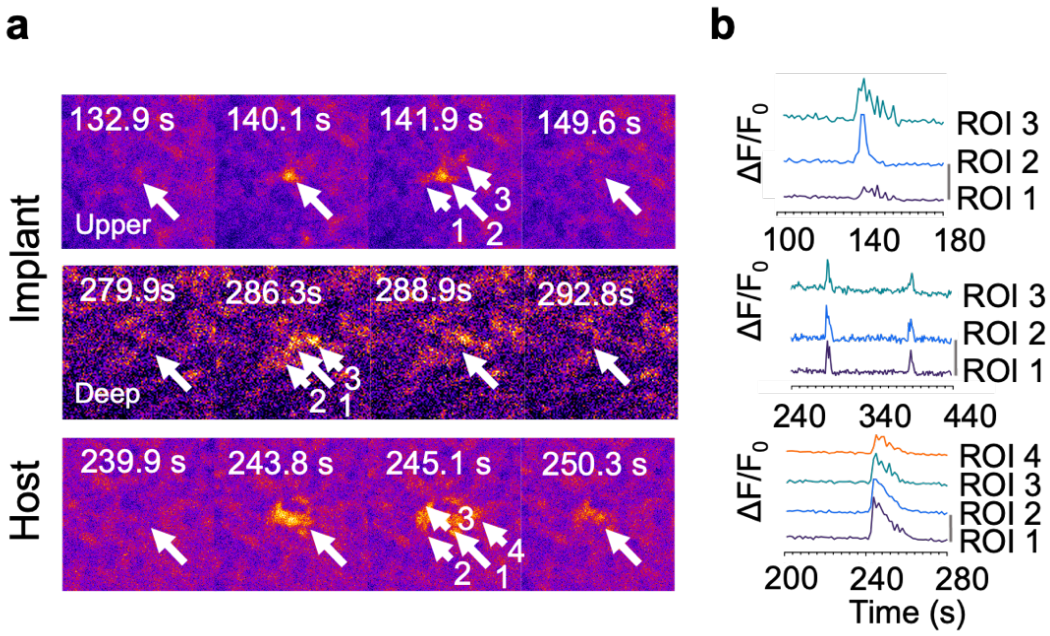

Figure 5.10 Ca^{2+} activity and traces of interested neuron in tissue implanted brain explant. **a.** Frames of Fluo-4 live calcium imaging of the 5 DPIs implanted brain explants demonstrate spontaneous calcium oscillations (colored as fire) in adjacent cells. **b.** Single-cell Fluo-4 calcium traces regions of interest (ROIs) are revealed by arrows in "a."

5.5.2. Functional Analysis between Implant and Host

In the nervous system, correlated Ca^{2+} oscillations of cells in connected neuronal circuits are necessary for brain functions[141-143]. To evaluate the functional connection between the implanted cortical tissues and host brain explant, we performed Ca^{2+} imaging with Fluo-4 to seek correlations of calcium oscillations at the interface. By applying the correlation calculation method reported by Ko et al.[146], we found that the neurons exhibited Ca^{2+} oscillations with a correlation factor of $R > 0.1$ at 5 DPIs, suggesting a functional connection between the implant and the host (Figure 5.11 and Figure 5.12).

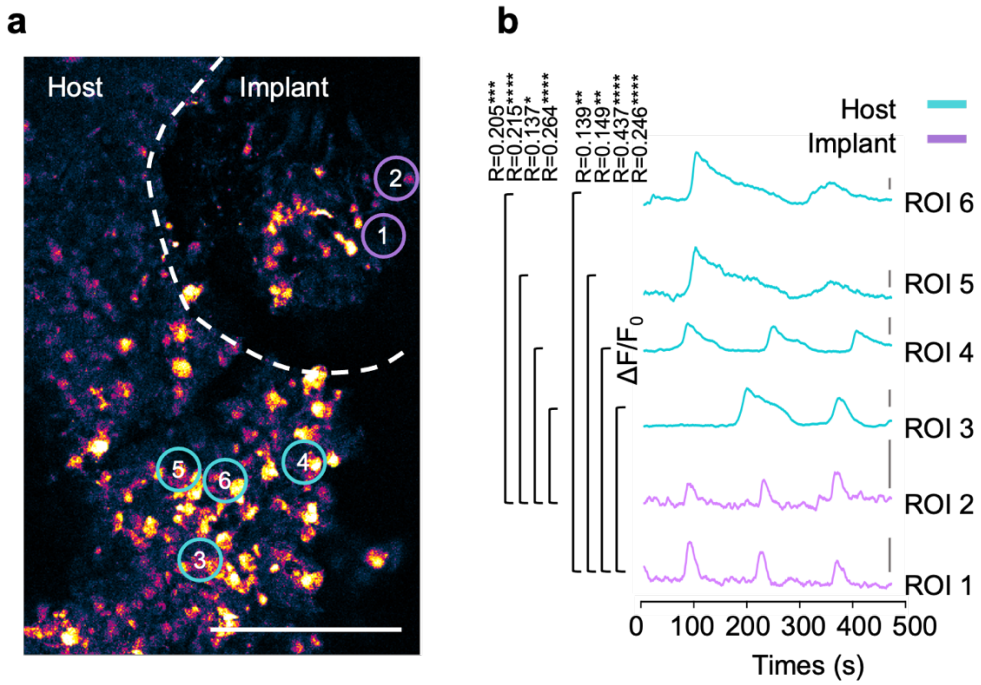

Figure 5.11 Functional analysis of printed tissue implanted brain explant at the interface. **a.** Fluo-4 calcium imaging of a 5-DPI brain explant implanted with DNPs only. The dashed line demonstrates the interface between the implant and the host. Scale bars: 200 µm. **b.** Correlated single-cell calcium traces between implant and host explant. ROIs, as referred to in **"a"**. Scale bar: $\Delta F/F_0 = 0.8$.

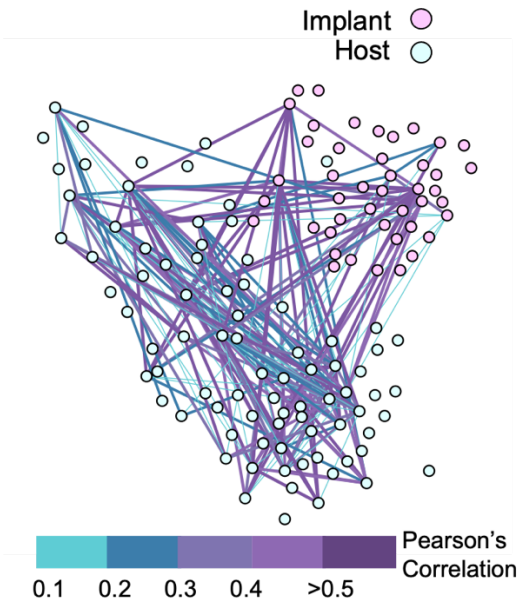

Figure 5.12 Network analysis of a printed tissue implanted brain explant at the interface. Network analysis of firing-correlated neurons between the 5-DPI implant and host is shown in Figure 5.11. Circles correspond to neurons, and lines indicate correlated firings.

To further understand the connection between the implanted cortical tissue and host brain explant, we performed another Ca^{2+} imaging (Figure 5.13a,b) and correlated network assessment (Figure 5.13c) on 5-DPI implanted explants, which demonstrated correlated cell pairs between the implant and the host, and across their boundary. In particular, we demonstrated a group of ROIs with correlated calcium ion traces between implant and host (Figure 5.13d). In general, for implanted explants at 3–5 DPIs, we identified 4.4 ± 0.7% correlated host-to-host cell pairs, 1.6 ± 0.3% host-to-implant cell pairs, and 2.0 ± 0.9% implant-to-implant cell pairs (Figure 5.13e). These results reveal that possible functional connections exist across the boundary and between the printed cerebral cortical and host tissues.

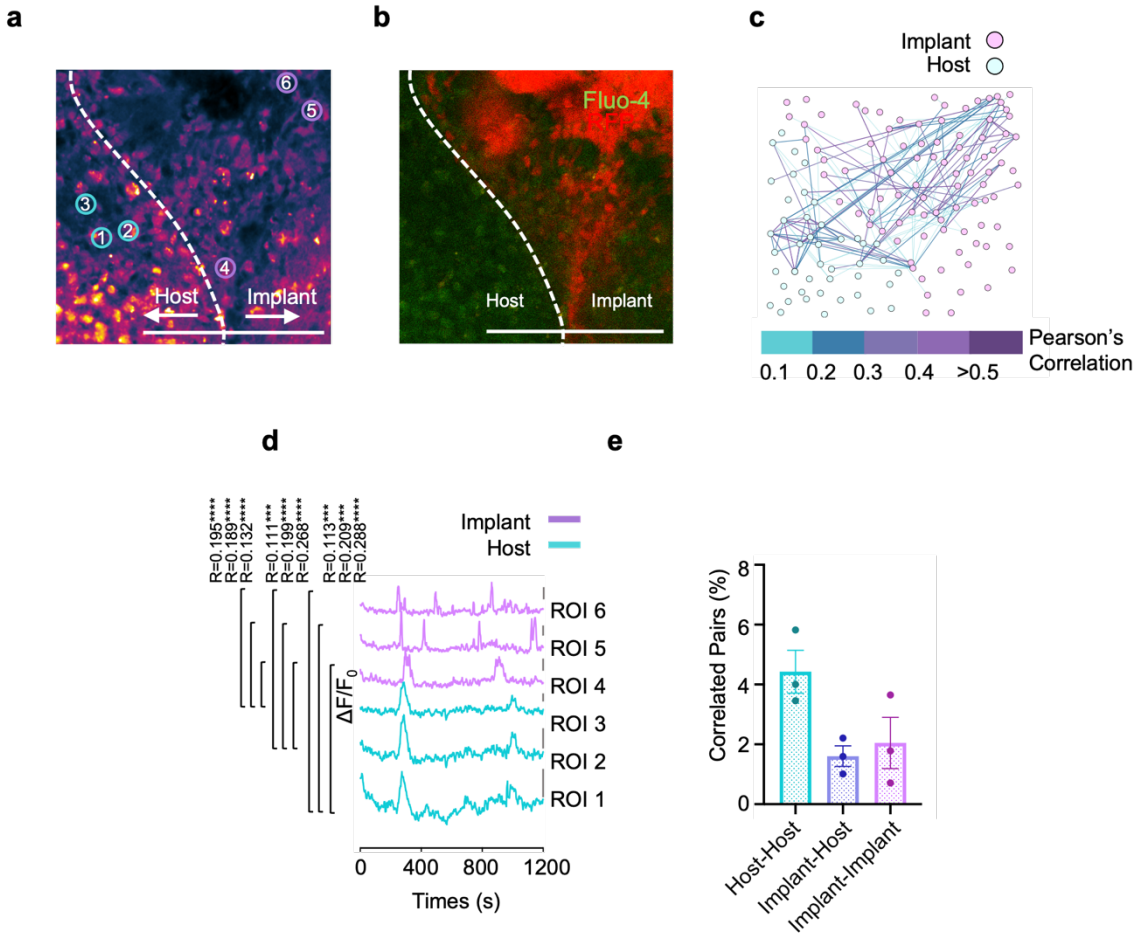

Figure 5.13 Further functional and network analysis of a printed tissue implanted brain explant at the interface.

a. Fluo-4 images of a 5-DPI brain explant implanted with UNPs only. The dashed line demonstrates the interface between the implant and the host. Scale bar: 200 µm. **b.** Fluorescence image of the brain explant implanted with upper layer tissue, as also exhibited in **"a".** The RFP-labeled UNs and Fluo-4 labeled implant and host tissue demonstrate the implant-to-host interface. Scale bar: 200 µm. **c.** Correlated neuron pairs within **"a"** between the 5-DPI implant and the host by network analysis. Points represent neurons, and the lines between them represent correlated calcium signals. **d.** Single-cell calcium traces. ROIs, as referred to **"a"**. Scale bar: ΔF/F0 = 0.05. **e.** Quantitative analysis of the correlated neuron pairs within the host, within the implant, and between the host and implant. Pairs with a Pearson's correlation of more than 0.1 were counted (n = 3).

5.6. Chapter Conclusion

The implantation of single-cell suspension of human neurons into the mouse brain has been published from several groups, showing the survival of transplanted cells, process pathway generation, and implant-host connections[45,78]. However, the transplantation of dissociated cells has not been demonstrated to restore the architecture of lost tissue, such as the laminar structure of the lesioned cerebral cortex. With droplet bioprinting, an implant can be designed using a computer to emulate the dimensions, orientation, cellular composition, and architecture of the lost tissue. In the case of a large lesion, the implantation of printed tissue with a similar 3D structure and cellular architecture can provide a precise replacement. In the current chapter, droplet-printed two-layer cerebral cortical tissues were implanted into P8–10 live mouse brain explants, resulting in structural integration. This integration was demonstrated by implant–host process outgrowth and neuron migration, as well as the functional connection illustrated by Ca^{2+} oscillations correlated between the cortical implant and the host brain explant. Considering the short period of post-implantation incubation (5 days), we presume that the functional connections are caused by the early establishment of volume transmission. Volume transmission is a neuronal signal transmission mechanism that is conducted by the nonsynaptic release of neurotransmitters diffusing through the extracellular space[147,148].

Chapter 6. Discussion and Future Direction

This thesis reports on the progress and implementation of a droplet-based bioprinting technique to pattern hiPSC-derived UNPs and DNPs to form cerebral cortical tissues with the architecture of a simplified two-layer cerebral cortical column. The identity and structure of the deep and upper layers were maintained during *in vitro* culture after printing. During this period, we observed process outgrowth, neuron migration, and maturation. We also described the implantation of printed cortical tissues into brain explants and demonstrated the formation of structural and functional connections between the implant and the host. In this chapter, we discuss the potential future applications of this droplet-based bioprinting technique.

6.1. A Comparison of 3D Bioprinting and Organoids

The advancements of tissue engineering lead to the emergence of various technologies for creating functional human tissues. Two prominent methods that have gained attention are 3D bioprinting, particularly our droplet-based system, and organoids. We included an critical comparison to assess the strengths and limitations of our droplet-based 3D bioprinting in relation to organoids and other related technologies.

6.1.1. Controllability

Droplet-based 3D bioprinting offers precise control over the placement of cells and biomaterials allowing the creation of complex tissue structures. By utilizing computer-aided design models,

we can deposit cells with high spatial resolution (e.g. up to 50 μm in our system), mimicking the native tissue architecture, such as two- or six-layered cerebral cortical column. In contrast, organoids, which are self-organizing cell aggregates, lack the level of control in tissue architecture found in bioprinted constructs[149]. Improved geometry control of organoids were achieved through a combination of bioengineering methods and conventional organoid culture[150].

6.1.2. Scalability

Bioprinting provides an potential scalability by enabling the production of large quantities of tissues with identical structure. This aspect is particularly important for drug testing, disease modeling, and transplantation purposes. A further engineering and manufacturing improvement are required to fulfill the potential of such scalability in the droplet-based 3D bioprinting system. Nevertheless, organoid culture scaling up are challenging due to the variability between different batches or samples, caused by the inherent self-organizing nature of organoid formation[151]. Automated organoids manufacture platform enables the generation of large quantity of organoids with reproducible cell density, diameter, appearance and drug responses. However, the internal structure of those manufactured organoids are still not controllable and reproducible[152].

6.1.3. Functionality

While 3D bioprinting are capable of fabricating pre-designed tissue architectures, it often falls short in recapitulating the intricate cellular interactions and functionality in natural organs. Organoids, on the other hand, can resemble some aspects of organ function due to the its self-regulated formation and cellular heterogeneity. Cerebral cortical organoids, as an example, contains organized neural progenitors, excitatory neurons, inhibitory neurons, astrocytes and oligodendrocyte precursor cells[153]. Cells in the brain organoids can self-assemble into rosette-like structures which can latter form ventricular-like zone, outer subventricular zone and layers

containing deep and upper-layer neurons, making them valuable tools for studying organ development and disease mechanisms[66,154].

6.1.4. Clinical Translation

Both 3D bioprinting and organoids hold a great potential for clinical applications, particularly personalized tissue repair using a patient's own cells. Three-dimensional bioprinting enable the fabrication of tissues that match the cellular components sand structure of the lesion in host. Organoids contain a more complicated combination of cell population, possibly resembling the natural cellular components of the host lesion. However, challenges such as technique robustness, safety, post-implantation vascularization, innervation and long-term functionality are still need to be addressed for both 3D bioprinting and organoids[155-158].

6.1.5. Technological Maturity and Cost:

Three-dimensional bioprinting is a relatively newer technology, which is still undergoing rapid development. The cost of bioprinters, materials, and supporting infrastructure remains high. Organoid culture system are more mature and comparatively affordable. Organoids can be produced using standard laboratory equipment and relatively inexpensive reagents.

6.1.6. Discussion

Three-dimensional bioprinting and organoid offer unique advantages. 3D bioprinting excels in controllability, scalability, while organoids provide functional complexity at a lower cost. Both tissue generation methods face challenges for future clinical translation. The 3D bioprinting and organoid technology has led to a narrowing gap between the two fields. The integration of bioengineering techniques into organoid culture has become increasingly prevalent [149], alongside

the emerging reports on bioprinting of organoids[73]. The choice between these technologies depends on the specific research or clinical application.

6.2. Barrier to Translation

6.2.1. Printing Robustness

The droplet-based 3D bioprinting technology require an enhancement of robustness to produce structural consistent, high-quality living tissues for downstream applications, like drug screening, disease modeling, research of development and clinical implantation.

The relationship between droplet size, ejection speed, and packing quality in bioprinting is intricately intertwined. The voltage and duration for droplet ejection can adjust droplet size and ejection speed. However, these parameters require adjustment following an employment of new printing nozzle. For enhancing process efficiency and robustness, the implementation of standardized, manufactured glass printing nozzles emerges as a critical solution. By standardizing the nozzles, we can mitigate the batch-to-batch variance in droplet size and packing, therefore simplifying the overall procedure and increase the consistency of droplet networks.

Another aspect of robustness lies in accurate temperature and humidity control. Current droplet-based 3D bioprinter relies on Matrigel, which are liquid at ~4°C and solidified at higher temperature. In addition, the dynamics of DIBs formation can be influenced by the environmental temperature and humidity. Therefore, these environmental parameters can affect the behavior of the bioprinting process. Precise control systems, such as a temperature and humidity-controlled chamber encapsulating the bioprinter, would ensure that the bioink and oil-bath maintain their desired properties throughout the process, improving the reliability and repeatability of the prints.

The introduction of an air pressure controlling system to the piezo chamber also can enhance the print quality. Unbalanced air pressure in the printing nozzle, caused by undersealed piezo chamber or other unknown reasons, lead to the leakage or retraction of bioink. An air pressure control system could accurately modulate and re-balance the pressure in piezo chamber and printing nozzle, reducing undesired incidences.

Automated or artificial intelligence-enforced error correction system are also an potential solution to improve their robustness. Error correction can be designed to monitor the real-time printing video and detect droplets that are missed or incorrectly printed, and make necessary adjustments to correct the defect.

The robustness of the 3D bioprinter is essential for paving the way for their widespread use in research and clinical occasions. A comprehensive advancement in engineering and manufacturing are required in enhancing printing robustness. Standardization of printing nozzles, temperature and humidity control, air pressure control and error correction system requires particular attention during the design of bioprinter advancement.

6.2.2. Extracellular Matrix

The current 3D droplet-based bioprinting technique relies on the the utilization of mouse sarcoma-derived Matrigel, due to its features of liquid at 4°C, polymerized at higher temperature and supporting *in vitro* growth and differentiation of delicate cells, like neurons. However, Matrigel presents potential challenges in clinical applications, such as batch-to-batch variation, limited supply, and safety concerns arising from its tumor-derived origin. In order to address the

translational limitation caused by Matrigel, alternatives have been reported by numerous groups. Hydrogels sourced from the ECM of specific tissues have been reported as viable alternatives to Matrigel for organoid production [159]. However, the composition and structure of these hydrogels may still exhibit variation from one batch to another. To overcome the limitations associated with Matrigel or other ECM-derived hydrogels, chemically defined hydrogels for cells and organoids have been reported[160,161]. Our droplet-based method is capable of printing alternative hydrogels, such as collagen and agarose[118]. This versatility holds the potential for future printing of 3D tissues comprising diverse and chemically defined hydrogels.

6.3. Six-layer Cerebral Cortical Tissues

Droplet network printing could take advantage of future discoveries in neural differentiation that generate all layer-specific neurons and thereby produce more realistic six-layer cortical tissues. In the future, the printing technique could print hiPSC-derived cells resembling all six layers in the cerebral cortex to provide a structure that is more comparable with the human cortex. Chapter 2 demonstrated how UNs and DNs can be differentiated from hiPSCs. We believe that there is potential to generate all six-layer cerebral cortical neurons. One possible strategy for doing so is the staggered differentiation method, which harvests cells at distinctive differentiation stages that later mature into different layers of neurons. Another strategy could use genetically encoded critical layer-specific transcription factors or markers with fluorescent proteins owning distinguishable excitation/emission wavelengths. Once the neurons express a layer-specific transcription factor, the fluorescent protein is coexpressed. Therefore, fluorescently labeled cells can be sorted alive using a flow cytometer and replated into a monoculture. Enforced neural-related gene expression can also facilitate the differentiation of neurons[162]. Therefore, we propose

that enhanced expression of layer-specific transcription factors could be another possible approach for generating a homogenous culture of neurons with specific cortical layer phenotypes.

Chapter 3 described the one-, two-, and six-layer network printing procedures. Once all six-layer cortical neurons can be generated, it will be possible to generate tissue assembling all six cerebral cortical layers. However, a printing network containing neural cells is more complicated than printing droplets containing an aqueous solution because of the time limit on cell survival at 4°C, the disturbance of printing fluency by cell particles, and the need for an oil-to-water phase transfer process. Therefore, further engineering of the optimization of the droplet-based printer is essential to achieve this goal. To avoid cell death caused by an extended printing procedure at 4°C, multiple parallel printing nozzles can print a row of droplets rather than a single droplet to speed up the overall printing process and shorten the time required for large, complex, and multiple-layered networks. Printing fluency could be enhanced by employing a standardized printing glass nozzle and precise control of cell dissociation and concentration. We could also develop intelligent software that detects the completeness of each droplet ejection, generating feedback and adjusting pulse amplitude/duration to reduce the incidence of failed droplet ejection, and therefore improve network packing. The oil-to-water phase transfer process is expected to be difficult for large and fragile networks. A microfluidic system that pumps in culture medium at the bottom of the cuvette and pumps out of printing oil at the top is considered a potential approach to improve the phase transfer process. A continuous flow of culture medium and oil exchange can avoid physical disturbances from micropipetting liquid in and out, leading to better preservation of printed networks. Overall, the combination of advanced hiPSC differentiation protocols and an engineering-optimized droplet-printing system would enable the fabrication of tissues that mimic all six layers of cerebral cortex in humans and most other mammals.

6.4. Living Implantation of Cortical Tissues

In the current study, printed cerebral cortical tissue was implanted into the cortex region of brain explants, demonstrating the formation of structural and functional connections between the implant and the host. In the next phase of the study, it will be critical to implant cortical tissue into the lesioned brain cortex of living animals.

TBI damages the cerebral cortex and leads to catastrophic burdens for patients and society. Approximately 69 million people worldwide suffer from TBI, and 4.8 million of these cases are severe[40,41]. However, effective therapeutics for severe TBI are still lacking[44]. Although neural progenitor cells and brain organoids have been implanted in an injured mouse brain model, the structure of the lesioned brain tissue has not been fully restored in these studies[45,46]. Therefore, the implantation of tissues resembling the laminar architecture of the damaged brain cortex could offer a more effective treatment. To investigate the therapeutic effect of such structure-designed tissue made from droplet bioprinting, essential next-phase work involves implanting the tissue into living animal brains and long-term observation.

Neonatal (P2–4) mice or adult mice are two conventional models for studying the response to implantation. Neonatal mice might serve as a good option for a preliminary implantation study due to the higher plasticity of the brain and tolerance of heterogenic materials[163,164]. However, we might face other operational or post-operational challenges, such as the small size of brain and stopping feeding from the mother after surgery[165]. In terms of implantation, classical mouth pipettes are widely used for animal surgery to deliver implants[166]. However, stereotactic intracranial implantation through a stereotaxic frame is increasingly accepted due to its advantage

in enabling precise control of implantation location[167]. C57BL/6J mice, considered the "wild type," are the most commonly used mice for laboratory purposes worldwide. However, these mice might generate immunoreactions to the human-originated cortical tissues and lead to failure in the long-term survival of implants. Immunodeficient mice could serve as a good model for investigating implantation without disturbing the host immune system[168,169]. In real clinical conditions, autologous neural progenitors derived from patients' own reprogrammed iPSCs could be used to produce implants to avoid an undesired immune response[170].

Chapter 7. Method

The author declare that an excerpt of this Method section is also undergoing a publication process of peer-reviewed journal. A pre-print version is available online during the submission of the thesis: https://www.biorxiv.org/content/10.1101/2022.10.28.513987v1?rss=1

7.1. Two-dimensional Cells Generation

7.1.1. hIPSC Maintenance

Cell Lines.

The iPSC lines used in this study were kindly provided by Dr Sally Cowley (James Martin Stem Cell Facility, Oxford). We used three AH016-3 lines: unlabelled, RFP-labelled, and GFP-labelled.

Geltrex Coating

Initially, Geltrex (Thermo Fisher) was shipped and stored at -20°C. Geltrex was defrosted at 4°C for three hours or overnight, and 0.4 mL aliquots were produced in a 50 mL centrifuge tube on ice. To cover cell culture plates, the iPSC culture media (mTeSRplus TM Medium from STEMCELLTM Technologies), culture plates, pipettes, and centrifuge tubes were pre-cooled to 4°C. Geltrex aliquot was removed from -20°C and mixed with 40 mL 4°C mTeSRplus TM

medium before to coating (1:100 dilution). Geltrex solution was used to coat a 6-well, 12-well, 24-well, or 96-well cell culture plate with a suitable volume of 2mL, 1mL, 0.5mL, or 100L diluted Geltrex solution, respectively. A rapid operation is necessary to prevent unwanted Geltrex solidification. The plate containing the Geltrex solution was then incubated at 37°C for one hour to solidify. Two weeks of storage at 4°C is possible for the diluted cold Geltrex solution in a 50mL centrifuge tube.

Resuscitation of Frozen Human iPSC Line

When thawing iPSCs frozen at -80°C or liquid nitrogen, a cryopreservation vial encapsulating the cells was rapidly taken from the -80°C refrigerator or liquid nitrogen tank. The vial was then put and manually thawed in a 37°C water bath while being rotated. When the cells were almost thawed, they were collected and placed in a 15ml centrifuge tube. To counteract the change in osmotic pressure, nine millilitres of pre-warmed, room-temperature mTeSRplus™ medium were introduced to the tube drop-by-drop. Next, the cells were centrifuged for 4 minutes at 200 rcf and resuspended in new mTeSRplus™ media containing 10uM Y-27632 (STEMCELLTM Technologies). One vial of frozen human iPSCs was plated in one well of a 6-well culture plate covered with Geltrex. After resuscitation, the iPSCs were maintained with a daily medium change of mTeSRplus™. Standard iPSC colonies typically develop after two to three days of culture.

Purification of Human iPSC Line

Spontaneous differentiation usually happens when iPSCs are just resuscitated from frozen state. An enzyme-free and non-manual purification method was applied in this experiment instead of time- and labour-consuming physical selection under microscope. These spontaneous differentiated iPSCs were removed by using the ReLeSR™ (STEMCELLTM Technologies), an iPSCs-selective detachment agent. The mTeSRplus ™ medium was firstly aspirated and the cells

washed by DPBS, followed by 1 ml ReLeSR™. The agent was then removed in 40 seconds. With 5 minutes incubation at 37°C, 1mL mTeSRplus ™ medium was added on the cells. The culture plate was then tapped from the side by finger for 40 seconds to facilitate cell detachment. Floated iPSC colonies were subsequently collected and transferred into new Geltrex-coated plate. The purified iPSC colonies were passaged at a 1:1 ratio. The incubation time can be further reduced if a strict selectivity is required.

Maintenance and Passaging of Human iPSC Line

The hiPSC line was cultivated on a 6-well culture plate covered with Geltrex with mTeSRplus™ media and maintained undifferentiated with daily medium changes. An aliquot of mTeSRplus™ media was warmed to room temperature prior to use during the medium change. The old medium was then aspirated and 2 mL of fresh medium was applied to each well of the 6-well plate.

When cell colonies reach roughly 70% confluence, the iPSCs were passed every 3–4 days. First, the mTeSRplus™ medium in one well of a 6-well plate was aspirated, then the well was cleaned with DPBS and 1 mL of ReLeSR™ was added. The agent was then eliminated within 40 seconds. The cells were incubated for 5 minutes at 37°C before 1 mL of mTeSRplus™ medium was added. In order to facilitate cell separation, the culture plate was tapped from the side for 40 seconds. Subsequently, floating iPSC colonies were collected and transferred to a new Geltrex-coated plate. The cells were passed at a ratio of 1:3. If further selectivity is desired, the incubation duration can be shortened further. The selective passaging technique permits the maintenance of a hiPSC line without the increase of spontaneously developed cells over time.

Stock Preservation of Human iPSC Line

When they achieve 70-90% confluency, hiPSCs can be cryopreserved. In a freezing mixture composed of 50% mTeSRplus™ medium, 40% ESC-qualified foetal bovine serum (Gibco® Life Technology), and 10% DMSO, cells were cryopreserved (Sigma-Aldrich Corporation). Before digesting cell, pre-chill freezing medium Mr. Frosty™ Freezing Container (Thermo Scientific™) at 4°C. During cryopreservation, hiPSCs were first digested with 0.5mM EDTA in DPBS (Gibco® Life Technology) at 37°C for 5-7 minutes. After aspiration of spare EDTA, hiPSCs were dispersed by blowing DPBS or any basal medium with 1mL pipette. Single-cell suspension were collected and centrifuged at 200 rcf for 4 mins and resuspended using the pre-chilled freezing medium, which in turn was transferred into cryovials. One well of a 6-well culture plate of hiPSCs were stocked in one cryovial. The cryovials were then transferred into pre-chilled Mr. Frosty™ Freezing Container and stored in -80°C freezer overnight. For long-term preservation, the vials were transferred into liquid nitrogen.

7.1.2. hIPSC Differentiation

Deep-layer Progenitor Differentiation

On DIV -1, hiPSCs were passaged as tiny clusters 1:1 or 3:2 by 0.5mM EDTA (Life Technologies). To accomplish this, cells were treated with 0.5mM Ethylenediaminetetraacetic acid (EDTA; Life Technologies) for 7-10 minutes after being washed with Dulbecco's phosphate-buffered saline (DPBS; Gibco). Following EDTA aspiration, cells were lifted with mTeSRPlus™ media. Collecting floating cells and re-plating them on geltrex-coated plates. 100% confluent hiPSCs were induced on DIV0 using Neural Induction Medium (NIM). The NIM formula is shown in Table 7.1. The medium was replaced everyday with fresh NIM until DIV7. On DIV7, cells were replated, passaged 1:2 using 0.5mM EDTA, and grown in NIM supplemented with 10 μM Y-27683 (Stemcell Technologies). Neural Maintenance Medium was substituted for the culture medium on DIV8 (NMM; Table 7.1). On DIV12, the cells were again passaged 1:2 using EDTA as indicated previously. Using Accutase, cells were passaged 1:2 on DIV 16. (Life Technologies).

The cells were rinsed with DPBS before being treated for 5-7 minutes at 37 °C with 1 mL Accutase. Additional 3mL DMEM/F12 medium (Life Technologies) was added, followed by centrifugation at 200rcf for 5 minutes (g). On geltrex-coated plates, the cell pellet was resuspended in NMM supplemented with 10 μM Y-27683 and replated. On DIV19, hiPSC-DNPs were sent either for cryopreservation as cell stocks or re-plating for research involving terminal maturation. For cryopreservation, DNPs were treated for three hours with 10 μM Y-27683 before to Accutase dissociation. The cell pellets were resuspended in 1mL of pre-chilled freezing medium that included 90% Fetal Bovine Serum (FBS, Gibco) and 10% DMSO (Sigma). The resuspended DNPs were put into cryopreservation vials and stored overnight at -80°C in Freezing Containers (Thermo Scientific) before being transported into liquid nitrogen for long-term storage.

Upper-layer Progenitor Differentiation

DIV19 DNPs were cultured in NMM supplemented with growth factor (GFs) cocktails containing 10ng/mL Fibroblast Growth Factor-2 (FGF-2), Epidermal Growth Factor (EGF) and Brain-derived Neurotrophic Factor (BDNF). The formula for NMM+GFs is listed in Table 7.1. The culture medium was exchanged with fresh medium daily. Once progenitors reach 100% confluency, they were passaged 1:2 using Accutase as described above. The centrifuged cells were resuspended with NMM + GFs and re-plated for sub-cultures. The passaging was performed approximately every 5 days until DIV 40 (since hiPSCs). The DIV 40 UNPs were either cryopreserved or cultured for terminally maturation as the protocol described for DNPs.

Terminal plating of DNPs and UNPs

To recover cryopreserved DNPs or UNPs, the cells were thawed for two days. Then, the cells were replated at a concentration of 100,000/cm^2 in 8- or 96-well plates with Neural Terminal Medium (NTM) supplemented with 10 μM Y-27683 after Accutase passage. The NTM formula

is shown in Table 7.1. Every 3-4 days, the culture medium was replaced with fresh, supplemented NTM. After 10 days, the newly produced neurons were available for evaluation.

Stock Preservation of DNPs and UNPs

When DIV19 and DIV 50+ DNPs and UNPs attain 100 % confluence, they can be cryopreserved. The freezing medium for neural progenitor cells consists of 90% fetal bovine serum (Gibco® Life Technology) and 10% DMSO (Sigma-Aldrich Corporation). Before cell digestion, chill the neural progenitor freezing media and Mr. Frosty^{TM} Freezing Container (Thermo ScientificTM) to 4 degrees Celsius. As indicated above, neural progenitors were first digested using Accutase prior to cryopreservation. Single-cell suspension was collected, centrifuged at 200 rcf for 4 minutes, resuspended in pre-chilled neural progenitor freezing media, and then placed in cryovials. One well of a 6-well culture plate was filled with neural progenitors in a cryovial. The cryovials were then placed in a pre-chilled Mr. Frosty^{TM} Freezing Container and stored overnight in a -80°C freezer. The vials were submerged in liquid nitrogen for long-term preservation.

Resuscitation of DNPs and UNPs

A cryopreservation vial containing neural progenitor was quickly removed from a -80°C freezer or liquid nitrogen tank, and then put and manually thawed in a 37°C water bath. When the cells were nearly thawed, they were collected and placed in a 15ml centrifuge tube. To counteract the shift in osmotic pressure, nine millilitres of pre-warmed, room-temperature Neural Basal media were introduced to the tube drop by drop. The cells were then centrifuged at 200 rcf for 4 minutes and resuspended in new NMM containing 10 μM Y-27632. One vial of frozen human iPSCs was plated on one or four wells of a 6-well or 24-well culture plate coated with Geltrex.

Fixation for Cell Assay

Neurons were cultivated on Geltrex-coated 96-well black polystyrene microplates (Corning) for the majority of cell assays. The neurons were rinsed with DPBS and fixed for 15 minutes at room temperature with 4% paraformaldehyde (PFA). Following fixation, the cells were rinsed three times with ice-cold DPBS and kept in the dark at 4 °C for a maximum of three weeks. If neurons were washed away during fixation, repeat all steps three times with a 50% liquid change each time to reduce physical disturbance caused by liquid movement.

7.2. Three-dimensional Bioprinting

7.2.1. Setup of Bioprinting

The printer was upgraded from what was reported previously[7,76] to provide a two-sided microscopic view for the precise allocation of droplets. For reproducibility, 3D printing was performed in a temperature- and humidity-stable cold room. At 4 °C and 80% relative humidity, Matrigel-based bioink was printed for all studies. Glass printing nozzles were coated with (3-aminopropyl) trimethoxysilane (Sigma) to create a hydrophilic coating that prevented bioink and oil from entering the nozzle and leaking. The printing oil bath comprises 2 mg/mL DPhPC (1, 2-diphytanoyl-sn-glycero-3-phosphocholine, Avanti) in a 1:4 v/v mixture of undecane and silicone oil AR20 (both from Sigma).Associated consumables listed in Table 7.2.

7.2.2. Bioink Preparation and Droplet Bioprinting

Accutase was used to separate cells into single-cell suspensions. Trypan blue staining (Life Technologies) was used to measure cell number and viability, with either a hemocytometer or a Countess II automated cell counter being used to manually or automatically count the cells (ThermoFisher). The cell suspension was then centrifuged at 200 rcf for 5 minutes, after which the supernatant was removed. The pellet was then mixed with pre-thawed Matrigel at 4 °C to

resuspend cells on ice to produce bioink, which was subsequently put into printer nozzles in 4 °C settings. Computer-generated maps were loaded into the customised printing control software for printing. Approximately fifteen minutes were required to print one droplet network. Multiple-material networks were created with either two separate nozzles or a single nozzle by reloading various bioink throughout the printing process.

7.2.3. Network Phase Transfer

The stepped heating procedure was optimized compared with our previous protocol[7,76]. We placed the glass cuvette containing the printed networks in a water bath at room temperature for 20 minutes before transferring it to a 37 °C tissue culture incubator for 1 hour. 2/3 oil was then aspirated and replaced with a mixture of undecane and silicone oil. To dilute the lipid, this oil exchange procedure was repeated five times. To replace the oil, culture medium was then added drop by drop. The medium was then replaced four times to eliminate any remaining oil. The phase-transferred tissue was then transferred to a 12-well or 24-well plate for culture using a 200 L pipette tip with a wide cut.

7.2.4. Printed Tissue

For the first seven days, printed neural cortical tissues were cultured in NMM supplemented with 10ng/mL FGF-2, EGF, BDNF, and 100U/mL Penicillin-Streptomycin (ThermoFisher). The first three days were supplemented with 10 M Y-27683 to prevent cell apoptosis. Then, the cortical tissue was incubated in the NTM for up to 8 weeks with 100U/mL Penicillin-Streptomycin. Every three days, half of the medium was replaced with fresh medium.

7.3. Generation of Implanted Brain Explant

7.3.1. Animal Welfare

According to the Animals Scientific Procedures Act (1986) and licence number PP8557407, all mice were sacrificed by cervical dislocation. All experiments were carefully designed to minimise the number of mice required.

7.3.2. Brain Slicing and Culture

Before obtaining brain slices, the cerebral cortical tissue was printed one day beforehand. The following day, mice P8 C57BL/6J were sacrificed. The skull was opened with surgical scissor and brains were harvested with minimal damage. The harvested brain was stored in ice-cold carbogen-filled (95%O_2/5%CO_2) Earle's Balanced Salt Solution (EBSS, Life technologies). Before sectioning, the brain was embedded in DPBS containing 1.5% UltraPure™ Low Melting Point Agarose (InvitrogenTM). The Agarose-imbedded brain was then adhered to the section stage using superglue. Using a compresstome (Precisionary, VF-310-0Z), coronal slices with a thickness of 300 μm were sliced. Temporarily harvested in chilled carbogen-filled EBSS, the brain slices were transferred and cultured on 0.4-m Millicellculture inserts (Merck Millipore) in six-well plates with the culture medium listed in Table 7.2.

7.3.3. Artificial Lesion

On the same day, a 500-m inner and 800-m outer diameter EMS biopsy punch was used to create a lesion in the cortex of the mouse brain explant. The outside of the lesion circle reached the outer edge of the brain explant, and the inside of the lesion circle reached an approximately 800-μm depth of the cortex, which covered most of the thickness of the cortex (P7 mouse cortex with a thickness of ~800-1000 μm)[133]. We confirmed the lesion is created within the cortex by comparing the location with reference to P7 brain cortex altas in Allen Brain Altas[133].

7.3.4. Tissue Implantation

The printed cortical tissues were removed from the culture plate using a 200 L wide-bored pipette tip and then transferred to the 0.4- μm Millicell-culture inserts containing brain explants. Using needles, printed tissues were micromanipulated and delivered into lesions. The lesion was implanted with two-layered printed cortical tissues whose orientation matched the native cortical structure. Under fluorescent microscope, the orientation of tissues was confirmed both before and after implantation.

7.3.5. Following Culture and Treatment

Then, the implanted brain explants were maintained in a tissue incubator (37°C/5%CO_2) with either nutrient condition A or B culture medium. In Table 7.1, the formulas for conditions A and B were provided. Before using the medium, it was filtered with a 0.22 μm filter. On day two, DAPT was added directly to the culture without changing the medium at a final concentration of 10nM. The medium was replaced every three days. Consumable items listed in Table 7.2.

7.4. Immunocytochemistry for Cell Monolayer

7.4.1. Immunocytochemistry

The neurons were cultured on Geltrex-coated 96 Well Black Polystyrene Microplates (Corning), washed with PBS, and fixed for 15 minutes at room temperature with 4% paraformaldehyde (PFA). After fixation, the cells were washed three times with ice-cold PBS, permeabilized for 20 minutes with 0.1% Triton X-100 in DPBS (DPBST), and then washed three times with DPBS. The cells were then protected from non-specific binding for 60 minutes using 10% goat serum diluted in DPBST. The neurons were then incubated overnight at 4°C with primary antibodies diluted in 1% goat serum in DPBST in a humidified chamber. The neurons were then washed three times with DPBST and incubated for two hours at room temperature with secondary

antibodies diluted in 1% goat serum in DPBST. The information regarding the employed antibodies is provided in

Table 7.3. After incubation, the cells were washed at room temperature three times with DPBST and once with DPBS. The neurons were then mounted with DAPI-containing Antifade Mounting Medium (Abcam). The neurons can be examined directly or stored at 4°C in the dark for later use.

7.4.2. Epi-fluorescent Microscope

Differentiated neurons were imaged using epi-fluorescent microscopes (Leica DMI 8 and Nikon Eclipse Ni-E).

7.4.3. Confocal Microscope

Differentiated neurons were imaged using fluorescence confocal microscopes (Leica LSM780 and Leica SP5)

7.4.4. Quantification Analysis of Immunocytochemistry

For the measurement of cells expressing specific cortical neuronal markers, at least three pictures containing more than 40 cells per field were captured. The cells were counted, and the average cell count for each biologically independent sample was calculated. Associated consumables are listed in Table 7.2.

7.5. Reverse Transcription Quantitative Polymerase Chain Reaction

7.5.1. RNA Isolation

Total RNA was isolated using Monarch@ Total RNA miniprep Kit (New England BioLabs) according to the manufacturer's instruction and described below.

Neurons with maturation over 10 days in NTM were digested by Accutase as described above. After centrifuge, the supernatant was discarded carefully to minimize retained liquid. The cells were snap-frozen by putting the dry pellet of cells in 15mL centrifuge tube into powdered dry ice. Frozen neurons can be stored long-term at -80°C or thawed for subsequent qPCR assessment.

For total RNA isolation, snap-frozen cells pellet was thaw briefly before operation and then resuspended in 600 µL RNA Lysis Buffer by pipetting gently to avoid foaming. For later experiment, all centrifugation steps were performed at 16,000 x g. The mixed sample was then transferred into a gDNA Removal Column (light blue) fitted with a collection tube. Subsequently, it was spined for 30 seconds to remove most of the gDNA. Flow-through was saved and gDNA removal column was discarded.

Equal volume of ethanol was added to the flow-through and mix thoroughly by pipetting. Then, the mixture was transferred to an RNA Purification Column (dark blue) fitted with a collection tube and spined for 30 seconds. Flow-through was discarded. 500 µl RNA Wash Buffer was added into the column and spined for 30 seconds. Flow-through was also discarded. In an RNase-free microfuge tube, 5 µL DNase I and 75 µL DNase I Reaction Buffer mixture was added directly to the top of the matrix. The column was incubated for 15 minutes at room temperature.

After that, 500 µL RNA Priming Buffer was added and spined for 30 seconds. Flow-through was discarded. 500 µL RNA Wash Buffer was then added and spined for 30 seconds. Flow-through

was discarded. Another 500 µL RNA Wash Buffer was added and spined for 2 minutes. Column was then transferred to an RNase-free microfuge tube. 30-100 µL nuclease-free water was added directly to the center of column matrix and spined for 30 seconds.

The eluted RNA was conducted with an additional in-tube DNase I digestion to avoid genomic DNA amplification. For each 40ul sample in microcentrifuge tube, 5 µL DNase I and 5µL DNase I Reaction Buffer was added and incubated at room temperature for 20 minutes. For every 50 µl of treated sample, 100 µl RNA Lysis Buffer was added and mixed thoroughly. An equal volume of ethanol was then added and mixed thoroughly. An RNA binding and elution process as described above was subsequently conducted. For short, the mixture was added to RNA purification column, spined 30 seconds. Addition of 500 µl RNA Priming Buffer with 30 second spin, addition of 500 µl RNA Wash Buffer with 30 second spin, another addition of 500 µl RNA Wash Buffer with 2 minutes spin was sequentially performed. Then, the column was transferred to a microfuge tube. 30-100 µl Nuclease-free Water was added directly to the center of column matrix and spined for 30 seconds. The eluted RNA was either preserved at -80°C freezer or on ice for next step to prepare cDNA preparation. A 2µL RNA solution was used to measure RNA quantity and quality by using a Nanodrop spectrophotometer.

7.5.2. cDNA Generation

The isolated RNA was used for reverse transcription by using the LunaScript@ RT SuperMix Kit (New England BioLab). For cDNA synthesis reaction. Every 20 µL reaction in microcentrifuge tube was prepared with 4 µL LunaScript RT SuperMix (5X), variable RNA sample and appropriate volume of nuclease-free water to make up 20 µL total volume. For no-RT control reactions, every 20 µL reaction in microcentrifuge tube was prepared with 4 µL No-RT Control

Mix (5X), same volume of RNA sample and appropriate volume of nuclease-free water to make up 20 µL total volume. For no template controls, every 20 µL reaction in microcentrifuge tube was prepared with 4 µL LunaScript RT SuperMix (5X) and 16ul nuclease-free water. The microcentrifuges were placed in the thermocycler with following step: Primer Annealing (25 °C, 2 minutes), cDNA Synthesis (55°C, 10 minutes) and Heat Inactivation (95°C, 1minutes) with 1 cycle. The synthesized cDNA can be long-term preserved in -20°C freezer.

7.5.3. RT-qPCR Performance

Quantitative PCR assays were prepared by loading primer mixes and commentary cDNA in triplex wells of 96-well plate followed by the addition of Luna@ Universal qPCR Master Mix (New England BioLab). qPCR reactions were performed using ProFlex PCR System (Applied Biosystem). Parameters (e.g. temperature, time and cycles) were selected according to the manufacturer's (LuanScript) suggestions and discribed below.

Each 20 µL reaction contains 10 µL Luna Universal qPCR Master Mix, 0.5 µL Forward primer (10 µM), 0.5 µL Reverse primer (10 µM), variable Template cDNA and appropriate volume of nuclease-free water to make up 20 µL volume in total.

For preparation, Luna Universal Probe qPCR Master Mix and other reaction components were thawed at room temperature, then placed on ice. After thawing completely, briefly mix each component by inversion, pipetting, or gentle vertexing. Then, Reaction solution with 10% overage was determined and prepared, except DNA template accordingly. Mix solution was added into qPCR plate. Then, cDNA templates were added into plate and sealed with optically transparent film. The plate was spined 1mins at 200 rcf to remove bubbles and collect liquid. The qPCR plate

was then placed in real-time qPCR instrument with thermocycling protocol setup: Initial Denaturation (95 °C , 60 seconds, 1 cycle), Denaturation (95°C , 15 seconds, 45 cycles), Extension (60 °C , 30 seconds, 45 cycles), Melt Curve (60-95°C , 1 cycle). SYBR scan mode was used on the real-time instrument.

7.5.4. RT-qPCR Analysis

The relative gene expression was determined by averaging the results of two to three technical replicates and comparing the Ct values of genes of interest with those of the control gene (18S) using ΔΔCt method. Associated consumables and Primers are listed in Table 7.2 and

Table 7.3

7.6. Characterization for Printed Tissue

7.6.1. Whole-tissue Confocal Scanning

Printed tissue and tissue sections were imaged using fluorescence confocal microscopes (Leica LSM780)

7.6.2. Cryosection

Printed tissues were fixed in 4% v/v paraformaldehyde at room temperature for one hour before being rinsed three times with DPBS. The fixed tissues were encapsulated in optimal cutting temperature compound (OCT, VWR) before being transported to dry ice for snap freezing. The OCT-embedded tissue was subsequently sectioned using a cryostat (Leica, CM1860 UV) to produce 30-µm-thick sections on glass slides for immunostaining.

7.6.3. Immunohistochemistry on Frozen-sectioned Tissue

The tissue sections were circled with a PAP pen (Merck) to create a hydrophobic barrier so that reagents could be localized. The sections were then stained using ‘immunocytochemistry’ method (see above). After tissue sections were stained, they were mounted in Mounting Medium with DAPI (Fluoroshield, Abcam) and sealed with a coverslip and nail polish for 4°C storage. Fluorescence was visualized using a confocal microscope and analyzed using ImageJ. For quantification, three random fields were counted in each of the deep and upper layers and averaged for each biologically independent sample two, four, and eight weeks after the printing culture. For each marker and timepoint, three biologically independent samples were analyzed.

7.6.4. Quantification Analysis of Immunohistochemistry

For the measurement of cells expressing specific cortical neuronal markers, at least three pictures containing more than 40 cells per field were captured for deep or upper layer. The cells were counted, and the average cell count for each biologically independent sample was calculated.

7.6.5. Process Outgrowth and Neuron Migration Analysis

Using ImageJ, two-layer tissue sections were analyzed. The RFP coverage was calculated as the ratio of the RFP-labeled area to the total area of the deep layer, which was defined and quantified by drawing a box encompassing the deep-layer region and utilizing ImageJ's 'threshold' and 'measurement' tools. Using the 'cell counter' plugin in ImageJ, individual migrating neurons were manually selected. Counted as migrated neurons were RFP-labeled neurons with apparent cell bodies and co-localized DAPI staining that were 200 to 400 μm away from the upper-layer boundary.

7.7. Characterization of Implanted Brain Explants

7.7.1. Whole-tissue Confocal Scanning

Explants of the brain were fixed in 4% v/v paraformaldehyde at room temperature for one hour. The brain explants were then washed twice with DPBS with a 5-minute interval between washes. Brain explants were obtained by severing the semipermeable membrane beneath them. For scanning, the brain explant was then positioned toward the objective lens of an inverted confocal microscope. Implanted brain explants were imaged with confocal fluorescence microscopes (Leica LSM780 and Leica LSM980)

7.7.2. Whole-tissue Immunohistochemistry

On post-implantation days 1, 3, or 5, brain explants were fixed in 4% v/v paraformaldehyde at room temperature for 1 hour. Protocol for immunostaining was similar to that described in "Immunohistochemistry of printed tissues." Explants were washed with DPBS, permeabilized with 0.5% Triton X-100 in DPBS (DPBST-0.5%) for 20 minutes, blocked with 10% goat serum in DPBST-0.5% for 60 minutes, and immunostained overnight at 4°C with primary antibodies in 1% goat serum in DPBST-0.5%. The explants were stained for 2 h at room temperature with secondary antibody (see Table 7.3) in 1% goat serum in DPBST-0.5%, followed by DAPI staining (1 g/mL) for 1 h and three DPBST-0.5% washes. Before imaging, the immunostained explants were stored in the dark at 4°C in DPBS.

7.7.3. Live/dead Assay

Before imaging, brain explants at 5 DPI were incubated for 30 minutes with 2.5 μM Calcein-AM (Cambridge Biosciences Ltd) and 5.0 μM propidium iodide (Sigma Aldrich). Imagery was performed on three randomly selected cortical regions of the explants. Images were processed with ImageJ and manually counted.

7.7.4. Implanted Brain Explant Process Outgrowth and Neuron Migration Analysis

The distance of process outgrowth in implanted explants was determined as the maximum distance at which RFP signals could be detected from single-layer implants and HNCAM signals from double-layer implants. The extent of RFP expression in two-layer tissues confirmed the identity of the upper layer. The fluorescence intensities were plotted using 'profile plots' in imageJ, and the width of the decreasing grey value phase was used to represent the outgrowth distance. ImageJ's 'cell counter' plugin was utilised to count individual migratory neurons. Migrating neurons were identified as RFP-labeled neurons with apparent cell bodies and co-localized DAPI staining that were 200 to 400 µm away from the implant-host boundary.

7.7.5. Fluo-4 Calcium Imaging

To determine calcium activities, a Fluo-4 Direct calcium assay kit (Invitrogen) was used according to the manufacturer's instructions. Explants on culture inserts (0.4 µm Millicell, Merck Millipore) were incubated for 1 h at 37°C with a mixture of BrainPhys™ Imaging Optimized Medium (Stemcell Technologies) and Fluo-4 calcium imaging reagents (1:1 v/v). After incubation, brain explants were harvested by removing the semi-permeable membrane from the culture insert and placing them inverted on imaging dishes (Ibidi). At 37°C, calcium fluctuations were captured by fluorescence confocal microscopy (Leica SP5) at a rate of 1 frame every 1.29 seconds.

7.7.6. Fluo-4 Calcium Imaging Analysis

Each video was captured at 1.29 seconds per frame. ImageJ was used to perform pre-processing for calcium analysis. Neurons were identified as bright objects, and ROIs were manually selected. Fluorescence traces were exported as csv files for further Excel analysis of the changes in fluorescence of each ROI throughout the recording period. Subsequently, a functional neuron

connection analysis was conducted using the method described by Ko et al[146]. Briefly, the fluorescence at a given time t (Ft) was normalized for each fluorescence trace as F/F0. F0 represents the average fluorescence value of the first 10 frames. ΔF = Ft-F0. Fluorescence trace smoothed by averaging six frames (Ft/F0 = (Ft-2+Ft-1+Ft+Ft+2+Ft+3 /F0) / 6). Then, background fluorescence was removed from each fluorescence trace by applying a threshold defined as the trace's median value plus 0.02-0.05 to make it more stringent. Each background-filtered trace was then normalized to the range '0-1', with the maximum F/F0 assigned the value '1' and the minimum F/F0 assigned the value '0'. Excel ('Data Analysis> Correlation') was used to calculate Pearson's correlation between pairs of traces in order to generate a correlation matrix containing Pearson's correlations for all possible trace pairs. For correlation visualization, the matrix was imported into R (Rstudio1.3.1093) and plotted using the igraph R package (v1.3.2). We represented the location of ROIs with circles and the Pearson's correlation between pairs of ROIs with lines. In accordance with Ho's report[146], neuron pairs with a Pearson's correlation greater than 0.1 are considered to be correlated. A blue-to-purple color gradient was applied to the lines to indicate low-to-high Pearson's correlation values.

7.8. Statistical Analysis

Data in text are presented as mean ± standard error of the mean (S.E.M.). Data in figures are presented either as mean ± S.E.M. (Figure 2.10, Figure 2.11, Figure 4.12, Figure 4.17, Figure 5.2 b, Figure 5.5 b, Figure 5.6 b, Figure 5.7 b and Figure 5.8 b) or mean ± Standard Deviation (SD) range (Figure 5.8 d). For Figure 2.10, Figure 2.11, Figure 4.12 and Figure 4.17, biological replicates n = 3. For Figure 5.7 b, biological replicates n ≥3. For Figure 5.5 b, biological replicates n ≥4. For Figure 5.6 b, biological replicates n ≥5. For Figure 5.8 b,d, biological replicates n ≥3. For Figure 5.13 e, biological replicates n = 3. Statistical analysis was performed using GraphPad Prism 9.

Table 7.1 Culture Medium Formula

Neural Induction Medium (NIM) 100mL					
Item	**Volume**	**Final Conc**	**Stock Conc**	**Supplier**	**Cat no**
DMEM/F12 Medium	~49 mL	NA	1X	Life Technologies	21331020
Neurobasal Medium	~49 mL	NA	1X	Life Technologies	21103-049
B27 supplement	1 mL	NA	NA	Life Technologies	17504044
N2 supplement	0.5 mL	NA	NA	Life Technologies	17502-048
GlutaMax	1 mL	NA	100X	Life Technologies	35050-038
LDN193189	10 µL	100nM	1 mM	Sigma	SML0559
SB431542	100 µL	10 µM	10 mM	Cambridge Bioscience	ZRD-SB-50
Puromycin (opt)	50 µL	2.5µg/ml	5 mg/ml	MP Biomedicals UK	210055225
Neural Maintenance Medium (NMM) 100mL					
Item	**volume**	**Final Conc**	**Stock Conc**	**Supplier**	**Cat no**
DMEM/F12 Medium	~49 mL	NA	1X	Life Technologies	21331020
Neurobasal Medium	~49 mL	NA	1X	Life Technologies	21103-049
B27 supplement	1 mL	NA	NA	Life Technologies	17504044
N2 supplement	0.5 mL	NA	NA	Life Technologies	17502-048
GlutaMax	1 mL	NA	100X	Life Technologies	35050-038
Puromycin (opt)	50 µL	2.5µg/ml	5 mg/ml	MP Biomedicals UK	210055225
Neural Maintenance Medium + Growth Factors (NMM + GFs) 100mL					
Item	**volume**	**Final Conc**	**Stock Conc**	**Supplier**	**Cat no**
DMEM/F12 Medium	~49 mL	NA	1X	Life Technologies	21331020
Neurobasal Medium	~49 mL	NA	1X	Life Technologies	21103-049
B27 supplement	1 mL	NA	NA	Life Technologies	17504044
N2 supplement	0.5 mL	NA	NA	Life Technologies	17502-048
GlutaMax	1 mL	NA	100X	Life Technologies	35050-038
Fibroblast Growth Factor-2 (FGF-2)	10 µL	10 ng/mL	100µg/mL	R&D Systems	4114-TC-01M
Epidermal Growth Factor (EGF)	10 µL	10 ng/mL	100µg/mL	Life Technologies	PHG0311
Brain-derived Neurotrophic Factor (BDNF)	10 µL	10 ng/mL	100µg/mL	Life Technologies	PHC7074
Freezing Medium 10 mL					
Item	**volume**	**Final Conc**	**Stock Conc**	**Supplier**	**Cat no**
ESC-qualified FBS	9 mL	NA	NA	Gibco	16141061
DMSO	1 mL	NA	NA	Merck	D2650-100ML
Neural Terminal Medium (NTM) 100 mL					
Item	**volume**	**Final Conc**	**Stock Conc**	**Supplier**	**Cat no**
Neurobasal Medium	97 mL	NA	1X	Life Technologies	21103-049
B27 supplement	2 mL	NA	NA	Life Technologies	17504044
GlutaMax	1 mL	NA	100X	Life Technologies	35050-038
DAPT	10 µL	10 µM	100 mM	Tocris	Oct-34
Puromycin (opt)	50 µL	2.5µg/ml	5 mg/ml	MP Biomedicals UK	210055225
Brain Explant Culture Medium Condition A 100mL					
Item	**volume**	**Final Conc**	**Stock Conc**	**Supplier**	**Cat no**
DMEM/F12 Medium	~36 mL	NA	1X	Life Technologies	21331020
Neurobasal Medium	~36 mL	NA	1X	Life Technologies	21103-049
B27 supplement	1 mL	NA	NA	Life Technologies	17504044
N2 supplement	0.5 mL	NA	NA	Life Technologies	17502-048
GlutaMax	1 mL	NA	100X	Life Technologies	35050-038
Pen/Strep	1 mL	NA	10,000 U/mL	Gibco	15140122
Horse Serum	25 mL	NA	NA	Life Technologies	16050130
Brain Explant Culture Medium Condition B 100mL					
Item	**volume**	**Final Conc**	**Stock Conc**	**Supplier**	**Cat no**
Brainphys Neural Medium	72.5 mL	NA	NA	Stemcell Technologies	5792
SM1 supplement	1.5 mL	NA	NA	Stemcell Technologies	5792
Pen/Strep	1 mL	NA	10,000 U/mL	Gibco	15140122
Horse Serum	25 mL	NA	NA	Life Technologies	16050130

Table 7.2 Consumables

Consumables (Cell Culture)					
Item	**volume**	**Final Conc**	**Stock Conc**	**Supplier**	**Cat no**
mTeSR Plus Medium	NA	NA	NA	Stemcell Technologies	100-0276
Geltrex	NA	NA	NA	Gibco	A1413302
StemPro Accutase	NA	NA	NA	Life Technologies	A1110501
DPBS	NA	NA	NA	Gibco	14190144
UltraPure 0.5M EDTA	NA	0.5 mM	0.5 M	Life Technologies	15575020
Distilled Water	NA	NA	NA	Life Technologies	15230089
Y-27632	NA	10 µM	1mM	Abcam	ab120129-10mg
ReLeSR	NA	NA	NA	Stemcell Technologies	5872
Consumables (Droplet Printing)					
Item	**volume**	**Final Conc**	**Stock Conc**	**Supplier**	**Cat no**
Silicone oil AR20	NA	NA	NA	Sigma	10836
Undecane	NA	NA	NA	Sigma	1120-21-4
DPHPC	NA	NA	NA	Avanti	850356
Trimethoxysilane	NA	5% v/v	NA	Sigma	281778
Matrigel	NA	NA	NA	Corning	354230
Consumables (Brain Explant)					
Item	**volume**	**Final Conc**	**Stock Conc**	**Supplier**	**Cat no**
EBSS	NA	NA	NA	Life Technologies	24010043
Culture Insert	NA	NA	NA	Merck	PICM0RG50
X30 Cell Imaging Dish,	NA	NA	NA	Fisher Scientific UK	15670537
BrainPhys Imaging Optimized Medium	NA	NA	NA	Stemcell Technologies	5796
UltraPure Low Melting Point Agarose	NA	NA	NA	Life Technologies	16520050
Microtome blade	NA	NA	NA	Fisher Scientific	11912355
Needle	NA	NA	NA	Fisher Scientific	10749891
Super Glue	NA	NA	NA	Office Depot	4086446
Consumables (qPCR)					
Item	**volume**	**Final Conc**	**Stock Conc**	**Supplier**	**Cat no**
LunaScript(R) RT SuperMix Kit	NA	NA	NA	New England Biolabs	E3010L
Monarch(R) Total RNA Miniprep Kit	NA	NA	NA	New England Biolabs	T2010S
Luna(R) Universal qPCR Master Mix	NA	NA	NA	New England Biolabs	M3003L
MicroAmp Fast Optical 96-Well Reaction Plate	NA	NA	NA	Life Technologies	4346906
Nuclease-Free water	NA	NA	NA	QIAGEN	129114
Consumables (Immunostaining, live/dead assay and Fluo-4 imaging)					
Item	**volume**	**Final Conc**	**Stock Conc**	**Supplier**	**Cat no**
Ibidi µ-Slide 18 Well	NA	NA	NA	ThistleScientific	SKU 81816
Paraformaldehyde 4%	NA	4%	4%	Alfa Aesar	J61899.AK
Glycine 1 M Solution	NA	NA	NA	Merck	67419-1ML-F
Triton X-100	NA	NA	NA	Merck	93443-100ML
Tween-20	NA	NA	NA	Alfa Aesar	P9416-50ML
Normal Goat Serum	NA	NA	NA	Abcam	ab7481
Normal Donkey Serum	NA	NA	NA	Abcam	ab7475
DAPI Solution	NA	1X	10000X	Merck	MBD0015-1ML
Mounting Medium With DAPI	NA	1X	1X	Abcam	ab104139
Fluo-4 Direct Calcium Assay Kit	NA	1X	2X	Life Technologies	F10471
Calcein-AM	NA	2.5 µM	NA	Cambridge bioscience	1755-50
Propidium iodide	NA	5.0 µM	NA	Sigma	P4170
Plastics and others					
1.8ml Cryogenic Vial	NA	NA	NA	STARLAB	E3090-6222
10µl Pipette Tip	NA	NA	NA	STARLAB	S1121-2710
20µl Pipette Tip	NA	NA	NA	STARLAB	S1120-1710
200µl Pipette Tip	NA	NA	NA	STARLAB	S1126-7810
1000µl Pipette Tip	NA	NA	NA	STARLAB	S1120-8810
6 Well Tissue Culture Plate	NA	NA	NA	Greiner Bio-One	657160
12 Well Tissue Culture Plate	NA	NA	NA	Greiner Bio-One	665180
24Well Tissue Culture Plate	NA	NA	NA	Greiner Bio-One	662160
48 Well Tissue Culture Plate	NA	NA	NA	Greiner Bio-One	677180
96 well Tissue Culture Plate	NA	NA	NA	Greiner Bio-One	655180
96 well Assessment Plate	NA	NA	NA	Corning	CLS3603
5mL Stripette	NA	NA	NA	Scientific Laboratory Supp	4487
10mL Stripette	NA	NA	NA	Scientific Laboratory Supp	4488
25mL Stripette	NA	NA	NA	Scientific Laboratory Supp	4489
Cryo Container	NA	NA	NA	VWR International	479-3200
Microslides	NA	NA	NA	VWR International	631-0448
PAP Pen	NA	NA	NA	Merck	Z672548-1EA

Table 7.3 Antibodies and Primers

Primary Antibodies				
Target	**Original Species**	**Manufacturer**	**Dilution Factor**	**Cat. No**
CUX1	Ms	Santa Cruz Biotechnology	100	sc-13024
CUX2	Rb	AbCam	200	ab216588
BRN2	Ms	Santa Cruz Biotechnology	100	sc-393324
SATB2	Rb	AbCam	200	ab92446
CTIP2	Rat	AbCam	200	ab18465
TBR1	Rb	Merck	500	AB10554
SOX2	Rb	Millipore	100-200	ab5603
TUJ1	Ms	AbCam	500-1000	ab78078
GFAP	Rat	Invitrogen	200	13-0300
HNCAM	Rb	AbCam	200	ab75813

Secondary Antibodies					
Target Species	**Original Species**	**Fluorophore**	**Manufacturer**	**Dilution Factor**	**Cat. No**
Rb	Goat	Alex488	Invitrogen	1000	a11006
Ms	Goat	Alex488	Invitrogen	1000	a32723
Ms	Goat	Alex633	Invitrogen	1000	a21052
Rat	Goat	Alex647	Invitrogen	1000	a21247
Rb	Goat	Alex647	Invitrogen	1000	a21245

qPCR Primer			
Target	**Forward or Backward**	**5'-3' Sequence**	**Manufacturer**
PAX6	**F**	GCCAGCAACACACCTAGTCA	Life Technologies
	R	TGTGAGGGCTGTGTCTGTTC	Life Technologies
Nestin	**F**	GGAAGAGAACCTGGGAAAGG	Life Technologies
	R	CTTGGTCCTTCTCCACCGTA	Life Technologies
CTIP2	**F**	GAGTACTGCGGCAAGGTGTT	Life Technologies
	R	TAGTTGCACAGCTCGCACTT	Life Technologies
BRN2	**F**	GACCTTTGCAGGCGAGTAAC	Life Technologies
	R	TCAGGAAGCTGCATTTTGTG	Life Technologies
CUX1	**F**	GCTCTCATCGGCCAATCACT	Life Technologies
	R	TCTATGGCCTGCTCCACGT	Life Technologies
CUX2	**F**	AAGGAGATCGAGTCGCAGAA	Life Technologies
	R	CTCCAGGATGCTCTTGATGG	Life Technologies
18S	**F**	GAGGATGAGGTGGAACGTGT	Life Technologies
	R	TCTTCAGTCGCTCCAGGTCT	Life Technologies

Reference

1 Ngo, T. D., Kashani, A., Imbalzano, G., Nguyen, K. T. Q. & Hui, D. Additive manufacturing (3D printing): A review of materials, methods, applications and challenges. *Composites Part B: Engineering* **143**, 172-196, doi:https://doi.org/10.1016/j.compositesb.2018.02.012 (2018).

2 Murphy, S. V. & Atala, A. 3D bioprinting of tissues and organs. *Nature Biotechnology* **32**, 773-785, doi:10.1038/nbt.2958 (2014).

3 Xu, T. *et al.* Complex heterogeneous tissue constructs containing multiple cell types prepared by inkjet printing technology. *Biomaterials* **34**, 130-139, doi:10.1016/j.biomaterials.2012.09.035 (2013).

4 De Coppi, P. *et al.* Isolation of amniotic stem cell lines with potential for therapy. *Nat Biotechnol* **25**, 100-106, doi:10.1038/nbt1274 (2007).

5 Duan, B., Hockaday, L. A., Kang, K. H. & Butcher, J. T. 3D bioprinting of heterogeneous aortic valve conduits with alginate/gelatin hydrogels. *J Biomed Mater Res A* **101**, 1255-1264, doi:10.1002/jbm.a.34420 (2013).

6 Koch, L. *et al.* Skin tissue generation by laser cell printing. *Biotechnol Bioeng* **109**, 1855-1863, doi:10.1002/bit.24455 (2012).

7 Villar, G., Graham, A. D. & Bayley, H. A tissue-like printed material. *Science* **340**, 48-52, doi:10.1126/science.1229495 (2013).

8 Harris, J. A. *et al.* Hierarchical organization of cortical and thalamic connectivity. *Nature* **575**, 195-202, doi:10.1038/s41586-019-1716-z (2019).

9 Barrett, L. F. & Simmons, W. K. Interoceptive predictions in the brain. *Nat Rev Neurosci* **16**, 419-429, doi:10.1038/nrn3950 (2015).

10 Catala, M. & Kubis, N. in *Handbook of Clinical Neurology* Vol. 115 (eds Gérard Said & Christian Krarup) 29-41 (Elsevier, 2013).

11 Akinrodoye, M. A. & Lui, F. Neuroanatomy, somatic nervous system. (2020).

12 Mahadevan, V. Neuroanatomy: an overview. *Surgery (Oxford)* **36**, 597-605, doi:https://doi.org/10.1016/j.mpsur.2018.09.010 (2018).

13 McCorry, L. K. Physiology of the autonomic nervous system. *Am J Pharm Educ* **71**, 78, doi:10.5688/aj710478 (2007).

14 Jansen, A. S., Van Nguyen, X., Karpitskiy, V., Mettenleiter, T. C. & Loewy, A. D. Central command neurons of the sympathetic nervous system: basis of the fight-or-flight response. *Science* **270**, 644-646 (1995).

15 Glick, G., Braunwald, E. & Lewis, R. M. Relative roles of the sympathetic and parasympathetic nervous systems in the reflex control of heart rate. *Circulation research* **16**, 363-375 (1965).

16 Goyal, R. K. & Hirano, I. The enteric nervous system. *New England Journal of Medicine* **334**, 1106-1115 (1996).

17 Brodal, P. *The central nervous system: structure and function*. (oxford university Press, 2004).

18 McDonald, J. W. & Sadowsky, C. Spinal-cord injury. *The Lancet* **359**, 417-425 (2002).

19 Brambilla, P. *et al.* Brain anatomy and development in autism: review of structural MRI studies. *Brain research bulletin* **61**, 557-569 (2003).

20 Pascual-Leone, A., Amedi, A., Fregni, F. & Merabet, L. B. The plastic human brain cortex. *Annu. Rev. Neurosci.* **28**, 377-401 (2005).

21 Norden, A. D. & Blumenfeld, H. The role of subcortical structures in human epilepsy. *Epilepsy & Behavior* **3**, 219-231 (2002).
22 Jueptner, M., Frith, C., Brooks, D., Frackowiak, R. & Passingham, R. Anatomy of motor learning. II. Subcortical structures and learning by trial and error. *Journal of neurophysiology* **77**, 1325-1337 (1997).
23 Penfield, W. & Rasmussen, T. The cerebral cortex of man; a clinical study of localization of function. (1950).
24 Collins, A. & Koechlin, E. Reasoning, learning, and creativity: frontal lobe function and human decision-making. *PLoS Biol* **10**, e1001293, doi:10.1371/journal.pbio.1001293 (2012).
25 Huttenlocher, P. R. & Dabholkar, A. S. Regional differences in synaptogenesis in human cerebral cortex. *Journal of comparative Neurology* **387**, 167-178 (1997).
26 Jones, E. G. Microcolumns in the cerebral cortex. *Proceedings of the National Academy of Sciences* **97**, 5019-5021 (2000).
27 Shipp, S. Structure and function of the cerebral cortex. *Current Biology* **17**, R443-R449 (2007).
28 Horton, J. C. & Adams, D. L. The cortical column: a structure without a function. *Philosophical Transactions of the Royal Society B: Biological Sciences* **360**, 837-862 (2005).
29 Frantz, G. D. & McConnell, S. K. Restriction of late cerebral cortical progenitors to an upper-layer fate. *Neuron* **17**, 55-61 (1996).
30 Leone, D. P., Srinivasan, K., Chen, B., Alcamo, E. & McConnell, S. K. The determination of projection neuron identity in the developing cerebral cortex. *Current opinion in neurobiology* **18**, 28-35 (2008).
31 Harris, K. D. & Shepherd, G. M. The neocortical circuit: themes and variations. *Nat Neurosci* **18**, 170-181, doi:10.1038/nn.3917 (2015).
32 Kowalczyk, T. *et al.* Intermediate Neuronal Progenitors (Basal Progenitors) Produce Pyramidal–Projection Neurons for All Layers of Cerebral Cortex. *Cerebral Cortex* **19**, 2439-2450, doi:10.1093/cercor/bhn260 (2009).
33 Lemon, R. N., Baker, S. N. & Kraskov, A. Classification of cortical neurons by spike shape and the identification of pyramidal neurons. *Cerebral Cortex* **31**, 5131-5138 (2021).
34 Poirazi, P., Brannon, T. & Mel, B. W. Pyramidal neuron as two-layer neural network. *Neuron* **37**, 989-999 (2003).
35 Connors, B. W. & Kriegstein, A. Cellular physiology of the turtle visual cortex: distinctive properties of pyramidal and stellate neurons. *Journal of Neuroscience* **6**, 164-177 (1986).
36 Gonzalez-Burgos, G., Fish, K. N. & Lewis, D. A. GABA neuron alterations, cortical circuit dysfunction and cognitive deficits in schizophrenia. *Neural plasticity* **2011** (2011).
37 Lewis, D. A., Hashimoto, T. & Volk, D. W. Cortical inhibitory neurons and schizophrenia. *Nature Reviews Neuroscience* **6**, 312-324 (2005).
38 Molyneaux, B. J., Arlotta, P., Menezes, J. R. & Macklis, J. D. Neuronal subtype specification in the cerebral cortex. *Nature reviews neuroscience* **8**, 427-437 (2007).
39 Hevner, R. F. Layer-specific markers as probes for neuron type identity in human neocortex and malformations of cortical development. *Journal of Neuropathology & Experimental Neurology* **66**, 101-109 (2007).
40 Iaccarino, C., Carretta, A., Nicolosi, F. & Morselli, C. Epidemiology of severe traumatic brain injury. *J Neurosurg Sci* **62**, 535-541, doi:10.23736/S0390-5616.18.04532-0 (2018).
41 Dewan, M. C. *et al.* Estimating the global incidence of traumatic brain injury. *J Neurosurg*, 1-18, doi:10.3171/2017.10.JNS17352 (2018).

42 Song, S. Y., Lee, S. K., Eom, K. S. & Investigators, K. Analysis of Mortality and Epidemiology in 2617 Cases of Traumatic Brain Injury : Korean Neuro-Trauma Data Bank System 2010-2014. *J Korean Neurosurg Soc* **59**, 485-491, doi:10.3340/jkns.2016.59.5.485 (2016).
43 Hall, K. M. Establishing a national traumatic brain injury information system based upon a unified data set. *Archives of physical medicine and rehabilitation* **78**, S5-S11 (1997).
44 Galgano, M. *et al.* Traumatic Brain Injury: Current Treatment Strategies and Future Endeavors. *Cell Transplant* **26**, 1118-1130, doi:10.1177/0963689717714102 (2017).
45 Espuny-Camacho, I. *et al.* Human Pluripotent Stem-Cell-Derived Cortical Neurons Integrate Functionally into the Lesioned Adult Murine Visual Cortex in an Area-Specific Way. *Cell Rep* **23**, 2732-2743, doi:10.1016/j.celrep.2018.04.094 (2018).
46 Mansour, A. A. *et al.* An in vivo model of functional and vascularized human brain organoids. *Nat Biotechnol* **36**, 432-441, doi:10.1038/nbt.4127 (2018).
47 Takahashi, K. & Yamanaka, S. Induction of pluripotent stem cells from mouse embryonic and adult fibroblast cultures by defined factors. *Cell* **126**, 663-676, doi:10.1016/j.cell.2006.07.024 (2006).
48 Takahashi, K. *et al.* Induction of pluripotent stem cells from adult human fibroblasts by defined factors. *Cell* **131**, 861-872, doi:10.1016/j.cell.2007.11.019 (2007).
49 Lyra-Leite, D. M. *et al.* A review of protocols for human iPSC culture, cardiac differentiation, subtype-specification, maturation, and direct reprogramming. *STAR Protoc* **3**, 101560, doi:10.1016/j.xpro.2022.101560 (2022).
50 Galiakberova, A. A. & Dashinimaev, E. B. Neural Stem Cells and Methods for Their Generation From Induced Pluripotent Stem Cells in vitro. *Front Cell Dev Biol* **8**, 815, doi:10.3389/fcell.2020.00815 (2020).
51 Magdy, T., Schuldt, A. J. T., Wu, J. C., Bernstein, D. & Burridge, P. W. Human Induced Pluripotent Stem Cell (hiPSC)-Derived Cells to Assess Drug Cardiotoxicity: Opportunities and Problems. *Annual Review of Pharmacology and Toxicology* **58**, 83-103, doi:10.1146/annurev-pharmtox-010617-053110 (2018).
52 Shi, Y., Kirwan, P. & Livesey, F. J. Directed differentiation of human pluripotent stem cells to cerebral cortex neurons and neural networks. *Nature Protocols* **7**, 1836-1846, doi:10.1038/nprot.2012.116 (2012).
53 Shi, Y., Kirwan, P., Smith, J., Robinson, H. P. C. & Livesey, F. J. Human cerebral cortex development from pluripotent stem cells to functional excitatory synapses. *Nature Neuroscience* **15**, 477-486, doi:10.1038/nn.3041 (2012).
54 Shen, Q. *et al.* The timing of cortical neurogenesis is encoded within lineages of individual progenitor cells. *Nature Neuroscience* **9**, 743-751, doi:10.1038/nn1694 (2006).
55 Boissart, C. *et al.* Differentiation from human pluripotent stem cells of cortical neurons of the superficial layers amenable to psychiatric disease modeling and high-throughput drug screening. *Translational Psychiatry* **3**, e294-e294, doi:10.1038/tp.2013.71 (2013).
56 Lelièvre, S. A., Kwok, T. & Chittiboyina, S. Architecture in 3D cell culture: An essential feature for in vitro toxicology. *Toxicol In Vitro* **45**, 287-295, doi:10.1016/j.tiv.2017.03.012 (2017).
57 Lawko, N. *et al.* 3D Tissue Models as an Effective Tool for Studying Viruses and Vaccine Development. *Frontiers in Materials* **8**, doi:10.3389/fmats.2021.631373 (2021).
58 Kim, J., Koo, B.-K. & Knoblich, J. A. Human organoids: model systems for human biology and medicine. *Nature Reviews Molecular Cell Biology* **21**, 571-584, doi:10.1038/s41580-020-0259-3 (2020).

59 Andersen, J. *et al.* Generation of Functional Human 3D Cortico-Motor Assembloids. *Cell* **183**, 1913-1929.e1926, doi:10.1016/j.cell.2020.11.017 (2020).
60 Masters, J. R. W. Human cancer cell lines: fact and fantasy. *Nature Reviews Molecular Cell Biology* **1**, 233-236, doi:10.1038/35043102 (2000).
61 Robinson, N. B. *et al.* The current state of animal models in research: A review. *Int J Surg* **72**, 9-13, doi:10.1016/j.ijsu.2019.10.015 (2019).
62 Levy, A. *et al.* Extrapolating from animal studies to the efficacy in humans of a pretreatment combination against organophosphate poisoning. *Arch Toxicol* **81**, 353-359, doi:10.1007/s00204-006-0153-6 (2007).
63 Han, Y., Yang, L., Lacko, L. A. & Chen, S. Human organoid models to study SARS-CoV-2 infection. *Nature Methods* **19**, 418-428, doi:10.1038/s41592-022-01453-y (2022).
64 Perez-Lanzon, M., Kroemer, G. & Maiuri, M. C. Organoids for Modeling Genetic Diseases. *Int Rev Cell Mol Biol* **337**, 49-81, doi:10.1016/bs.ircmb.2017.12.006 (2018).
65 Drost, J. & Clevers, H. Organoids in cancer research. *Nature Reviews Cancer* **18**, 407-418, doi:10.1038/s41568-018-0007-6 (2018).
66 Lancaster, M. A. *et al.* Cerebral organoids model human brain development and microcephaly. *Nature* **501**, 373-379 (2013).
67 Velasco, S. *et al.* Individual brain organoids reproducibly form cell diversity of the human cerebral cortex. *Nature* **570**, 523-527, doi:10.1038/s41586-019-1289-x (2019).
68 Hofer, M. & Lutolf, M. P. Engineering organoids. *Nature Reviews Materials* **6**, 402-420, doi:10.1038/s41578-021-00279-y (2021).
69 Miura, Y. *et al.* Generation of human striatal organoids and cortico-striatal assembloids from human pluripotent stem cells. *Nature Biotechnology* **38**, 1421-1430, doi:10.1038/s41587-020-00763-w (2020).
70 Miura, Y. *et al.* Engineering brain assembloids to interrogate human neural circuits. *Nature Protocols* **17**, 15-35, doi:10.1038/s41596-021-00632-z (2022).
71 Li, J., Chen, M., Fan, X. & Zhou, H. Recent advances in bioprinting techniques: approaches, applications and future prospects. *Journal of Translational Medicine* **14**, 271, doi:10.1186/s12967-016-1028-0 (2016).
72 Boularaoui, S., Al Hussein, G., Khan, K. A., Christoforou, N. & Stefanini, C. An overview of extrusion-based bioprinting with a focus on induced shear stress and its effect on cell viability. *Bioprinting* **20**, e00093, doi:https://doi.org/10.1016/j.bprint.2020.e00093 (2020).
73 Brassard, J. A., Nikolaev, M., Hübscher, T., Hofer, M. & Lutolf, M. P. Recapitulating macro-scale tissue self-organization through organoid bioprinting. *Nature Materials* **20**, 22-29 (2021).
74 Yang, H., Yang, K. H., Narayan, R. J. & Ma, S. Laser-based bioprinting for multilayer cell patterning in tissue engineering and cancer research. *Essays Biochem* **65**, 409-416, doi:10.1042/ebc20200093 (2021).
75 Wang, Z. *et al.* A simple and high-resolution stereolithography-based 3D bioprinting system using visible light crosslinkable bioinks. *Biofabrication* **7**, 045009, doi:10.1088/1758-5090/7/4/045009 (2015).
76 Zhou, L. *et al.* Lipid-Bilayer-Supported 3D Printing of Human Cerebral Cortex Cells Reveals Developmental Interactions. *Advanced Materials* **32**, 2002183, doi:https://doi.org/10.1002/adma.202002183 (2020).
77 Kim, J.-H. *et al.* Dopamine neurons derived from embryonic stem cells function in an animal model of Parkinson's disease. *Nature* **418**, 50-56, doi:10.1038/nature00900 (2002).

78 Linaro, D. *et al.* Xenotransplanted Human Cortical Neurons Reveal Species-Specific Development and Functional Integration into Mouse Visual Circuits. *Neuron* **104**, 972-986.e976, doi:10.1016/j.neuron.2019.10.002 (2019).
79 Mansour, A. A. *et al.* An in vivo model of functional and vascularized human brain organoids. *Nature biotechnology* **36**, 432-441 (2018).
80 Revah, O. *et al.* Maturation and circuit integration of transplanted human cortical organoids. *Nature* **610**, 319-326, doi:10.1038/s41586-022-05277-w (2022).
81 Gaspard, N. *et al.* An intrinsic mechanism of corticogenesis from embryonic stem cells. *Nature* **455**, 351-357, doi:10.1038/nature07287 (2008).
82 Rakic, P. Neurons in Rhesus Monkey Visual Cortex: Systematic Relation between Time of Origin and Eventual Disposition. *Science* **183**, 425-427, doi:10.1126/science.183.4123.425 (1974).
83 Hu, B.-Y. *et al.* Neural differentiation of human induced pluripotent stem cells follows developmental principles but with variable potency. *Proceedings of the National Academy of Sciences* **107**, 4335-4340, doi:doi:10.1073/pnas.0910012107 (2010).
84 Shahjalal, H. M., Abdal Dayem, A., Lim, K. M., Jeon, T.-i. & Cho, S.-G. Generation of pancreatic β cells for treatment of diabetes: advances and challenges. *Stem Cell Research & Therapy* **9**, 355, doi:10.1186/s13287-018-1099-3 (2018).
85 Corbett, J. L. & Duncan, S. A. iPSC-Derived Hepatocytes as a Platform for Disease Modeling and Drug Discovery. *Front Med (Lausanne)* **6**, 265, doi:10.3389/fmed.2019.00265 (2019).
86 Schopperle, W. M. & DeWolf, W. C. The TRA-1-60 and TRA-1-81 human pluripotent stem cell markers are expressed on podocalyxin in embryonal carcinoma. *Stem Cells* **25**, 723-730, doi:10.1634/stemcells.2005-0597 (2007).
87 Ling, G. Q., Chen, D. B., Wang, B. Q. & Zhang, L. S. Expression of the pluripotency markers Oct3/4, Nanog and Sox2 in human breast cancer cell lines. *Oncol Lett* **4**, 1264-1268, doi:10.3892/ol.2012.916 (2012).
88 Shi, G. & Jin, Y. Role of Oct4 in maintaining and regaining stem cell pluripotency. *Stem Cell Research & Therapy* **1**, 39, doi:10.1186/scrt39 (2010).
89 Nagasaka, R. *et al.* Visualization of morphological categories of colonies for monitoring of effect on induced pluripotent stem cell culture status. *Regenerative Therapy* **6**, 41-51, doi:https://doi.org/10.1016/j.reth.2016.12.003 (2017).
90 Gunhanlar, N. *et al.* A simplified protocol for differentiation of electrophysiologically mature neuronal networks from human induced pluripotent stem cells. *Molecular Psychiatry* **23**, 1336-1344, doi:10.1038/mp.2017.56 (2018).
91 Li, Y. *et al.* An optimized method for neuronal differentiation of embryonic stem cells in vitro. *J Neurosci Methods* **330**, 108486, doi:10.1016/j.jneumeth.2019.108486 (2020).
92 Faye, P. A. *et al.* Optimized Protocol to Generate Spinal Motor Neuron Cells from Induced Pluripotent Stem Cells from Charcot Marie Tooth Patients. *Brain Sci* **10**, doi:10.3390/brainsci10070407 (2020).
93 Haenseler, W. *et al.* A Highly Efficient Human Pluripotent Stem Cell Microglia Model Displays a Neuronal-Co-culture-Specific Expression Profile and Inflammatory Response. *Stem Cell Reports* **8**, 1727-1742, doi:10.1016/j.stemcr.2017.05.017 (2017).
94 Dovey, H. F. *et al.* Functional gamma-secretase inhibitors reduce beta-amyloid peptide levels in brain. *J Neurochem* **76**, 173-181, doi:10.1046/j.1471-4159.2001.00012.x (2001).
95 Sastre, M. *et al.* Presenilin-dependent γ-secretase processing of β-amyloid precursor protein at a site corresponding to the S3 cleavage of Notch. *EMBO reports* **2**, 835-841 (2001).

96 Crawford, T. Q. & Roelink, H. The notch response inhibitor DAPT enhances neuronal differentiation in embryonic stem cell-derived embryoid bodies independently of sonic hedgehog signaling. *Developmental dynamics: an official publication of the American Association of Anatomists* **236**, 886-892 (2007).
97 Qi, Y. *et al.* Combined small-molecule inhibition accelerates the derivation of functional cortical neurons from human pluripotent stem cells. *Nat Biotechnol* **35**, 154-163, doi:10.1038/nbt.3777 (2017).
98 Matos, L. L., Trufelli, D. C., de Matos, M. G. & da Silva Pinhal, M. A. Immunohistochemistry as an important tool in biomarkers detection and clinical practice. *Biomark Insights* **5**, 9-20, doi:10.4137/bmi.s2185 (2010).
99 Hevner, R. F. *et al.* Tbr1 Regulates Differentiation of the Preplate and Layer 6. *Neuron* **29**, 353-366, doi:https://doi.org/10.1016/S0896-6273(01)00211-2 (2001).
100 Bedogni, F. *et al.* Tbr1 regulates regional and laminar identity of postmitotic neurons in developing neocortex. *Proc Natl Acad Sci U S A* **107**, 13129-13134, doi:10.1073/pnas.1002285107 (2010).
101 Han, W. *et al.* TBR1 directly represses Fezf2 to control the laminar origin and development of the corticospinal tract. *Proceedings of the National Academy of Sciences* **108**, 3041-3046 (2011).
102 Leid, M. *et al.* CTIP1 and CTIP2 are differentially expressed during mouse embryogenesis. *Gene Expr Patterns* **4**, 733-739, doi:10.1016/j.modgep.2004.03.009 (2004).
103 Cánovas, J. *et al.* The Specification of Cortical Subcerebral Projection Neurons Depends on the Direct Repression of TBR1 by CTIP1/BCL11a. *J Neurosci* **35**, 7552-7564, doi:10.1523/jneurosci.0169-15.2015 (2015).
104 Nieto, M. *et al.* Expression of Cux-1 and Cux-2 in the subventricular zone and upper layers II–IV of the cerebral cortex. *Journal of Comparative Neurology* **479**, 168-180 (2004).
105 Cubelos, B. *et al.* Cux1 and Cux2 Regulate Dendritic Branching, Spine Morphology, and Synapses of the Upper Layer Neurons of the Cortex. *Neuron* **66**, 523-535, doi:https://doi.org/10.1016/j.neuron.2010.04.038 (2010).
106 Sugitani, Y. *et al.* Brn-1 and Brn-2 share crucial roles in the production and positioning of mouse neocortical neurons. *Genes Dev* **16**, 1760-1765, doi:10.1101/gad.978002 (2002).
107 Alcamo, E. A. *et al.* Satb2 regulates callosal projection neuron identity in the developing cerebral cortex. *Neuron* **57**, 364-377, doi:10.1016/j.neuron.2007.12.012 (2008).
108 Fenlon, L. R. *et al.* Formation of functional areas in the cerebral cortex is disrupted in a mouse model of autism spectrum disorder. *Neural Development* **10**, 10, doi:10.1186/s13064-015-0033-y (2015).
109 Cipriani, S. *et al.* Dynamic Expression Patterns of Progenitor and Pyramidal Neuron Layer Markers in the Developing Human Hippocampus. *Cereb Cortex* **26**, 1255-1271, doi:10.1093/cercor/bhv079 (2016).
110 Hevner, R. F. Layer-specific markers as probes for neuron type identity in human neocortex and malformations of cortical development. *J Neuropathol Exp Neurol* **66**, 101-109, doi:10.1097/nen.0b013e3180301c06 (2007).
111 Taupin, P. *et al.* FGF-2-responsive neural stem cell proliferation requires CCg, a novel autocrine/paracrine cofactor. *Neuron* **28**, 385-397, doi:10.1016/s0896-6273(00)00119-7 (2000).
112 Lim, J. Y. *et al.* Brain-derived neurotrophic factor stimulates the neural differentiation of human umbilical cord blood-derived mesenchymal stem cells and survival of differentiated cells through MAPK/ERK and PI3K/Akt-dependent signaling pathways. *J Neurosci Res* **86**, 2168-2178, doi:10.1002/jnr.21669 (2008).

113 Bustin, S. A. *AZ of quantitative PCR*. (International University Line La Jolla, CA, 2004).
114 Zhang, X. *et al.* Pax6 is a human neuroectoderm cell fate determinant. *Cell stem cell* **7**, 90-100 (2010).
115 Park, D. *et al.* Nestin is required for the proper self-renewal of neural stem cells. *Stem cells* **28**, 2162-2171 (2010).
116 Ma, S., Mukherjee, N., Mikhailova, E. & Bayley, H. Gel Microrods for 3D Tissue Printing. *Adv Biosyst* **1**, e1700075, doi:10.1002/adbi.201700075 (2017).
117 Aisenbrey, E. A. & Murphy, W. L. Synthetic alternatives to Matrigel. *Nat Rev Mater* **5**, 539-551, doi:10.1038/s41578-020-0199-8 (2020).
118 Krishna Kumar, R. *et al.* Droplet printing reveals the importance of micron-scale structure for bacterial ecology. *Nature Communications* **12**, 857, doi:10.1038/s41467-021-20996-w (2021).
119 Zhou, L. *et al.* Lipid-Bilayer-Supported 3D Printing of Human Cerebral Cortex Cells Reveals Developmental Interactions. *Adv Mater* **32**, e2002183, doi:10.1002/adma.202002183 (2020).
120 Mason, J. O. & Price, D. J. Building brains in a dish: Prospects for growing cerebral organoids from stem cells. *Neuroscience* **334**, 105-118, doi:https://doi.org/10.1016/j.neuroscience.2016.07.048 (2016).
121 Renner, M. *et al.* Self-organized developmental patterning and differentiation in cerebral organoids. *The EMBO Journal* **36**, 1316-1329, doi:https://doi.org/10.15252/embj.201694700 (2017).
122 Karra, D. & Dahm, R. Transfection Techniques for Neuronal Cells. *The Journal of Neuroscience* **30**, 6171, doi:10.1523/JNEUROSCI.0183-10.2010 (2010).
123 Skylar-Scott, M. A. *et al.* Orthogonally induced differentiation of stem cells for the programmatic patterning of vascularized organoids and bioprinted tissues. *Nat Biomed Eng*, doi:10.1038/s41551-022-00856-8 (2022).
124 Milone, M. C. & O'Doherty, U. Clinical use of lentiviral vectors. *Leukemia* **32**, 1529-1541, doi:10.1038/s41375-018-0106-0 (2018).
125 Matsushita, M. *et al.* Neural differentiation of human embryonic stem cells induced by the transgene-mediated overexpression of single transcription factors. *Biochemical and Biophysical Research Communications* **490**, 296-301, doi:https://doi.org/10.1016/j.bbrc.2017.06.039 (2017).
126 Wolf, M. K. Anatomy of cultured mouse cerebellum. II. Organotypic migration of granule cells demonstrated by silver impregnation of normal and mutant cultures. *Journal of Comparative Neurology* **140**, 281-297 (1970).
127 Humpel, C. Organotypic brain slice cultures: A review. *Neuroscience* **305**, 86-98, doi:https://doi.org/10.1016/j.neuroscience.2015.07.086 (2015).
128 Croft, C. L., Futch, H. S., Moore, B. D. & Golde, T. E. Organotypic brain slice cultures to model neurodegenerative proteinopathies. *Molecular Neurodegeneration* **14**, 45, doi:10.1186/s13024-019-0346-0 (2019).
129 Noraberg, J. *et al.* Organotypic hippocampal slice cultures for studies of brain damage, neuroprotection and neurorepair. *Current Drug Targets-CNS & Neurological Disorders* **4**, 435-452 (2005).
130 Jung, S. *et al.* Brain tumor invasion model system using organotypic brain-slice culture as an alternative to in vivo model. *Journal of cancer research and clinical oncology* **128**, 469-476 (2002).

131 Bardy, C. *et al.* Neuronal medium that supports basic synaptic functions and activity of human neurons in vitro. *Proceedings of the National Academy of Sciences* **112**, E2725-E2734, doi:doi:10.1073/pnas.1504393112 (2015).
132 Chen, X. *et al.* High Glucose Inhibits Neural Stem Cell Differentiation Through Oxidative Stress and Endoplasmic Reticulum Stress. *Stem Cells Dev* **27**, 745-755, doi:10.1089/scd.2017.0203 (2018).
133 Science, A. I. f. B. Allen Mouse Brain Atlas. *Available from* https://developingmouse.brain-map.org/experiment/thumbnails/100098039?image_type=nissl (2004).
134 Bratosin, D., Mitrofan, L., Palii, C., Estaquier, J. & Montreuil, J. Novel fluorescence assay using calcein-AM for the determination of human erythrocyte viability and aging. *Cytometry Part A: the journal of the International Society for Analytical Cytology* **66**, 78-84 (2005).
135 Dumitriu, I. E. *et al.* 5,6-carboxyfluorescein diacetate succinimidyl ester-labeled apoptotic and necrotic as well as detergent-treated cells can be traced in composite cell samples. *Anal Biochem* **299**, 247-252, doi:10.1006/abio.2001.5415 (2001).
136 Yu, T. W. & Bargmann, C. I. Dynamic regulation of axon guidance. *Nat Neurosci* **4 Suppl**, 1169-1176, doi:10.1038/nn748 (2001).
137 Myers, J. P., Santiago-Medina, M. & Gomez, T. M. Regulation of axonal outgrowth and pathfinding by integrin-ECM interactions. *Dev Neurobiol* **71**, 901-923, doi:10.1002/dneu.20931 (2011).
138 Jørgensen, O. S. Neural cell adhesion molecule (NCAM) as a quantitative marker in synaptic remodeling. *Neurochem Res* **20**, 533-547, doi:10.1007/bf01694535 (1995).
139 Smetters, D., Majewska, A. & Yuste, R. Detecting Action Potentials in Neuronal Populations with Calcium Imaging. *Methods* **18**, 215-221, doi:https://doi.org/10.1006/meth.1999.0774 (1999).
140 Simms, Brett A. & Zamponi, Gerald W. Neuronal Voltage-Gated Calcium Channels: Structure, Function, and Dysfunction. *Neuron* **82**, 24-45, doi:https://doi.org/10.1016/j.neuron.2014.03.016 (2014).
141 Heck, D. H., Thach, W. T. & Keating, J. G. On-beam synchrony in the cerebellum as the mechanism for the timing and coordination of movement. *Proceedings of the National Academy of Sciences* **104**, 7658-7663, doi:doi:10.1073/pnas.0609966104 (2007).
142 Grienberger, C. & Konnerth, A. Imaging calcium in neurons. *Neuron* **73**, 862-885, doi:10.1016/j.neuron.2012.02.011 (2012).
143 Dupont, E., Hanganu, I. L., Kilb, W., Hirsch, S. & Luhmann, H. J. Rapid developmental switch in the mechanisms driving early cortical columnar networks. *Nature* **439**, 79-83, doi:10.1038/nature04264 (2006).
144 Gee, K. R. *et al.* Chemical and physiological characterization of fluo-4 Ca2+-indicator dyes. *Cell Calcium* **27**, 97-106, doi:https://doi.org/10.1054/ceca.1999.0095 (2000).
145 Kao, J. P., Li, G. & Auston, D. A. in *Methods in cell biology* Vol. 99 113-152 (Elsevier, 2010).
146 Ko, H. *et al.* Functional specificity of local synaptic connections in neocortical networks. *Nature* **473**, 87-91, doi:10.1038/nature09880 (2011).
147 Agnati, L. F. *et al.* A correlation analysis of the regional distribution of central enkephalin and β-endorphin immunoreactive terminals and of opiate receptors in adult and old male rats. Evidence for the existence of two main types of communication in the central nervous system: the volume transmission and the wiring transmission. *Acta Physiologica Scandinavica* **128**, 201-207 (1986).

148 Agnati, L. F., Guidolin, D., Guescini, M., Genedani, S. & Fuxe, K. Understanding wiring and volume transmission. *Brain Research Reviews* **64**, 137-159, doi:https://doi.org/10.1016/j.brainresrev.2010.03.003 (2010).
149 Garreta, E. *et al.* Rethinking organoid technology through bioengineering. *Nature Materials* **20**, 145-155, doi:10.1038/s41563-020-00804-4 (2021).
150 Gjorevski, N. *et al.* Tissue geometry drives deterministic organoid patterning. *Science* **375**, eaaw9021, doi:doi:10.1126/science.aaw9021 (2022).
151 Rossi, G., Manfrin, A. & Lutolf, M. P. Progress and potential in organoid research. *Nature Reviews Genetics* **19**, 671-687, doi:10.1038/s41576-018-0051-9 (2018).
152 Jiang, S. *et al.* An Automated Organoid Platform with Inter-organoid Homogeneity and Inter-patient Heterogeneity. *Cell Rep Med* **1**, 100161, doi:10.1016/j.xcrm.2020.100161 (2020).
153 Qian, X., Song, H. & Ming, G. L. Brain organoids: advances, applications and challenges. *Development* **146**, doi:10.1242/dev.166074 (2019).
154 Di Lullo, E. & Kriegstein, A. R. The use of brain organoids to investigate neural development and disease. *Nature Reviews Neuroscience* **18**, 573-584, doi:10.1038/nrn.2017.107 (2017).
155 Kaur, S., Kaur, I., Rawal, P., Tripathi, D. M. & Vasudevan, A. Non-matrigel scaffolds for organoid cultures. *Cancer Letters* **504**, 58-66 (2021).
156 Rademakers, T., Horvath, J. M., van Blitterswijk, C. A. & LaPointe, V. L. Oxygen and nutrient delivery in tissue engineering: Approaches to graft vascularization. *Journal of tissue engineering and regenerative medicine* **13**, 1815-1829 (2019).
157 Das, S. *et al.* Innervation: the missing link for biofabricated tissues and organs. *NPJ Regenerative medicine* **5**, 11 (2020).
158 Syedain, Z. *et al.* 6-Month aortic valve implantation of an off-the-shelf tissue-engineered valve in sheep. *Biomaterials* **73**, 175-184 (2015).
159 Kim, S. *et al.* Tissue extracellular matrix hydrogels as alternatives to Matrigel for culturing gastrointestinal organoids. *Nature Communications* **13**, 1692, doi:10.1038/s41467-022-29279-4 (2022).
160 Chrisnandy, A., Blondel, D., Rezakhani, S., Broguiere, N. & Lutolf, M. P. Synthetic dynamic hydrogels promote degradation-independent in vitro organogenesis. *Nature Materials* **21**, 479-487, doi:10.1038/s41563-021-01136-7 (2022).
161 Gjorevski, N. *et al.* Designer matrices for intestinal stem cell and organoid culture. *Nature* **539**, 560-564, doi:10.1038/nature20168 (2016).
162 Goparaju, S. K. *et al.* Rapid differentiation of human pluripotent stem cells into functional neurons by mRNAs encoding transcription factors. *Scientific Reports* **7**, 42367, doi:10.1038/srep42367 (2017).
163 Rocha-Ferreira, E. & Hristova, M. Plasticity in the Neonatal Brain following Hypoxic-Ischaemic Injury. *Neural Plast* **2016**, 4901014, doi:10.1155/2016/4901014 (2016).
164 Shin, J. E. *et al.* Brain and spinal cord injury repair by implantation of human neural progenitor cells seeded onto polymer scaffolds. *Exp Mol Med* **50**, 1-18, doi:10.1038/s12276-018-0054-9 (2018).
165 Schuler, B., Rettich, A., Vogel, J., Gassmann, M. & Arras, M. Optimized surgical techniques and postoperative care improve survival rates and permit accurate telemetric recording in exercising mice. *BMC veterinary research* **5**, 1-11 (2009).
166 Sarvari, A., Naderi, M. M., Sadeghi, M. R. & Akhondi, M. M. A technique for facile and precise transfer of mouse embryos. *Avicenna J Med Biotechnol* **5**, 62-65 (2013).

167 Baumann, B. C., Dorsey, J. F., Benci, J. L., Joh, D. Y. & Kao, G. D. Stereotactic intracranial implantation and in vivo bioluminescent imaging of tumor xenografts in a mouse model system of glioblastoma multiforme. *JoVE (Journal of Visualized Experiments)*, e4089 (2012).
168 Khan, Z. A. *et al.* Multipotential stem cells recapitulate human infantile hemangioma in immunodeficient mice. *The Journal of clinical investigation* **118**, 2592-2599 (2008).
169 Przyborski, S. A. Differentiation of human embryonic stem cells after transplantation in immune-deficient mice. *Stem Cells* **23**, 1242-1250 (2005).
170 Pearl, J. I., Kean, L. S., Davis, M. M. & Wu, J. C. Pluripotent stem cells: immune to the immune system? *Science translational medicine* **4**, 164ps125-164ps125 (2012).